POLITECNICO
MILANO 1863

SCUOLA DI INGEGNERIA INDUSTRIALE
E DELL'INFORMAZIONE

Numerical Modelling of Laser-Driven Proton Acceleration with Nanostructured Targets and TW-class Lasers

Tesi di Laurea Magistrale in
Nuclear Engineering - Ingegneria Nucleare

Author: **Kevin AMBROGIONI**

Student ID: 970692
Advisor: Prof. Matteo PASSONI
Co-advisors: Alessandro MAFFINI, Marta GALBIATI
Academic Year: 2022-23

List of Symbols

Variable	Description	SI System	CGS System
e	Fundamental Charge	$1.602176634\times10^{-19}$ C	$2.08194332709\times10^{8}$ sC
m_e	Electron Mass	$9.1093837015\times10^{-31}$ kg	$9.1093837015\times10^{-28}$ g
c	Light Velocity	2.99792458×10^{8} m/s	2.99792458×10^{10} cm/s
$\hbar$	Reduced Planck Constant	1.05457×10^{-34} J·s	1.05457×10^{-27} Erg·s

Abstract

Laser-driven proton sources seem interesting for many applications (e.g. non-destructive material analysis). Their low space and investment needs can help spread such techniques when the use of conventional radiation sources is prohibitive. Among the others, Double-Layer Targets (DLTs) are a promising way to optimise the coupling between the laser and solid targets to enhance proton acceleration and can be produced at Nanolab (Politecnico di Milano) growing low-density (few mg/cm^3) nanofoams on top of metallic substrates. DLT can be modelled using Diffusion-Limited Cluster-Cluster aggregation (DLCCA) algorithms and particle-in-cell simulations. In this thesis work, a comprehensive investigation of the numerical modelling of proton acceleration driven by the interaction of two examples of class-TW lasers (20 TW and sub-TW) with DLTs is presented. A characterisation of the numerical foams produced with a proprietary DLCCA code and a vast two and three-dimensional PIC campaign using WarpX and Smilei codes were performed to analyse the optimal configuration and explore the influence of different processes in proton acceleration with such lasers. The DLCCA code is proven to provide numerical foams emulating realistic ones obtained in experiments. Also, a method to produce foams having the desired density and thickness with the code is proposed. Then, the modelling choices for the interaction of the two lasers with DLTs are discussed and the most suitable for each case is proposed. The field ionisation was shown negligible in the 20 TW case, while fundamental in the other. The nanostructure description resulted crucial in both cases. The 20 TW laser was proven able to provide protons with energy up to 15 MeV in a 200 nm-thick substrate, 4.0 µm-thick optimised foam configuration, while the sub-TW protons with energy up to 100 keV (laser intensity FWHM 10 fs, foam of 3.0 µm and 1.7×10^{27} m^{-3} density). Lastly, the possible application of such class-TW laser-driven sources for PIXE is discussed. Only the 20 TW laser is promising in the studied configuration. An interesting trend in foam ion acceleration is shown in the sub-TW one.

Keywords: Class-TW lasers, Laser-Driven Proton Acceleration, Double-Layer Target, DLCCA, Particle in-cell, Compact Proton Radiation Sources

Abstract in lingua italiana

Le sorgenti di protoni da laser risultano interessanti per varie applicazioni come l'analisi non distruttiva di materiali per le loro ridotte esigenze di spazio e di investimento. I Double-Layer Targets (DLT) sono un modo promettente per ottimizzare l'accoppiamento tra laser e target solidi e aumentare l'efficienza del processo di accelerazione dei protoni. La produzione di questi target presso il Nanolab (Politecnico di Milano) avviene attraverso la deposizione di nano-schiume a bassa densità (pochi mg/cm^3) su substrati metallici. Algoritmi di aggregazione Diffusion-Limited Cluster-Cluster(DLCCA) e simulazioni particle-in-cell rendono possibile la modellazione dell'interazione tra laser e DLT. In questo il lavoro di tesi, viene presentata un'indagine sulla modellazione numerica dell'interazione di laser di classe TW (20 TW e sub-TW) con DLT per accelare protoni. Si è eseguita una caratterizzazione di schiume numeriche prodotte con un codice proprietario DLCCA e una campagna di PIC 2D e 3D utilizzando i codici WarpX e Smilei. Lo scopo era analizzare la configurazione ottimale ed esplorare l'influenza di diversi processi nell'accelerazione dei protoni con tali laser. Il codice DLCCA si è dimostrato in grado di fornire schiume numeriche che emulano quelle realistiche ottenibili dagli esperimenti. Inoltre, si propone un metodo per produrre schiume con densità e spessore desiderati usando il codice. Viene, poi, discussa la modellazione dell'interazione dei due laser con i DLT e si propone la più adatta per ogni caso. La ionizzazione di campo si è dimostrata trascurabile nel caso da 20 TW, ma fondamentale nell'altro. Descrivere la nanostruttura è risultato fondamentale in entrambi i casi. Il laser da 20 TW si è dimostrato in grado di fornire protoni con un'energia massima fino a 15 MeV con un substrato di 200 nm di spessore e una schiuma di spessore 4 µm e densità ottimale. Si possono produrre protoni con un'energia fino a 100 keV (intensità laser FWHM 10 fs, schiuma densa $1{,}7\times10^{27}$ m^{-3} di spessore 3,0 µm) con il laser sub-TW. Il laser da 20 TW è promettente in applicazioni PIXE. Il laser sub-TW mostra invece un interessante trend nell'accelerazione degli ioni della schiuma.

Parole chiave: Laser Classe TW, Accelerazione Protoni da Laser, Target Double-Layer, DLCCA, Particle in-cell (PIC), Sorgenti di Protoni Compatte

Contents

Introduction

The development of technologies to amplify and shape in space and time the light pulses generated by lasers has opened the possibility to obtain light sources which provide high-intensity electromagnetic fields. The irradiation of materials with such sources irremediably causes their ionisation, forming in this way a plasma. The exploration of the laser interaction with such generated plasmas is a complex scenario which cannot be studied only by means of simple analytical models. The inevitable approximations made in developing them, in fact, necessarily causes the loss of some parts of the physics behind the processes. In this context the use of numerical tools in which the particles composing the plasma are moved self-consistently with the electromagnetic fields is necessary. Among all, the particle in-cell (PIC) method is one of the most common approaches to the study of the laser-plasma interaction thanks to its capability of unveiling the complexity of its physics. During the interaction of the laser with the targets, the electrons and the ions composing them get heated by the laser energy. The heating process can be used to accelerate such particles. When the laser irradiates a solid target, many heating processes happen. Among those, the Target Normal Sheath Acceleration (TNSA) is the most studied and demonstrated one to accelerate low-mass ions, such as hydrogen or carbon, which are naturally present on the surface of solid targets as contaminants. The enhancement of the efficiency of the process has been following many strategies over the years, among those one of the most promising is the use of advanced nanostructured targets such as double-layer targets (DLTs). DLTs are interesting targets which exploit a low-density (few mg/cm^3) layer deposited on a metal film to increase laser energy absorption. Such layers can be obtained at Nanolab (Politecnico di Milano) by using nanostructured materials. Thus, their complex morphology needs an accurate description. The optimisation of this process is fundamental in the development of compact radiation sources. It could, in fact, allow the use of tens of TW or sub-TW compact lasers to produce radiation sources to be used in laboratories or universities. These compact sources require ad-hoc simulations that consider all the relevant physics in this interaction regime like the impact of target ionization and morphology. thesis work falls under this context, with the aim of analysing and optimising the TNSA process when the laser source is a compact one and character-

ising the numerical description of nanostructured targets. Thus the involved topics will be presented following this scheme:

- **Chapter 1** provides the fundamental physics necessary to describe the TNSA process and the fractal nanostructures typical of the foams used in DLTs. Firstly the concepts of laser and plasma are presented, followed by the treatment of the electromagnetic wave propagation inside a plasma. Then some analytical models to describe the electron and ion heating models in solid targets are presented with a focus on the TNSA process and also on the specific case of DLTs. Lastly, the fractal description of nanostructured foams and the effect of the nanostructure in the TNSA process is discussed.
- **Chapter 2** presents the description of the numerical strategies to describe the TNSA process. At first the mathematical bases of the PIC method are described, together with the meaning of lower dimensionality simulations. The dimensionality effects are then discussed. The Monte Carlo method to account for different physical processes in the PIC simulations is then presented: a focus is given to the tunnel ionisation process. Lastly, the diffusion-limited and diffusion-limited cluster-cluster aggregation models are presented as a way to describe numerically the foams.
- **Chapter 3** has the scope of describing the motivations, objectives and methods of the thesis work. In particular, the working principle of the used numerical tools are shown in this chapter after a brief presentation of the context in which the thesis work rises.
- **Chapter 4** is devoted to the presentation and discussion of the results involving the characterisation of the numerical foams generated by a proprietary DLCCA code. The performed numerical simulations to create numerical foams and the developed tool to characterise them are shown in the context of this chapter.
- **Chapter 5** is devoted to the analysis of the results of PIC simulations performed to optimise the simulation set-up and target configuration for lasers with 20TW and sub-TW peak power. The set-up of performed simulations is first described and then the obtained results are shown and commented.
- **Chapter 6** is devoted to the discussion of the results of the PIC simulations. The chapter tries to answer the open questions presented in the objectives of the thesis work and to explicate the phenomena which are seen as a result of the simulations.

The thesis ends with a section devoted to the conclusions and the future perspectives related to the work.

1 | Fundamentals of Physics for Ultraintense Laser-Driven Ion Acceleration

This first chapter aims to present the physical context on which the rest of the thesis work is focused. Firstly, a brief presentation of laser technology and its modelisation is given. Then, the concept of plasma is introduced: a laser interacting with a target can, in fact, ionise it and the result is just a plasma. While ionising the target, the charged particles composing the plasma and resulting from target ionisation can get heated, allowing the possibility to use this kind of interaction as a way of accelerating particles. Different processes can however happen, the focus of the thesis work will be the so-called "Target Normal Sheath Acceleration" (TNSA), a scheme which can be used to accelerate low mass ions up to several dozens of MeV and, so, its physical background will be presented within this first chapter. Many strategies have been investigated to increase ions energy, among the most promising, one can find the use of nanostructured targets. The physical description of nanostructured materials and their effects on laser interaction with matter will be presented as the last, but not less important, part of this introductory chapter.

1.1. Introduction to high-intensity lasers

The acronym LASER stands for "Light Amplification by Stimulated Emission of Radiation". The working principle is then precisely the stimulated emission process [1]. The laser scheme is based on materials which contain at least three energy levels. These materials are inserted in a resonant cavity, the *oscillator*, which is composed of two mirrors perpendicular to the electromagnetic wave propagation direction. The result is the amplification of light [2]. Two are the required conditions to take advantage of this process: the presence of a pumping process which moves the system out of equilibrium; the highest energy level to which the system is brought by the pumping process has to promptly decay, through non-electromagnetic processes, to an intermediate level. It is said that

these two conditions are necessary to create a *population inversion*. This same mechanism of amplification is what gives important characteristics to laser-emitted light, which are monochromaticity, coherence and directionality.

1.1.1. Laser pulse fundamental parameters and modelling

A laser is an optical system which can operate both in continuous and pulsed regimes. It can be described by the following parameters:

- fundamental **wavelength** λ, i.e. the central wavelength of the pulse spectrum;
- the **focal spot** S, defining an area representative of spatial size at focalisation;
- the **polarisation**, i.e. the direction of oscillation of the electric field;
- the **duration** τ, defining a representative of temporal duration of the pulse;
- the **repetition rate**, the frequency at which the laser system deliver pulses;
- the **energy** of the pulse;
- the **intensity**, i.e. the maximum power per unit surface that a laser can release;

A laser pulse can usually be described by a Gaussian pulse, the solution to Maxwell equations in the paraxial approximation. For a complete description and derivation, one should refer to *Principle of Lasers* by *O. Svelto* [1]. The result shows the presence of different modes in the oscillator, among which the simplest one for linear polarisation along y for a wave propagating along x has the following shape:

$$\boldsymbol{E}(\boldsymbol{r},t) = Re\left\{ E_0 \frac{w_0}{w(x)} e^{[i(\omega t - kx)]} e^{\left(-\frac{y^2+z^2}{w^2(x)}\right)} e^{\left[-i\frac{k(y^2+z^2)}{2R(x)} + i\arctan\left(\frac{x}{x_r}\right)\right]} \right\} \boldsymbol{u}_y, \tag{1.1}$$

where e is the Euler number, w_0 is the minimum waist, related to focal spot, $w(x)$ is the laser spot size along propagation, $R(x)$ is the curvature of the gaussian beam, $x_r = \pi w_0^2/\lambda$ is the Rayleigh parameter, k is the wavevector and ω is the frequency. From the solution of Maxwell equations, one can obtain also a relation for laser spot size and curvature:

$$w(z) = w_0\sqrt{1+\left(\frac{x-x_0}{x_r}\right)^2} \qquad R(x) = (x-x_0)\left[1+\left(\frac{x-x_0}{x_r}\right)^2\right]. \tag{1.2}$$

1.1.2. State of the art of tens of TW and sub-TW laser facilities

Since the first experiments happening around '60s, high-intensity laser facilities have been developing over the years. Many techniques have been studied in order to increase laser intensities and to decrease pulse duration, becoming able to achieve high power (PW) and high intensity ($\sim 10^{23}\mathrm{W/cm^2}$) laser facilities. Firstly, the **Q-switching** [3] was developed to obtain a pulsed regime: energy is accumulated through the production of a strong population inversion through pumping processes, then stimulated emission of photons releases energy in $\sim$ ns pulses. The pulsed regime is achieved thanks to the use of a pulse modulator which is inserted in the cavity. Then **mode-locking** [4] was introduced, different modes are created in the oscillator, when the oscillation dephasing between them is well defined, thanks to interference between the waves, one can obtain a short pulse, which can be reduced up to a minimum defined by the bandwidth of the light: larger the bandwidth, shorter is the reachable pulse. For solid or liquid lasers, where the bandwidth is large, $\sim$ fs pulses can be reached. Amplification of the pulse is however needed to reach high intensities, one of the developed methods was the **Optical Parametric Amplification** (OPA) [5] which exploits a non-linear medium to amplify the pulse via effects induced by a pump laser: the result is the increase of the pulse intensity. Finally, the **Chirped Pulse Amplification** (CPA) [6] was integrated, the pulse is firstly stretched through time dispersion in order to decrease its intensity, then amplified and recompressed back to its initial duration, allowing it to reach intensities above the relativistic limit in optics.

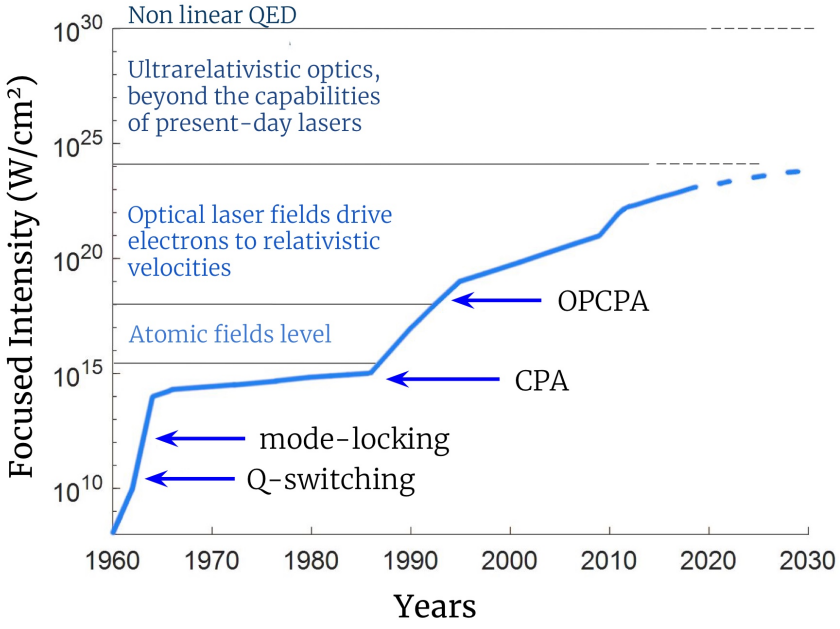

Figure 1.1: Advances in time of the high-intensity laser technology. Adapted from: [7].

Different lasers can be distinguished on the base of the oscillator or amplification material: gaseous lasers, such as the CO_2 ($\lambda \simeq 10$ µm) one, are characterised by thin bandwidth due to lower dispersion inside the medium, while liquid or solid lasers, such as Nd:YAG ($\lambda \simeq 1\mu m$) or Ti:Sapphire ($\lambda \simeq 0.8\mu m$), are characterised by large bandwidth.

The construction of laser facilities which can reach PW as peak power is very complex and space needing. Nonetheless, more compact facilities even go beyond the relativistic limit, which is set to the order of $\sim 10^{18}$ W/cm^2, can be very useful, keeping lower investment and space needs. Commercial systems delivering up to 200 TW of peak power have brought, then, high-intensity lasers also in small university laboratories and sub-TW lasers are available also as table-top lasers, i.e. very compact lasers which can be positioned on top of a table (an example could be Astrella by Coherent©). The interest in using so compact and accessible system is rising.

1.2. Plasma modelling for laser interaction

Prior to explaining the parameters and the models which can be used to describe a plasma, one should define what a plasma [8] is; to do so one should describe its fundamental characteristics:

- it contains a large number of charged particles;
- it can be considered *quasi-neutral* so that in the macroscopic point of view it can be treated as overall neutral: this happens when a large number of charged particles is present, a violation of global neutrality will induce charged particles motion;
- the presence of a great amount of charged particles implies that it will show collective effects due to the electromagnetic field present.

The common idea of plasma as a highly ionised gas, which brought to name it as the *fourth state of the matter*, is so reductive with respect to the general definition of plasma. The latter can, in fact, describe many states, which can, also, be greatly different from the ones of a gas. Surely, the simplicity of creating plasmas from gases, only by heating them up, is the cause of the common idea. Nevertheless, laser-generated plasmas are usually very different from the firsts. To distinguish all different kinds of plasmas, so, parameters have been developed and the next section will provide a summary of the most important ones.

1.2.1. Fundamental plasma parameters

A few simple parameters are fundamental to outline the right way to modelise a plasma: depending on plasma density, average energy and quantity of charged particles, in fact, different regimes can be achieved and some physical effects can become essential to correctly describe the plasma. In this section, all the parameters will be briefly presented and described. To have a deeper knowledge of how one can derive them one should refer to *Fundamental of Plasma Physics* by *Golant V. E. et al.* [9] and *Fisica dei Plasmi* by *Pucella* and *Segre* [10].

Degree of Ionisation

For a *simple plasmas*, i.e. plasmas containing only monovalent ions and their neutral relevant, one defines the *degree of ionisation* of plasma as follows:

$$\eta = \frac{n_i}{n_i + n_a}, \tag{1.3}$$

where n_i is the density of the charged ions and n_a is the density of the neutral particles. Being a ratio between the charged ions density and total heavy particle density, the degree of ionisation gives us knowledge on how much matter is ionised and whether it can be described as a plasma, assuming quasi-neutrality, or it has to be treated as an ionised gas: when its value is above 1%, one can already consider the system as a plasma.

Debye Length

For a simple plasma, the *Debye length* is defined as follows:

$$\lambda_D = \sqrt{\frac{T}{4\pi n_e e^2}}, \tag{1.4}$$

where T is the plasma electron temperature, as an indicator of their mean energy, and n_e is the electron density. The measuring system chosen for the thesis work considers, when it is not differently specified, the Gauss system for the electromagnetic quantities and the temperature in energy units. It can be generalised for a multispecies plasma as:

$$\lambda_D = \left(4\pi e^2 \sum_\alpha \frac{n_\alpha Z_\alpha}{T_\alpha}\right)^{-\frac{1}{2}}, \tag{1.5}$$

where α stands for the species inside the plasma and Z_α is the atomic number of the considered species. The Debye length, named after the first physicist to introduce the

quantity, is related to the spatial distance in which plasma cannot be considered quasi-neutral: single particle effects cannot be neglected below this limit. By using dimensional analysis, one can, in fact, relate λ_D to deviation from neutrality of a plasma [10].

Plasma Frequency

The *Plasma frequency* is a quantity related to the time needed for a plasma to re-balance a charge separation. It is defined as follows:

$$\omega_p = \sqrt{\frac{4\pi n_e e^2}{m_e}}. \tag{1.6}$$

When one refers to plasma frequency, usually refers to electron plasma frequency. Due to different mass and charge, in fact, ions have different dynamical properties and their velocity results lower than electron one: their higher inertia reduces their mobility. An usual approximation is, in fact, to consider them as frozen when describing the plasma, electron plasma frequency is, thus, the one really governing plasma dynamics. This quantity becomes of huge importance when considering the interaction between an electromagnetic wave and a plasma: different regimes of propagation are achieved when an electromagnetic wave has a frequency higher or lower than the plasma frequency.

Plasma Parameter

The *Plasma parameter* is an adimensional parameter which can be defined in relation to the total number of charged particles within a Debye sphere, i.e. a sphere the radius of which is the Debye length. Its definition is:

$$g = \frac{1}{\frac{4}{3}\pi\left(\frac{1}{4\pi e^2}\right)^3 \frac{T^{\frac{3}{2}}}{n^{\frac{1}{2}}}}. \tag{1.7}$$

Knowing that T is related to particles kinetic energy and $e^2/n^{\frac{1}{3}}$ to electromagnetic potential energy, one can easily understand that g can be related to the ratio between energy associated with the electromagnetic field in a plasma and average kinetic energy of its particles; when its value approaches to zero, one can neglect short-range interactions: these plasmas can be treated as ideal plasmas.

Collision Frequency

In a plasma, charged particles can collide among themselves in many different ways such as elastic scattering, inelastic scattering, ionisation collision and so forth. The *Collision*

frequency is a parameter, different for each kind of collision, which allows discerning whether that process can be neglected in modelling: it can be seen as the inverse of the average time between two collisions; it is defined as follow:

$$\nu = n\sigma_\alpha v, \tag{1.8}$$

where σ_α is the cross section of the specific collision process and v is the thermal velocity of the particles. Cross sections can be differently modelled considering the different processes, one can refer to the aforementioned books to have a deeper knowledge of the ways of modelisation.

Quantum Parameter

The *Quantum parameter* is defined as the ratio between Fermi energy and thermal energy of the plasma:

$$\sum = \frac{\hbar^2 n^{\frac{2}{3}}}{Tm}. \tag{1.9}$$

Since Fermi energy is associated, by means of the uncertainty principle, with the uncertainty on the particle momentum, while the temperature is associated with momentum, one can understand that only having $\sum \ll 1$ allows a non-quantum modelisation.

Relativistic Parameter

The *Relativistic parameter* permits one to understand whether one can neglect relativistic effects in the model. The parameter is defined as follows:

$$R.P. = \frac{T}{mc^2}. \tag{1.10}$$

When the relativistic parameter assumes a value approaching zero, one can neglect relativistic effects, otherwise one should include them in the model.

One can, then, imagine that very different matter conditions can be treated as plasmas: density can vary up to $\sim 10^{35}$ m^{-3} and temperature can reach very high values. A graphical way to summarise all the possible conditions and the right way to model them can be found in figure (1.2).

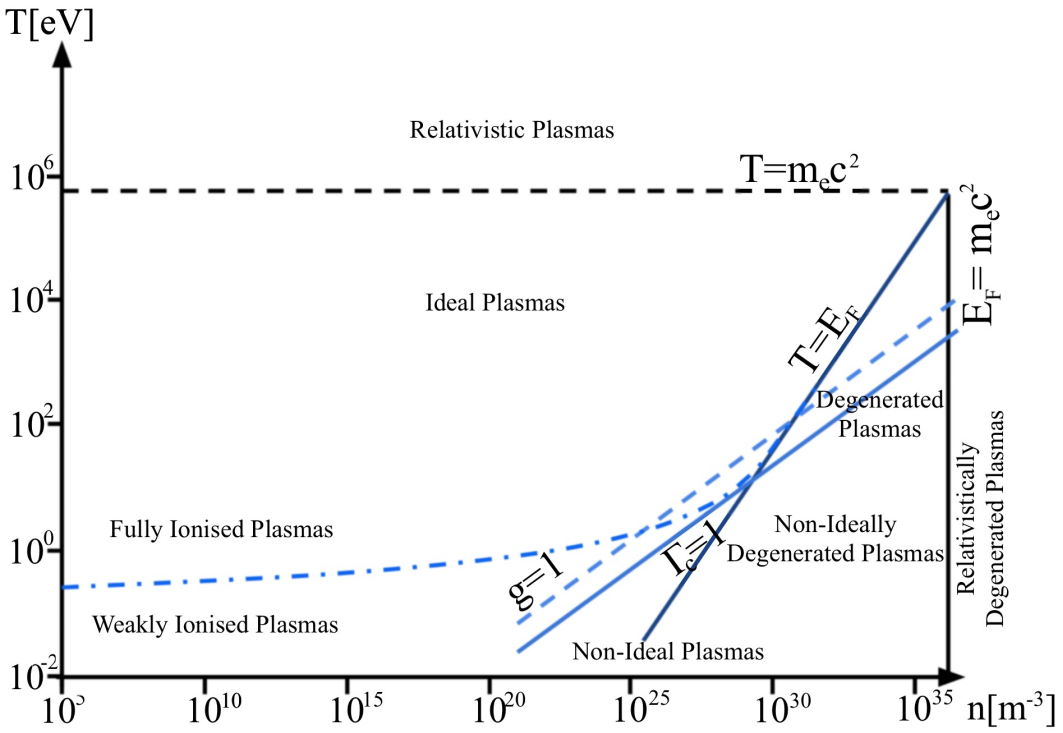

Figure 1.2: Graphical summary of various density-temperature conditions at which matter can be modelled as a plasma. Adapted from: [11].

As one can observe, in a region spanning several orders of magnitude of density and temperature a plasma can be treated as a simple non-relativistic and non-quantum plasma.

1.2.2. Laser-generated plasmas

Photons produced by a laser, being usually in the visible-infrared range, do not have high enough energy to ionise the matter within the most probable process: the *single photon ionisation*. Different mechanisms, which rely on a higher order of perturbation on the atom structure, have to be taken into account to explain experimental results. Indeed it is proved that high-intensity lasers can ionise matter. The first process to account for is the *multiphoton ionisation*, its probability is orders of magnitude lower than the single photon one, but when laser intensity is high, above the threshold of $\sim 10^{14}$ W/cm^2 its effect has to be taken into account. Secondly, but not for importance, the *tunnel ionisation*, has to be taken into account: when again the intensity threshold of $\sim 10^{14}$ W/cm^2 is trespassed, the electromagnetic field of the wave can bend the Coulomb potential in the atom. This leads to a reduction of the potential barrier felt by the electrons in the atom, allowing them to be released through tunnel effect. Lastly, also *impact ionisation* has to be taken into account: when a large enough number of free electrons is created, they can ionise

neutrals and ions, colliding with them. A visual scheme of the electromagnetic processes leading to ionisation is presented in figure (1.3). Laser can as a matter of fact create a plasma and, when its intensity is high enough, matter is already ionised before the arrival of the intensity peak.

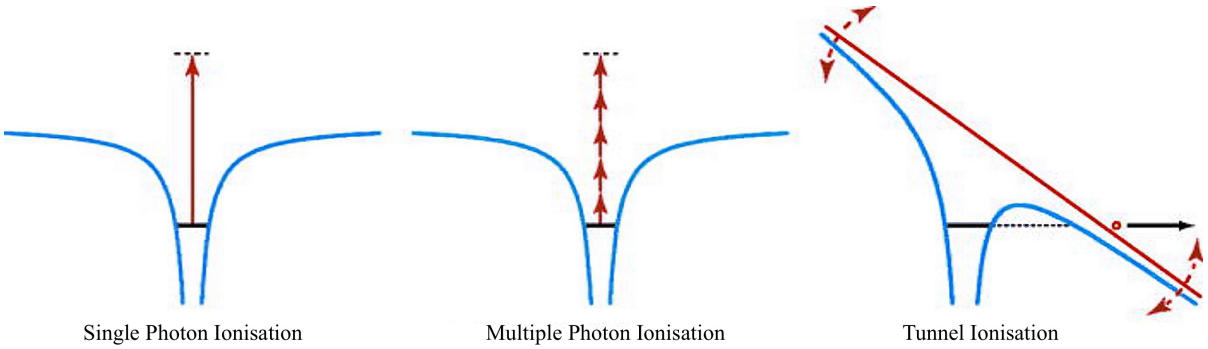

Figure 1.3: Graphical summary of various field ionisation processes due to high-intensity electromagnetic field. Source: [12].

Other important aspects to take into account when considering the interaction of a laser pulse with matter, are the effects which has to be considered in the theoretical description. One example could be whether the created plasma is relativistic. In order to do so, a characteristic velocity has to be taken into account: considering a monochromatic wave and particularly its vector potential, then, in the single-particle picture, one can determine a maximum velocity for the electrons in the field. The ratio between maximum particles momentum and mc is then defined as *normalised vector potential*:

$$a_0 = \frac{eA_0}{mc^2} \tag{1.11}$$

where A_0 is the maximum amplitude of the vector potential in the wave and m is the particle mass. When $a_0 \geq 1$ relativistic effects cannot be neglected in the theoretical analysis. One can observe that common high-intensity lasers, having an intensity higher than 10^{18} W/cm^2 lead electrons to energies above the relativistic limit, while an intensity on the order of 10^{24} W/cm^2 would be needed in order to reach the same limit for ion motion.

1.2.3. Regimes of interaction between lasers and plasmas

To correctly approach the physical description of the behaviour of a plasma subjected to a laser pulse, the simplest way is to consider its linear response to a monochromatic electromagnetic wave of frequency ω and wavevector k. The simplest way to describe

this is considering a non-relativistic, non-collisional, cold plasma, meaning neglecting relativistic effects and ion motion. The result, which can be obtained using the so-called multiple-fluid model [13], gives the following dispersion relation for a transverse wave in the plasma:

$$k^2c^2 = \omega^2 - \omega_p^2 \tag{1.12}$$

and the following other dispersion relation for a longitudinal plasma wave:

$$\omega = \omega_p^2. \tag{1.13}$$

Thus, an electromagnetic wave can propagate only when wave frequency is higher than plasma frequency: when this does not happen, electron dynamics is faster than electromagnetic wave frequency, being, so, able to screen an electromagnetic wave approaching plasma. The plasma frequency is then a cut-off frequency. This kind of dispersion relation allows us to define an important parameter, related to electron density.

Critical Density. The *Critical density* is a parameter which relates plasma electron density to the regime in wave propagation. It is defined as follows:

$$n_c = \frac{m_e\omega^2}{4\pi e^2}. \tag{1.14}$$

It represents the maximum density that a plasma should have in order to allow the propagation of an electromagnetic wave the frequency of which is ω.

It is, thus, possible to distinguish three different regimes of propagation for a plasma:

- **Overdense plasma**: when $n_e > n_c$ an evanescent wave will occur in plasma. The evanescent wave exponentially decreases its intensity while travelling along the material. The inverse of the slope value of the intensity at the interface is called skin depth and it can be computed as:

$$l_s = \frac{c}{\sqrt{\omega_p^2 - \omega^2}} \simeq \frac{c}{\omega_p} \tag{1.15}$$

  where ω is the frequency of the impinging wave. The approximated formula is usually valid when the wave frequency is smaller than the plasma frequency. The skin depth is a parameter related to the penetration of the wave into the material;

- **Critical plasma**: when $n_e = n_c$, a longitudinal wave will be created; an extreme coupling between plasma and electromagnetic wave will occur. The created wave is a longitudinal electrostatic wave, meaning its group velocity is equal to zero, this

kind of wave is related to charge density perturbations and it is often referred to as *plasmon*;

- **Underdense plasma**: waves will propagate within the plasma; propagation velocity will reach light velocity in vacuum with electron density approaching zero.

When relaxing the simplifying hypotheses on ions motion, different features can be studied: their explanation is beyond the scope of this thesis work and one should refer to chapters 6, 7 and 8 of *The Physics of Plasmas* by *Sanderson J.J.* [8].

When one would like to relax instead the non-relativistic hypothesis a first simple point of view of what happens inside a plasma can be given by looking at the single-particle picture: by using perturbation theory applied to the momentum equation of a charged particle in an oscillating electromagnetic field, the second order of perturbation term will give birth to the so-called *ponderomotive force*, which can be related to a potential named *ponderomotive potential*, defined by [13]:

$$\Phi_p = \frac{e^2}{2m_e\omega^2}\langle \boldsymbol{E}^2 \rangle = m_e c^2 \big(1 + \langle a^2 \rangle\big)^{\frac{1}{2}}, \tag{1.16}$$

where a is the adimensional vector potential. This simple result is quite important since the same scaling can be retrieved in one of the results of the equation of motion of a relativistic cold plasma when considering a transverse circularly polarised wave, as it was done by *Akhiezer* and *Polovin* in *Theory of Wave Motion of an Electron Plasma* [14]. In this case, the computed dispersion relation can be written as follows:

$$k^2c^2 = \omega^2 - \frac{w_p^2}{\gamma_e} \quad \text{where} \quad \gamma_e = \left(1 + \frac{a_0^2}{2}\right)^{\frac{1}{2}}, \tag{1.17}$$

where a_0 is the normalised vector potential. One can so retrieve that the cut-off frequency is increased when considering relativistic effects due to the increased inertia of the electrons: this effect is called *self-induced relativistic transparency*. This means that one can still distinguish the three different regimes of propagation, but their separation becomes less strict, the plasma is in fact considered critical, or nearcritical, in a range around n_c and $\gamma_e n_c$: the wave can, in fact, propagate through the plasma until electron density reaches $\gamma_e n_e$.

Another important effect is, then, the so-called *relativistic self-focusing*: by applying Snell law to a Gaussian beam crossing an underdense or nearcritical plasma, considering the relativistic dispersion relation, one can obtain that, due to differences in vector potential amplitude of the beam itself, some part of it can undergo total reflection. The beam

power threshold condition P_c for an underdense plasma with electron density n_e is given by:

$$P_c \simeq 43\text{GW}\ \frac{n_c}{n_e}. \tag{1.18}$$

This reflection causes in the pulse channel a reduction of the spot leading to self-focusing. The hypotheses made to retrieve the formula above neglect all the effects of a Gaussian beam on plasma density, but however, a good agreement with experiments is achieved.

Following, however, the treatment by *Akhiezer* and *Polovin* [14] one can see that while an electromagnetic wave is propagating through a plasma, also longitudinal modes can be excited. The longitudinal modes, being due to charge density oscillations, are the basis for a separation of charges. This separation can be very effective in creating a strong electric field in plasma when relativistic effects are included; strong non-linearities must, in fact, be accounted for. What one can obtain is a relation between the longitudinal electric field in plasma E_x, $\gamma_p = 1/\sqrt{1 - v_p^2/c^2}$, i.e. the relativistic factor associated with the velocity of propagation of the longitudinal wave and γ_e, the relativistic factor associated with electron fluid velocity:

$$E_x = \frac{m_e \omega_p c}{e}\sqrt{2(\gamma_p - \gamma_e)} \tag{1.19}$$

and also a relation for electron density:

$$n_e = \frac{n_0}{1 - u_x/v_p}, \tag{1.20}$$

where u_x is electron fluid velocity and v_p is the wave propagation velocity. The maximum electric field value can be retrieved when electron fluid velocity becomes null, while electron density diverges when fluid velocity is equal to wave velocity. By following algebra shown in *A Superintense Laser-Plasma Interaction Primer* by *Macchi A.* [13] one can also retrieve the distance between two spikes of the density as:

$$\lambda_p = 4\frac{c}{\omega_p}\sqrt{2(\gamma_p - 1)}. \tag{1.21}$$

1.2.4. Acceleration processes in laser interaction with targets

All the processes shown above can be of fundamental importance for applications in the field of electron acceleration. Electron acceleration and heating are fundamental steps to be able to accelerate ions too. Electron acceleration processes which take place in an underdense plasma hit by a laser pulse or a charged particle beam can be described

correctly by the theory of the *wakefield acceleration.*

Wakefield Acceleration. In an underdense plasma, due to the separation of charges happening when a longitudinal wave is propagating through it, light particles, such as electrons, can be widely accelerated. Following what was done by *Tajima T.* and *Dawson J. M* [15] one can retrieve a simple scaling for maximum electron energy reachable through this acceleration scheme:

$$\varepsilon = 2m_e c^2 \left(\frac{\omega}{\omega_p}\right)^2 \tag{1.22}$$

and one can also compute, estimating the accelerating distance, an accelerating gradient of $\varepsilon/L = (2m_e c^2/\lambda)(\omega_p/\omega)$, that is in the order of dozens of MeV/mm.

In a nearcritical plasma, instead, resonance effects become preponderant: the so-called *direct laser acceleration* (DLA) process has to be considered.

Direct Laser Acceleration. When considering an electron moving inside a nearcritical plasma, relativistic self-focusing becomes an important effect. The ponderomotive force effect leads to a depletion of electrons in the laser channel: an electrostatic radial electric field is then generated. In the meantime, electron motion generates an azimuthal magnetic field [16]. Both the fields, reach their maximum on the outer radius of the channel and they can be well described by a linear trend. The equation of motion of an electron in the presence of static fields and electromagnetic waves leads to an equation describing a driven oscillator the eigenfrequency of which are betatron oscillations; their frequency depends on the amplitude of the fields, electron longitudinal velocity and electron kinetic energy. It is possible to observe, then, that resonances are hit when betatron frequency is in relation to electron velocity:

$$\omega_\beta = \sqrt{\frac{K_E + v_x K_B}{\gamma}} = 1 - \frac{v_x}{v_{ph}}, \tag{1.23}$$

where K_E is the radial derivative of the static electric field, K_B is the radial derivative of the static magnetic field, γ is the relativistic gamma factor, v_x is the longitudinal electron velocity and v_{ph} is the phase velocity of the electromagnetic wave, which is above light velocity. When the frequency of the transverse electron oscillations in the static electric and magnetic fields coincide with the laser frequency in the electron reference frame, a resonance occurs allowing an energy exchange between the laser and the electron. The latter starts moving along the laser propagation direction. Being however ω_β dependent on γ, when the kinetic energy grows, electrons detune and acceleration ceases. This gives a energy gain proportional to $I^{\frac{1}{2}}$, where I is laser intensity. One can, however, demonstrate that only when $a_0 > 2$, the DLA process can start, becoming the most important process

in electron heating.

When considering, instead, an overdense plasma different processes happen. As it was already stated before, electromagnetic waves do not propagate and an evanescent wave is created inside the plasma when considering linear waves. Experimental and theoretical observations show that the ponderomotive potential mentioned above, however, has an important effect in the creation of the so-called hot electrons in an overdense plasma, which maximum energy in first approximation can be estimated by the **ponderomotive scaling**:

$$\varepsilon = m_e c^2 \left(\sqrt{1 + \frac{a_0^2}{2}} - 1 \right). \tag{1.24}$$

The simplest explanation of this scaling is the creation of a standing wave, due to the reflection of the incident electromagnetic wave by plasma itself. Other effects, however, should be taken into account when considering acceleration processes of the electrons present in the skin layer of the overdense plasma: *collisional absorption*, *anomalous skin effect*, *resonant absorption*, *Brunel heating* and $\boldsymbol{j} \wedge \boldsymbol{B}$ *heating*.

Collisional Absorption. When considering a plasma one usually neglects the effects of electron friction: when considering an evanescent wave, however, this assumption leads to a null absorption coefficient. In order to avoid such an effect one may consider *Coulomb collisions* between electrons and ions. Laser absorption happens, then, through the *inverse Bremsstrahlung (IB)* process, a collisional absorption process. The absorption coefficient, using Fresnel formulas, can be computed as [17]:

$$A = \nu_{ei} \frac{\omega^2}{\omega_p^3} \sim 2\varepsilon^{-\frac{3}{2}} \frac{\omega^2}{\omega_p^3} \tag{1.25}$$

As it is possible to observe, absorption decreases with electron energy, which means the mechanism can be effective only during the rise of the pulse, but it cannot explain the energy absorption leading electrons to energies higher than thermal energy.

Anomalous Skin Absorption. A simplified description [18] of the anomalous skin absorption can be obtained by the treatment of the *sheath inverse Bremsstrahlung (SIB)* [19]. After IB happens during the first stages of the interaction of a plasma with an electromagnetic pulse, electrons get heated and expand creating at the interface an electric sheath field which can be effectively a reflective boundary. Electrons which move due to an electromagnetic wave, then, get reflected from the sheath within the SIB process that works as an effective collision. The absorption coefficient due to SIB can so be estimated

as before considering the collision frequency:

$$A \sim \frac{\omega_p v_e}{c} \frac{\omega^2}{\omega_p^3}, \tag{1.26}$$

where v_e is the thermal velocity of electrons due to IB. This effect, anyway, cannot explain properly totally the heating of the electrons.

Resonant Absorption. When considering a wave in a 1D geometry impinging on an inhomogeneous plasma, that is the case after collisional absorption heats up the plasma, using perturbation theory [20] one can observe a variation in density given by:

$$\delta n_e = \frac{1}{4\pi e} \frac{(\boldsymbol{E} + \boldsymbol{E}_d) \cdot grad(n_0)}{n_0 - n_c}, \tag{1.27}$$

where $\boldsymbol{E}$ is the self-consistent electric field of the plasma, $\boldsymbol{E}_d$ is the external electromagnetic wave and n_0 is the unperturbed electron density. One can observe that when $n_0 = n_c$ and $\boldsymbol{E}_d \cdot grad(n_0) \neq 0$, i.e. in the P-polarised wave case, a singular point is created and a plasmon is excited. If thermal velocity is different from zero, the oscillation will propagate along the wave propagation direction. Due to the use of perturbation theory, the treatment is, however, valid only when density does not vary too much over oscillation amplitude, meaning that it will not be able to explain completely the absorption effects in overdense plasmas, where the density variations are high, particularly on the surface.

Brunel Heating. The Brunel heating is modelled considering in this case a step-like plasma profile, i.e. the opposite condition with respect to the resonant absorption. An external electric field which is constant in space, varies only in time and is directed as the electromagnetic wave one would like to consider is the driving force of the heating process [21]. To keep at the surface a null electric field at each cycle electrons get extracted from plasma, but this can happen only when the sheath electric field caused by the electrons heated by collisional absorption can be overcome. This results in the following condition on the intensity of the field: $4(I/c)\sin^2\theta > n_0 T_e$, where θ is the incidence angle of the wave. Switching to Lagrange variables one obtains two different solutions, one for electrons which do not cross the boundary after the electromagnetic cycle and the other for electrons crossing it [22]; the latter feel a secular force leading to a net acceleration and dephasing which depends on their initial position x_0: this net acceleration increases the absorption of the electromagnetic wave. Assuming that ejected electrons then re-enter the plasma and correcting the treatment with relativistic effects, it is possible to estimate

the absorption coefficient as:

$$A \simeq \frac{f(A)}{a_0}[(1 + f^2(A)a_0^2 \sin^2\theta)^{\frac{1}{2}} - 1]\tan\theta, \tag{1.28}$$

where $f(A) = 1+\sqrt{1-A}$. The maximum absorption strongly depends on the regime and for $a_0 \ll 1$ maximum absorption is achieved for grazing angles, while for $a_0 \gg 1$ for small angles. This effect better explains the experimental results, but still, it is not applicable when waves are S-polarised or in normal incidence.

j $\wedge$ ***B*** **Heating.** Last effect to be considered is the ***j*** $\wedge$ ***B*** heating, which is based on the treatment of the Brunel effect. It is differentiated from the latter by the force driving the process [23]. In this case is in fact the ***v*** $\wedge$ ***B*** force, which is then present in each kind of polarisation, is the driving force. Again both a secular and an oscillating, which oscillation frequency is 2ω, components of the force will be present. The oscillating term vanishes when the wave is circularly polarised. Then, linearising the equations via perturbation theory, it is possible to obtain the following formula for the electron density variation:

$$\delta n_e = n_0 \frac{2F_0}{m_e l_s \omega_p^2} e^{-\frac{2x}{l_s}} \left(1 + \frac{1-\epsilon^2}{1+\epsilon^2}\frac{\cos 2\omega t}{1 - 4\omega^2/\omega_p^2}\right), \tag{1.29}$$

where $F_0 = a_0^2(2m_e c^2/l_s)(\omega/\omega_p)^2$, l_s is the skin layer, e is the Euler number and ϵ the ellipticity. One can observe that when $\delta n_e < 0$ electrons have escaped from the surface. Their motion will be similar to the one explained in the Brunel effect, reaching then an accelerating regime. Secondly, one can well notice that when $\epsilon = 0$, i.e. circular polarisation, no oscillating term is present meaning a weaker coupling between plasma and electromagnetic wave and subsequent suppression of hot electrons generation.

All these mechanisms are fundamental in explaining also the majority of ion acceleration mechanisms. A review of the most common proposed ion acceleration mechanisms can be found in *Ion acceleration by superintense laser-plasma interaction* by *Macchi A.* and *Borghesi M.* and *Passoni M.* [24]; the most studied ones can be regrouped in:

- **Target Normal Sheath Acceleration (TNSA)**, the most widely encountered during experiments which will be better explained in the following section. In this case, ion acceleration is due to the creation of a sheath field behind the target caused by the separation of charge induced by a laser;
- **Radiation Pressure Acceleration (RPA)**, which can be explained as an effect of the radiation pressure. Radiation pressure is an effect of the ponderomotive force, which, piling up electrons inside the plasma, creates a charge separation layer. Two

different regimes can be identified: the *hole boring regime*, happening in thick targets in which laser pulse, acting as a piston, deforms plasma surface accelerating ions on the front surface as an effect of momentum balance between electromagnetic field and particles [25], the *light sail regime*, applying to thin targets in which laser can directly accelerate ions. The background plasma is in fact eliminated by the first part of the pulse, while the tail can directly accelerate ions to high energy [26]. In general, RPA becomes a preponderant effect for laser intensities higher than present-day technologies since ions should reach relativistic energies [27];

- **Collisionless shock acceleration** which can be explained in a fluid description, where supersonic shock waves can be generated by radiation pressure or hot electrons driven by a laser pulse. Such waves are able to accelerate ions up to twice their propagation velocity [28], allowing, then, to a different scheme for ion acceleration within laser-plasma interaction;
- **Coulomb explosion**, is a mechanism which can occur only when plasma has a limited size [29], usually smaller than the laser wavelength. This effect appears to be of great importance when nanostructured materials are considered and it will be explained in one of the next sections.

1.3. Target Normal Sheath Acceleration (TNSA)

As anticipated, TNSA is the main process considered when talking about ion acceleration, in particular on low-mass ions that can usually be found as contaminants in metallic foil surfaces, such as hydrogen and carbon. Lots of efforts have been put in order to understand the physics of the process and surely numerical simulations have been needed in order to reach a deeper knowledge of it. Nevertheless, simple models are always important in order to have a simple understanding of the process features. Many advances have also been achieved in target production, in order to reach higher efficiency in fast ions generation: production of ultrathin metallic films or *double layer targets* have resulted among of the most promising ways to do so.

1.3.1. TNSA: an ion acceleration scheme in solid targets

TNSA was the first proposed as an explanation of ion acceleration in an experiment [30] performed using a laser and solid targets [31]. The experiment showed the acceleration of low-mass ions, which can be found as hydro-carbon contaminants on the surfaces of solid targets. The TNSA process is mainly effective on these ions since their charge to

mass ratio is the highest. Two main strategies of modelling have been proposed in the years, the sheath acceleration [32] and the plasma expansion into vacuum [33]: both the strategies base on electrostatic, non-relativistic approximations for ions motion using two fluid equations and decoupling laser-interaction dynamics from ions acceleration. Their hypotheses however lead to modelisations which are complementary for understanding different features of the acceleration process.

Sheath Acceleration.

By following the model proposed by *Passoni M.* and *Lontano M.* [34], which differently from the previously cited [32], takes into account relativistic effects of electron population, one can have a good agreement between maximum ion energy estimated from the model and experiments. The model relies on a quasistationary solution of the Poisson equation that can be considered valid in the first stages of ions acceleration. After laser-target interaction has happened, two families of electrons are created, cold electrons and hot electrons. Considering the latter, one can assume, in a period of $\sim$ 100 fs after laser interaction, they are in equilibrium, following, thus, the Maxwell-Jüttner relativistic distribution function, which can be approximated, in most of the cases, with its ultra-relativistic limit. Electrons with an energy lower than electric potential energy will be trapped at the rear surface of the target and give birth to an electric field which can accelerate ions. By applying some algebra to the Poisson equation one can then obtain the following relation for the normalised electric potential $\varphi = e\phi/T$, where T is the average hot electron kinetic energy:

$$\int_{\varphi_0}^{\varphi(\xi)} \frac{d\varphi}{(\exp\varphi - \varphi - 1)^{\frac{1}{2}}} = -\sqrt{2}\xi, \tag{1.30}$$

where φ_0 is the normalised electric potential at the rear surface of the target and $\xi = x/\lambda_D$. To evaluate φ_0 one should then compute the electric field inside the target, making the hypothesis that deep inside the target quasi-neutrality is guaranteed. Solving the Poisson equation in the target, in the hypothesis that the electric field will be null deep in the target, one obtains the following relation between φ_0 and the normalised maximum electron energy φ^*:

$$\varphi_0 = \frac{\exp\varphi^*(\varphi^* - 1) + 1}{\exp\varphi^* - 1}. \tag{1.31}$$

Maximum electron energy φ can then be estimated thanks to a scaling based on published results as $\varphi^* = 4.8 + 0.8\ln E_L$, where E_L is the laser pulse energy in Joule and, in first approximation, electrons mean energy T can be estimated via the ponderomotive scaling. Considering that heavy ion motion is lower than low mass ions one, i.e. $t < \omega_{pi}^{-1}$ they can

be considered as immobile, and that low mass ions are usually in a negligible concentration with respect to heavy ones, one can estimate their maximum energy treating them as test particles so that $\varepsilon_{pmax} \simeq ZT\varphi_0$. One can refine, then, the solution by eliminating the hypothesis of ultrarelativistic limit [35], by considering the effect of target thickness [36] or even considering non-equilibrium effects [37] obtaining good agreement with experimental results. Surely, considering ions as an immobile population leads to neglecting the decrease of the electric field due to positive particle motion. Neglecting collision then means that neither electron cooling is considered: long-time behaviour, thus, cannot be predicted by the model, which is however valid for the acceleration of the low mass ions which sit on the most external surface of the target.

Plasma Expansion into Vacuum.

Following what was done by *Mora P.* [33], making the hypotheses of a Maxwellian distribution for the electrons that were heated by the laser and that plasma can be considered locally neutral, considering a plasma slab one can simplify a 1D two fluid equation to obtain a simple result for ion motion in the accelerated plasma. The equations to be solved, after some simplifications are:

$$\frac{\partial u_i}{\partial t} \simeq \frac{c_s^2}{n_0}\frac{\partial n_i}{\partial x}, \qquad \frac{\partial n_i}{\partial t} \simeq n_0 \frac{\partial u_i}{\partial x}, \tag{1.32}$$

where n_0 is the equilibrium density, n_i is the ion density, u_i the ion velocity and $c_s = (ZT_e/m_i)$, i.e. the ion-acoustic velocity. One can compute the ion front velocity and the electric field directly from the solution of the equations above, reaching a solution that is singular at the start of the interaction. Considering that for $t = 0$ the presence of a sheath field is experimentally confirmed, an interpolation of the field obtained by the two fluid equation and the sheath model can be done by obtaining a maximum velocity for the ion expansion front given by:

$$u_{if}(t) \simeq 2c_s \ln\left[\frac{\omega_{pi}t}{\sqrt{2e}} + \left(\frac{\omega_{pi}^2 t^2}{2e} + 1\right)^{\frac{1}{2}}\right], \tag{1.33}$$

where ω_{pi} is the plasma frequency of the ions. From this also a spectrum for ion energy can be obtained:

$$\frac{dn_i}{d\varepsilon_i} = \frac{n_0/T_e}{\sqrt{2\varepsilon_i/T_e}} \exp -\sqrt{\frac{2\varepsilon_i}{T_e}} \quad \text{when} \quad \varepsilon_i \leq \frac{m_i}{2}u_f^2. \tag{1.34}$$

The model however takes into account a one-species plasma, which cannot be usually considered true, since low-mass ions often are the components of a contaminant layer.

However, since their concentration is generally negligible in the first moment of the expansion, they can be treated at first as test particles. Due to lower inertia, however, their motion will be faster than heavy ions one and at some position their density can become equal to or higher than the heavy ions one: in that case, their motion will be dominated by the two fluid equation shown before [38]. One can observe that, however, due to the neglection of collisions and other simplifications, ion velocity will have a continuous growth: it is not possible to estimate the real ion maximum energy without artefacts.

1.3.2. State of the art of target for TNSA

The development of targets for TNSA which can optimise the coupling between laser pulses and, as a consequence, increase in ion energy while keeping constant laser power is still an open point in research. Also, the development of strategies allowing to exploit the high-repetition rate of the laser pulses to accelerate the ions is another open topic to be investigated. Many strategies have been proposed as solutions for the open questions and they can be regrouped into two main categories: the use of liquid targets and the use of solid targets. Among the seconds, the use of metallic substrates has been widely investigated. At Nanolab (Politecnico di Milano), two are the main strategies which have been followed over the years to increase the efficiency of the TNSA process:

- the decrease of solid foil thickness [39], which however imposes also limits on laser prepulse in order to avoid target pre-expansion. To do so, one of the possible ways consists in using High Power Impulse Magnetron Spattering (HiPIMS) deposition of compact freestanding films [40];
- the use of advanced targets which exploits the modifications in the irradiated surface of the solid targets. Among these kinds of strategies, one can find the superposition of a nearcritical layer [41] on the metallic foil to enhance the production of hot electrons. One of the possible ways of producing near-critical layers is the production of low-density nanofoams. They are characterised by an alternation of voids and overdense nanoparticles happening at the nanometric level and they can be produced using advanced techniques of material production such as Pulsed-Laser Deposition (PLD) [40]. Foam characteristics, such as density and thickness, can be tuned by setting different conditions in the PLD process parameters. This kind of target is often referred to as *Double Layer Targets*(DLTs), the structure of which can be seen in figure (1.4).

The combination of the production of double-layer targets from thin films is not straightforward: studies on the best sacrificial layer to be used in the production of solid foils are

still on course and also the successive deposition of the foam on the thin film can damage it or however, its characteristics can be less predictable.

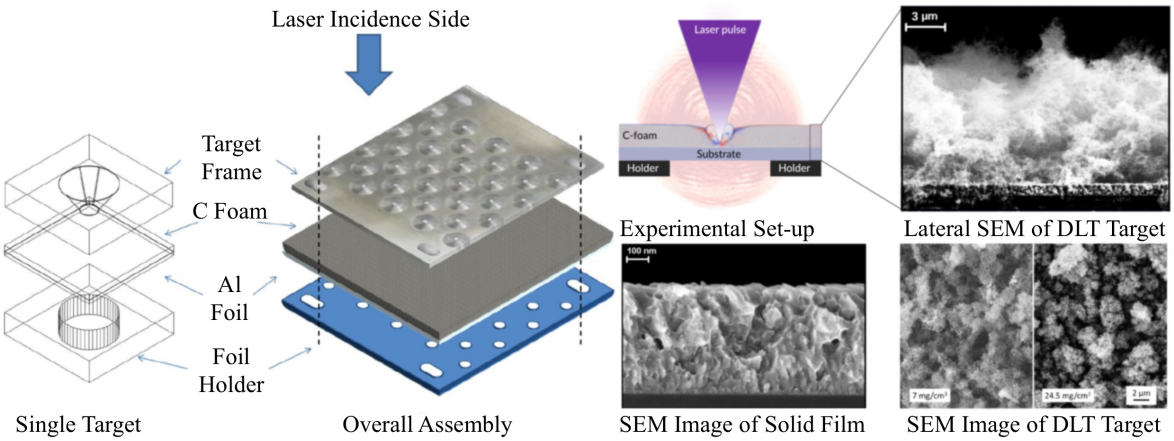

Figure 1.4: DLT experimental configuration in laser-plasma experiments. Adapted from: [40] and [42].

1.3.3. Effects of a nearcritical layer in TNSA

As previously remarked, the attachment of a nearcritical layer can be one of the ways to increase the efficiency of the acceleration process. This increase is mainly due to two effects which have already been explained in section (1.2.3):

- the *relativistic self-focusing* effect, which makes possible the reduction of the spot of the laser crossing it [43]. It has been shown, in fact, that a great increase of laser intensity can in fact be obtained via a nearcritical plasma lens [44]; an optimal plasma length can be computed for a Gaussian pulse and it is called *plasma self-focusing length*:

$$d_{opt} = \sqrt{\frac{w_0^2 - w_m^2}{\overline{n}}}, \tag{1.35}$$

  where w_0 is the gaussian pulse waist before the nearcritical plasma, w_m is the minimum waist and $\overline{n} = n_e/\gamma_0 n_c$. The minimum waist value has been proposed to be $w_m = \lambda/(\pi\sqrt{\overline{n}})$ [45]. This effect has been proven to be effective in enhancing TNSA, also, thanks to the steepening of the laser pulse when exiting the nearcritical plasma [45];

- the *coupling between laser and plasma* due to resonance effects in nearcritical plasmas. Increased absorption of laser energy has been proved [46], as electrons in a nearcritical plasma can be accelerated via direct laser acceleration [47] creating a higher sheath electric field behind the high-density layer. Superponderomotive elec-

trons can be accelerated in the nearcritical plasma [48]. Their contribution to the sheath electric field becomes of greatest importance in ions acceleration, being able also to enhance the effects of RPA on the ions.

Since nearcritical layers, however, are usually obtained by creating nanostructured materials, their effect can be greatly different from using a homogeneous nearcritical layer. The effect of foam nanostructure [49] or nanotubes [50] have been investigated, leading to great differences: the focus of this thesis work will be on foam nanostructured layers and a deeper introduction to these materials and their effects in ion acceleration will be given later on.

A sheath model to take into account, in first approximation, a homogeneous nearcritical layer in a TNSA context is given following what is done by *Pazzaglia A. et al.* [51]. When considering a nearcritical layer, laser propagation inside it becomes of great importance in evaluating electron behaviour. In the hypothesis the plasma behaves like a thin lens, one can obtain an equation for laser waist variation along the propagation direction, obtaining the minimum waist value for a distance equal to the self-focusing length in (1.35). An energy balance of the laser pulse is then performed considering that part of it will be reflected at the plasma surface and that another part will be absorbed by electrons: assuming that electrons are heated by the ponderomotive potential, a simplified model for pulse propagation in a nearcritical plasma is obtained. Knowing then that the energy lost by the laser during the propagation is given to the electrons one can estimate their mean energy as:

$$\varepsilon_{nc}(x) = \frac{(1 - R_D)E_{L0} - E_L(x)}{N_{nc}(x)}, \tag{1.36}$$

where R_D is the reflectivity coefficient, E_{L0} is laser pulse energy before entering the plasma, $E_L(x)$ is laser pulse energy at position x and $N_{nc}(x)$ is the total number of heated electrons in laser channel up to position x. To consider the second overdense layer in a DLT one should then consider a corrected ponderomotive scaling for electron heating in an overdense target considering the remaining part of the energy inside the laser pulse and, thus, averaging the two electrons populations, one can obtain a mean electron temperature to be inserted in the sheath model shown before in (1.3.1) to obtain an estimation of ions maximum energy.

1.3.4. Optimal nearcritical layer density and thickness estimation

Based on the model just explained, one gets, in the end, an estimation of ion maximum energy: the dependence of electron average energy on nearcritical layer density and thickness is straightforward, thus also ion maximum energy has a similar dependence, an optimisation of electron energy will be connected to an optimised ion maximum energy. Therefore, one can compute optimised electron density and thickness of nearcritical layer to obtain maximum ions acceleration. In order to do so, what one can observe is that the greatest part of the hot electrons population is given by the nearcritical layer, due to the coupling between the laser pulse and the plasma. One can observe that in all the cases the highest predicted proton energy is reached when nearcritical layer thickness is around the self-focusing length of the laser inside the plasma:

$$d_{opt}^{nc} \simeq w_0 \left(\frac{\gamma_0 n_c}{n_e} \right)^{\frac{1}{2}}, \tag{1.37}$$

where n_e is the electron density of the nearcritical layer and w_0 is the laser waist. Being, then, the reflectance coefficient negligible in usual conditions, one can then compute the optimised nearcritical layer density as:

$$n_{opt}^{nc} \simeq 0.91 \gamma_0 n_c \left(\frac{\lambda}{w_0 \sqrt{2 \ln 2}} \right)^2 \left(\tau_{FWHM} \frac{c}{\lambda} \right)^{\frac{2}{3}}, \tag{1.38}$$

where τ_{FWHM} is the laser pulse duration at the intensity full width at half maximum of the Gaussian pulse. These simple formulae can be greatly useful when approaching simulations or experiments to evaluate the optimal condition.

1.4. Foam-based nearcritical targets for TNSA

In order to reach densities such as the ones necessary in nearcritical layers of double-layer targets, in solid materials, the only way is relying on nanostructured materials. Nanostructured materials are porous materials which can reach a density orders of magnitude lower than the plain solid density. Their theoretical description, due to their chaotic origin, must rely on fractal theory. The first part of the following section will be focused on a brief introduction to fractals and their application in foam description, the second part will instead give an introductory description of the effects of foam-like nanostructures in laser-plasma interaction.

1.4.1. Foam parameters and theoretical description

When considering nanostructured materials, foam-like ones are among the most promising in many applications, such as fusion [52] or particle acceleration [40]. As introduced before, a theoretical way to describe foam-like structures is the fractal description. A central role in fractal studies is played by the power law relationship [53], i.e. $y(x) = cx^a$, that shows an important symmetry leading to a repetition of the shape of the function on all scales. When applying fractal description to foams central role will be played by the mass of the system which scales as $M \sim kL^{D_f}$, where L is the characteristic length scale, k is an amplitude related to physical processes in the creation of the foam structure and D_f is the so-called **fractal dimension**. Mass can then be related in fractal description to the density of the fractal as $\rho \sim M^{\frac{D_f - d}{D_f}}$, where d is the Euclidean dimension of the space. When considering a foam, it can be imagined as an ensemble of spherical nanoparticles which aggregates all together forming the fractal nanostructure, then one can relate its characteristic length scale to the number of nanoparticles in the aggregate as $N \sim (L/r_{np})^{D_f}$, where r_{np} is the nanoparticle radius. A measure of the characteristic length thus, can be obtained and one can define it as **gyration radius**, i.e. the radial distance at which one should concentrate the mass of all the aggregate to have the same moment of inertia of the real object. From now on, when referring to the characteristic length, thus to the gyration radius, the symbol R_g will be used in order to have a more specific symbol for a fundamental quantity in the description of the foam. When considering a real foam, often the number of nanoparticles which compose it is really high and its structure can be seen in terms of the gyration radius of the aggregates creating the foam. Summarising the description shown before, one can obtain an estimation of the density of foam as follows [54]:

$$\rho_f = k\rho_{np}\left(\frac{r_{np}}{R_g}\right)^{3-D_f} \quad \text{where} \qquad R_g = r_{np}N^{\frac{1}{D_f}}, \tag{1.39}$$

where R_g is the gyration radius of the aggregate, r_{np} is the radius of the nanoparticle, ρ_{np} is the density of the nanoparticle and N is the number of nanoparticle in the aggregate.

The fractal dimension and the scaling coefficient hold all the physics of the foam growth process; analysing thus the fractal dimension one can distinguish two families of aggregation: the *reaction-limited aggregation*, where the aggregation process is limited by the sticking probability of one particle to another. Being the probability low, particles have a higher probability to move in different positions creating denser foams, it is common to see this process in chemical foams; the *diffusion-limited aggregation*, where the aggregation

process is limited by the Brownian motion happening during the diffusion of the particles: when they get in contact they aggregate. It is common to retrieve this process in PLD foams, thus its numerical modelisation will be later on explained. They can be easily recognised, in fact, due to their different fractal dimension, the theoretical investigation of reaction-limited foams results in a fractal dimension of 2.05 [55], while the diffusion-limited ones show a fractal dimension of ~ 1.7 [56]. Real foams, however, usually show a fractal dimension that is in between the two families, in PLD foams produced at Nanolab, for example, a fractal dimension around 2.0 is experimentally retrieved [54].

1.4.2. Effects of foam nanostructure

As anticipated in previous sections, foam nanostructure can have important effects when considering a laser pulse interacting with it. Even though the average density of a foam can be nearcritical, the nanoparticles composing it are overdense and the density inhomogeneities are in the order of laser wavelength. When using a high contrast laser, usually necessary for TNSA experiments, the nanostructure can still be present during the interaction, thus its effect becomes not negligible [57]. It is possible, in fact, to see that two are the main effects of the presence of a nanostructure, mainly observable when laser intensities are quite low, not allowing a fast homogenisation of the target: an increase of laser absorption, a different ion heating kinetic and a reduction of the maximum energy both of electrons and ions.

It is possible to justify the first effect in terms of the different propagation of the laser inside the nearcritical layer [58]: when considering a homogeneous layer, promptly, a sheet of increased electron density is created in front of the pulse. This layer can become overdense increasing laser reflection while propagation. A nanostructured material, having instead a shape alternating void and dense nanoparticles, allows propagation through the voids leading to increased absorption.

The second effect is instead due to the presence of nanoparticles the size of which is lower than laser wavelength: Coulomb explosion is the primary process to take into consideration to clarify it. A faster ion heating is, in fact, met due to the strong electric fields created in the Coulomb explosion, which will be briefly explained.

When a laser interacts with a plasma having a dimension smaller than its wavelength, it can blow out the electrons from the plasma. A strong electric field is created then due to the remaining positive charges. When considering a sphere, a geometry that can describe a nanoparticle of the foam, the electric field can be computed for a spherical layer moving

outward thanks to Gauss theorem:

$$\boldsymbol{E}(r_i(t)) = \frac{4}{3}\pi r_i^3(0) n_i \frac{Ze}{r_i^2(t)}, \tag{1.40}$$

where $r_i(0)$ is the position of the considered layer before the expansion, $r_i(t)$ is the position of the layer when the expansion starts, Ze is the charge of an ion and n_i is the ion density.

The last effect can then be explained by considering both Coulomb expansion and laser propagation inside a nearcritical plasma. High energy electrons are created due to the resonance effect in the nearcritical plasmas: when considering a nanostructured plasma this effect is however reduced. Then, due to the Coulomb explosion phenomenon, the relativistic self-focusing is suppressed, particularly for lower laser intensity [58].

2 | Numerical Modelling of Target Normal Sheath Acceleration

This second chapter has the scope to show the theoretical basis for the numerical simulations of laser-matter interaction. Firstly the relativistic kinetic model for plasmas will be shown: its numerical solution is however needed to account for all the non-linearities of laser-plasma interaction, thus the Particle in-cell (PIC) method for its solution will be proposed. Although PIC simulations are reliable, their computational cost may be a source of constraints on their use: low dimensionality simulations are then necessary to be able to perform parametric scans, i.e. large sets of simulations exploring the impact of some input parameters. Nevertheless, the physics can change when symmetry constraints are imposed to lose dimensionality effects, thus methods to characterise the reliability of the results and to extrapolate important parameters from lower dimensionality simulations are needed: a method to take into account 2D effects in PIC simulations is then shown. The PIC method is an algorithm based on a collisionless and classical model of plasma: when one would like to consider also quantum or collision effects in a plasma, Montecarlo methods are generally needed. Methods to take into account field ionisation, collision and impact ionisation are presented. The last part of the chapter is, instead, focused on general algorithms to simulate fractal materials, such as foams, which can be used to produce more realistic inputs for full-dimensionality PIC simulations.

2.1. Particle in-cell (PIC) approach to relativistic collisionless plasmas

In order to deeply understand the physics behind the interaction between high-intensity lasers and plasmas, analytical models are surely useful, but a great loss of information on the processes is unavoidable. Simplified relativistic fluid models cannot, in fact, describe properly all the non-equilibrium effects present in such conditions. A solution of more complex models, such as the relativistic kinetic model, seems then necessary: analytical solutions are however not available except for a few simple cases, thus one should rely

on numerical simulations. Two main approaches to numerical simulations are nowadays the most common: *phase-space grid* methods and *particle* methods. In this section, the latter will be the focus: the so-named *Particle-in cell* approach will be introduced and its mathematical basis will be shown.

2.1.1. Relativistic kinetic model for plasmas

When treating the interaction between a high-intensity laser and a target, due to the high energy of particles, particularly when considering electrons the energy of which can reach dozens of times their rest energy, one should surely take into account relativistic effects. Considering, then, that high-intensity lasers usually have very short pulses, around the order of femtoseconds, while collision relaxation times are in the order of picoseconds, also non-equilibrium effects have to be taken into account: to do so one should rely on the kinetic models of the statistical physics. Starting by first principle equations, which allows getting to the so-called *Klimontovich equations* [59], considering in first approximation that every kind of short-range collision could be neglected, due to the hypothesis on the relaxation time, one can get to the so-called Vlasov system of equations, which is named after the first scientist who studied a way to have a self-consistent model for a plasma [60]:

$$\begin{cases} \dfrac{\partial f_\alpha}{\partial t} + \boldsymbol{v} \cdot \dfrac{\partial f_\alpha}{\partial \boldsymbol{x}} + q_\alpha \Big[\boldsymbol{E} + \dfrac{1}{c}(\boldsymbol{v} \wedge \boldsymbol{B}) \Big] \cdot \dfrac{\partial f_\alpha}{\partial \boldsymbol{p}} = 0 \\ div(\boldsymbol{E}) = 4\pi \sum\limits_\alpha q_\alpha \int f_\alpha d^3\boldsymbol{p} \\ div(\boldsymbol{B}) = 0 \\ curl(\boldsymbol{E}) = -\dfrac{1}{c}\dfrac{\partial \boldsymbol{B}}{\partial t} \\ curl(\boldsymbol{B}) = \dfrac{1}{c}\dfrac{\partial \boldsymbol{E}}{\partial t} + \dfrac{4\pi}{c} \sum\limits_\alpha q_\alpha \int \boldsymbol{v} f_\alpha d^3\boldsymbol{p} \end{cases} , \tag{2.1}$$

where $\boldsymbol{p} = m_\alpha \gamma \boldsymbol{v}$ in order to be relativistically invariant and f_α is the distribution function, defined as the mean number of particles in a position $\boldsymbol{x}$ with a momentum $\boldsymbol{p}$. When one would like to consider also collisions between particles the right-hand side term of the first equation in the system of equations must be changed as follows, to account for the collision one would like to consider:

$$\frac{\partial f_\alpha}{\partial t} + \boldsymbol{v} \cdot \frac{\partial f_\alpha}{\partial \boldsymbol{x}} + q_\alpha \Big[\boldsymbol{E} + \frac{1}{c}(\boldsymbol{v} \wedge \boldsymbol{B}) \Big] \cdot \frac{\partial f_\alpha}{\partial \boldsymbol{p}} = \Big(\frac{df_\alpha}{dt} \Big)_{coll}. \tag{2.2}$$

Some strategies for modelling the collision term can be found in *chapter 7* of *Kinetic Theory of Nonideal Gases and Nonideal Plasmas* by *Klimontovich Y.L.* [61]: many of them relies on considering further moments in the averaging process needed to obtain the equation (2.2) for the distribution function. Collision terms turn out to be the key terms to reach plasma equilibrium.

2.1.2. Particle in-cell approach: potentialities and weaknesses

PIC approach to the solution of fluid motion has been studied since 1955 [62] in order to be able to consider non-equilibrium effects in fluids, i.e. when kinetic models are necessary. The particle in-cell approach is part of the family of particle methods used to solve transport equations. Particle methods turned out to be extremely useful in plasma physics: already in 1962 *Dawson J.* [63] developed a numerical electrostatic model which was able to predict Debye screening and Landau damping using plasma sheets as computational particles. The use of PIC methods as a way to solve the relativistic collisionless model for plasmas, i.e. the Vlasov-Maxwell system of equations, grew during those years and various theoretical analyses of the method, in order to characterise its behaviour in various conditions, were performed [64]. Different numerical implementations have been developed over the years, each method presents its pros and cons. The description of the implementations chosen during the thesis work will be discussed in section (3.2.2). This section will instead be dedicated to introducing the PIC method for relativistic collisionless plasmas and its mathematical justification following *Kinetic Plasma Simulations: Particle in-cell* by *G. Lapenta* [65].

Firstly one should distinguish between a *strongly coupled system* and a *weakly coupled system*: the first is a system in which the number of particles is not high enough to screen a perturbation on a single particle, thus all the system is affected by small perturbations; the latter is a system in which the number of particles is high enough to screen the effects of a single particle: collective effects become predominant. A plasma, the plasma parameter of which approaches zero, can be usually considered a weakly coupled system, meaning that, in first approximation, one can neglect interaction happening below Debye length. This approximation is the one allowing to consider collisionless plasmas.

In the PIC method, the (2.1) system of equations is the starting point. The basic idea is to evaluate the plasma species distribution function as a sum of different distribution functions:

$$f_\alpha(\boldsymbol{x}, \boldsymbol{p}, t) = \sum_p f_{\alpha-p}(\boldsymbol{x}, \boldsymbol{p}, t), \tag{2.3}$$

where $f_{\alpha-p}(\boldsymbol{x}, \boldsymbol{p}, t)$ is the distribution function of the different elements which can be regarded as macroparticles. In this sense, particle in-cell method can be seen as a *finite element method*. Each distribution function is then assumed to have a specific form given by the tensor product of the shape in each direction of the phase space multiplied by a parameter which is the number of particles N_p that a single macroparticle represents

$$f_{\alpha-p}(\boldsymbol{x}, \boldsymbol{p}, t) = N_{\alpha-p} S_x(\boldsymbol{x} - \boldsymbol{x}_{p-\alpha}(t)) S_p(\boldsymbol{p} - \boldsymbol{p}_{p-\alpha}(t)). \tag{2.4}$$

If f_α is a solution of the Vlasov equation, $f_{\alpha-p}$ must be a solution to the same equation where the electromagnetic field still depends on the whole f_α. The functions $S_x(\boldsymbol{x} - \boldsymbol{x}_{p-\alpha}(t))$ and $S_p(\boldsymbol{p} - \boldsymbol{p}_{p-\alpha}(t))$ are respectively called *spatial shape function* and *momentum shape function*, which are fundamental to describe the extension in the phase space of the macroparticles.

In order to solve numerically the equation, only the weak form solution of the equation is required for the macroparticle distribution function. In this way, shape functions can have whichever form, within some important characteristics which come from their definition: they shall describe a small region in the phase space, the integral along the domain must be unitary and, in order not to complicate the situation, a symmetric shape is preferable. The choice of the shape functions becomes, then, important in having a better agreement between simulations and analytical solutions: a fluctuating behaviour is shown by codes when wrong distribution functions are chosen [64].

For what concerns space shape functions, the choice usually falls onto Dirac delta or b-splines functions. The first choice is usually avoided nowadays since it has been seen to be a source of noise in the simulations: being point-like particles, macroparticles in the simulations can be subjected to big angle collisions when they get too close to each other. This effect is instead reduced when considering a distributed macroparticle: the overlapped part of two macroparticles is automatically neglected in field calculation, creating then a filter for short distance interactions which can be added a posteriori in a controlled way using different methods. In this sense, it is said that PIC solves the collisionless approximation of the relativistic kinetic model, even though still it is not totally clear which is the real equation solved by it.

For what concerns momentum shape functions, instead, the choice is generally unique: a Dirac delta function is chosen for the macroparticle distribution function in order to be sure all particles inside it behave in the same way, i.e. they remain close in phase space during the evolution. The request for the shape function $f_{\alpha-p}$ is to satisfy the equations for the moments of the Vlasov system of equations. This solution brings to

solving Newton-like equations for each of the macroparticles.

In the relativistic case these latter equations can be written as [66]:

$$\frac{dN_{p-\alpha}}{dt} = 0, \tag{2.5}$$

$$\frac{d\boldsymbol{x}_{p-\alpha}(t)}{dt} = \boldsymbol{v_{p-\alpha}}(t) = \frac{\boldsymbol{p_{p-\alpha}}(t)}{\gamma_{p-\alpha}(t) m_\alpha}, \tag{2.6}$$

$$\frac{d\boldsymbol{p}_{p-\alpha}(t)}{dt} = q_\alpha \left(\boldsymbol{E}(\boldsymbol{x}_{p-\alpha}, t) + \frac{\boldsymbol{v}_{p-\alpha}(t) \wedge \boldsymbol{B}(\boldsymbol{x}_{p-\alpha}, t)}{c} \right), \tag{2.7}$$

where $\gamma_{p-\alpha}$ is the relativistic gamma factor associated with the macroparticle of the species α, $\boldsymbol{E}(\boldsymbol{x}_{p-\alpha}, t)$ is the electric field averaged on the macroparticle shape function, $\boldsymbol{B}(\boldsymbol{x}_{p-\alpha}, t)$ is the magnetic field averaged on the macroparticle shape function, q_α is the species particle charge and m_α is the species particle mass. Macroparticle motion is usually solved numerically by employing time finite-difference. This step is usually called *particle pusher* as it is shown in figure (2.1).

The following step to obtain a self-consistent numerical solution of the Vlasov system of equation is the so-called *density and current deposition*. The macroparticles need to be used to retrieve the quantities necessary to solve the Maxwell equations, i.e. the current and charge densities. A general idea of how macroparticles can be used in order to retrieve them is the following:

$$\rho(\boldsymbol{x}, t) = \sum_\alpha q_\alpha \sum_{n_\alpha} N_{p-\alpha} S(\boldsymbol{x} - \boldsymbol{x}_{p-\alpha}(t)), \tag{2.8}$$

$$\boldsymbol{J}(\boldsymbol{x}, t) = \sum_\alpha q_\alpha \sum_{n_\alpha} N_{p-\alpha} S(\boldsymbol{x} - \boldsymbol{x}_{p-\alpha}(t)) \boldsymbol{v}_{p-\alpha}, \tag{2.9}$$

where n_α is the total number of macroparticles that samples species α.

Maxwell equations can be then solved in different ways in the step called *Maxwell solver*. Among all, the most common ways to solve them are the *finite difference* or the *finite volume*. A numerical grid for the spatial domain is then needed: the name particle in-cell comes then from this, particles move along a domain made by cells. In the treatment, then, particles can move independently from the spatial grid. A numerical algorithm to gather information given by the different equations is then needed: this can be done by means of a loop in which particles deposit density and current, Maxwell equations are then solved using the deposited quantities retrieving the electromagnetic field.

The electromagnetic field is interpolated in the end to be correctly used in particle motion equations in the so-called *field gathering* step. The interpolation is performed by averaging

the field on the macroparticle shape.

A visual scheme of the loop is presented in figure (2.1). The various processes strongly differ based on modelling and numerical choices: a deeper treatment of the used strategies will be shown later on in (3.2.2).

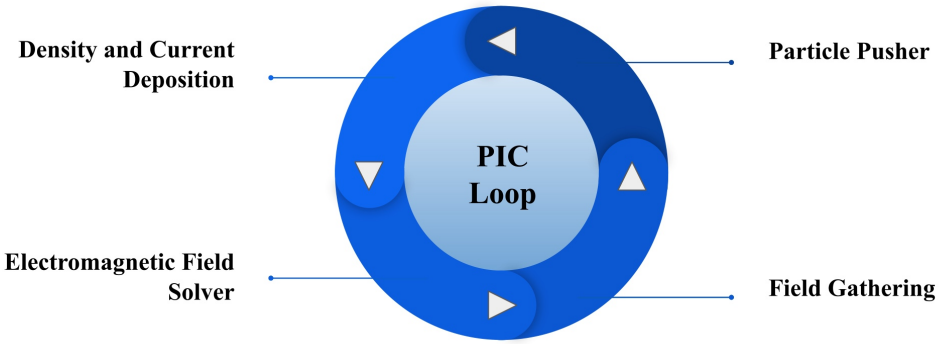

Figure 2.1: Schematic visualisation of the PIC loop. The main steps of the loop are shown in their logical order.

2.2. Dimensionality effects in Particle in-cell simulations

Low dimensionality particle-in-cell (PIC) simulations have been widely used to understand the physics behind particle acceleration by laser interaction. The choice of low dimensionality simulations comes from their lower computational cost with respect to full dimensionality problems, though the knowledge of some parts of the physical processes may nevertheless be lost due to constraints on particle motion. Therefore the knowledge of their limitation is important in order to understand which are the features that can be studied with those kinds of simulations. [24]

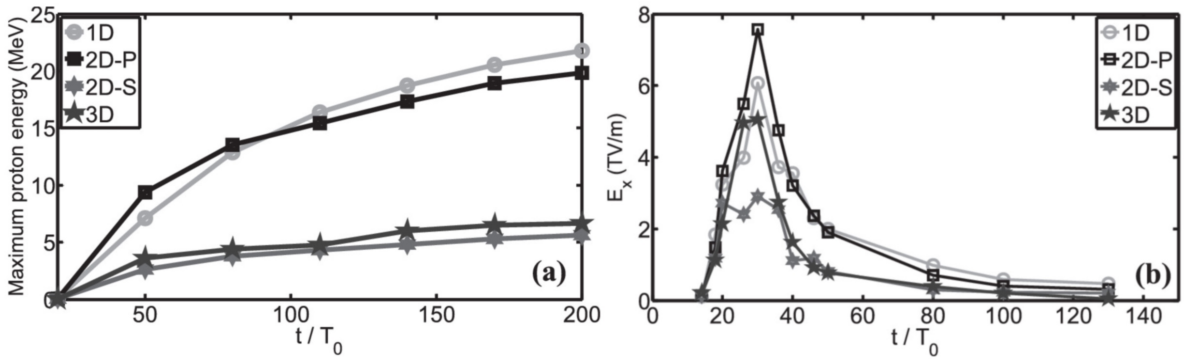

Figure 2.2: Maximum proton energy and electric field growth in time in 1D, 2D and 3D simulations with different polarisation. Source: [67].

Focusing on TNSA in laser interaction with solid targets, it is well known in the literature that the reduction of the motion of electrons in certain directions might influence the electric field felt by ions (see figure (2.2)-(b)). The electric field is, in fact, strictly related to electron density and temperature. A simple quasi-static model for a plasma sheath can, in fact, show that the maximum electric field is related to electron motion as follows [68]:

$$E_{max} = \frac{T_e}{e\lambda_{De}} \tag{2.10}$$

where $\lambda_{De} = (T_e/4\pi e^2 n_e)^{1/2}$ is the Debye length introduced in (1.2.1). The enhancement of hot electron re-circulation effects, which take place in 2D and 1D simulation due to the smaller emitting angles, increases electron density behind the target, allowing for higher proton acceleration in long time behaviour.

Also the effect of laser propagation within the target results in a different acceleration field in lower dimensionality: firstly, one has to take into account the effect of a Gaussian laser pulse spatial profile which is lost when considering a 1D case, secondly the effect that a circular spot can have with respect to a 2D case one.

The first effect becomes important, particularly in the first time instants of the acceleration, when focusing of laser happening both in 2D and 3D simulations due to the conical shape formed by laser interaction with the target, increases electron energy. [67]

The second effect is instead important in the electric field created behind the target due to electrons acceleration: considering again sheath electric field, particularly in the first time instants, the ratio between the electric field in a 2D and a 3D geometry can be expressed as: [69]

$$R_{sheath} = \frac{E^{2D}_{sheath}}{E^{3D}_{sheath}} = \left(\frac{\pi\sigma}{2}\right)^{\frac{1}{2}} \tag{2.11}$$

where σ is the laser waist. This effect, determined by the differences in the geometry taken into account, is then reflected on the maximum proton energies (see figure (2.2)-(a)): same ratio happens to appear in those. From the results shown in figure (2.2) for the 2D-S case, many differences can nonetheless be encountered when in a 2D simulation laser polarization is normal to the plane of incidence: this effect is mainly due to the reduction of re-circulation effects that are manifested instead in the case of p-polarization.

Due to these effects, generally, 2D simulations have been used to understand the basic physics of ion acceleration and to investigate the most efficient condition to increase maximum ion energy while keeping constant laser parameters; no quantitative knowledge on maximum ion energy is usually given by 2D simulations and 3D simulations are necessary to extrapolate this value. 2D simulations, in fact, mainly because of the electromagnetic scalar potential profile, which can be approximated as the one of an infinite thread [46] $\Phi \sim -\ln(r)$, create a monotonically increasing trend on proton energy, which does not seem to reach a plateau [70]. Due to the lower computational cost of 2D simulation, some effort has been put in order to get some quantitative knowledge on proton energy and to have a unique choice of simulation time in which extracting ion energy spectra. In *Babaei et al.* [71] the TNSA model by *Schreiber* [68] has been adapted to a 2D geometry to analyse ion energy trend, relating it to 3D geometry one.

2.2.1. Electrostatic model for TNSA to account for dimensionality effects

The 3D Schreiber model is based on an approximation of the field felt by maximum energy contaminant ions moving along their trajectory. After some approximations, the following relation for the scalar field [68] can be retrieved. The basic hypothesis is that the positive surface charge left on the target by the escaping electrons is the main contributor to the motion of the contaminant ions which reaches the maximum energy. The following equation represents the spatial behaviour of the scalar potential:

$$\Phi\left(\frac{z}{R}\right) = 2\pi R\sigma\left(\sqrt{1+\left(\frac{z}{R}\right)^2} - \frac{z}{R} - 1\right) \tag{2.12}$$

where z is the direction normal to target surface, R is plasma radius and σ is the positive surface charge density. Considering the equation of motion for a particle, the energy conservation, and approximating the field for long distances, a temporal trend for ions energy can be computed:

$$E(t) \simeq E_\infty\left(1 - \frac{t^*}{t}\right) \tag{2.13}$$

As one can see, an asymptotic constant value is reached when time goes to infinity. Different behaviour is seen instead in a 2D geometry, where charge density has to be modelled as an infinite stripe. In such a case, the scalar potential can be written as:

$$\Phi\left(\frac{z}{R}\right) = -4R\sigma \ln\left(1 + \frac{z}{R}\right) \tag{2.14}$$

which gives a temporal trend for ion energy that can be approximated as follows:

$$E(t) \simeq E_\infty \ln\left(\frac{t}{t^*}\right) \tag{2.15}$$

Fitting the maximum proton energy of a 2D and a 3D simulation at the same target and laser conditions gives almost the same energy factor E_∞, which allows having a criterion to stop 2D simulations and extract a more reliable ion energy spectrum [70].

2.3. Ionisation models in PIC: Monte Carlo method

Since quantum effects and collisions are not directly contained in PIC simulations, different models have been studied in order to include them. Many of the adopted strategies are based on the insertion of a Monte Carlo module inside the PIC loop, where the process that one wants to account for is simulated using proper probability distributions. The Monte Carlo module is generally added in the PIC loop after the calculation of the position of the macroparticles: following the distribution given by the process, random macroparticles will experience the processes taken into consideration. A representative scheme of the loop is shown in figure (2.3).

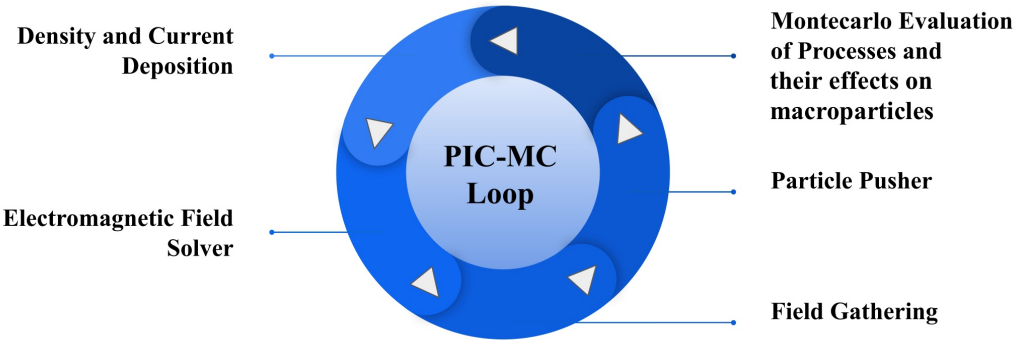

Figure 2.3: Visual scheme of the PIC-Montecarlo loop. All the steps are shown in their logical order.

The choice of which macroparticles will experience the process, just like in usual Monte

Carlo codes, is left to random number generators: rejection methods will be used in order to keep the correct probability distribution of the process inside the code. In order to do so, the choice of the right process probability distribution becomes of high importance. Models to take into account interesting processes such as photon emission, ionisation and collisions have been developed over the years. In the next section, the modelisation of the *Ammosov-Delone-Krainov (ADK) ionisation* process will be shown. For what concerns the ADK model, the ionisation takes place thanks to the presence of an external electric field which modifies the atomic band gaps allowing a tunnel effect; the impact ionisation model takes into account, instead, the effect of an electron impinging on an atom. Both the ionisation models take into account quantum effects which have to be modelled throughout macroscopical cross-sections.

2.3.1. ADK theory for field ionisation

ADK theory models field ionisation exploiting the following assumptions: firstly, external electric field amplitude (E) should be orders of magnitude lower than atom electric field one (E_{at}). Secondly, the energy of the quantum associated with the emitted photon energy in atom de-excitation (ε_ω) should be orders of magnitude lower than the atomic energy gap (I_p). These assumptions permit the quasi-classical approximation. Lastly, the adiabatic approximation can be used, i.e. the variation of the electric field (ω) is orders of magnitude lower than the ionisation frequency (ω_t), thus electric field can be considered constant when the ionisation process is happening, neglecting the variation of the potential during it. The ionisation rate is derived, then, as the mean rate in a field period. These hypotheses were used by *A. M. Perelomov*, *V. S. Popov* and *M. V. Terent'ev* [72] to evaluate the ionisation rate of a hydrogen atom in an external electromagnetic field. In the hypothesis that electron motion is not relativistic when ionisation happens, one can neglect, in first approximation, the effects of the magnetic field in the atom. The bound electrons will encounter during their motion due to the external field, three regions: the first region, when it is near the nucleus, in which atomic potential is higher than the external electric field which,thus can be neglected, a region in which the fields are in the same order of magnitude and a last external region in which electrons are out from the potential barrier and the feel the atomic field far from the nucleus, reducing to a coulomb field exerted by the charge Z of the nucleus, and the external field. In this context, it is possible to use a quasi-classical approximation to solve the motion in the potential barrier and evaluate the probability of ionisation per unit time for a static external field,

considering for all the treatment $\hbar = m_e = e = 1$:

$$p_{static}(E) = C^2_{n^*,l^*} I_p \frac{(2l+1)(l+|m|)!}{2^{|m|}(|m|)!(l-|m|)!} \left(\frac{2E_{at}}{E}\right)^{2n^*-|m|-1} e^{\left(-\frac{2E_{at}}{3E}\right)}, \tag{2.16}$$

where $E_{at} = (2I_p)^{\frac{3}{2}}$ is the atomic electric field, $n^* = Z(2I_p)^{-\frac{1}{2}}$ is the effective quantum number, l^* is the effective orbital quantum number, l is the orbital quantum number and m is the projection of l along the direction of the field. C_{n^*,l^*} is a coefficient which can be calculated by solving the Schrödinger equation for the atom and the external potential, in the region of the potential barrier; in this first treatment, which involves the solution of Schrödinger equation the solution for the equation is known only for s-levels of the hydrogen atom. *Ammosov M. V.*, *Delone N. B.* and *Kraïnov V. P.* [73] extended the theory to atoms different from hydrogen, in which also a non-Coulombian residual potential is present, due to the high number of electrons and computing C_{n^*,l^*} also for different orbitals. The latter result was obtained by providing the C_{n^*,l^*} coefficients considering an atom (ion) in the absence of an external field in the quasi-classical approximation, valid when $n^* \gg 1$. Considering again the potential barrier region for a general atom and in this case using the semiclassical approximation, one can compute the radial wave function. The definition of an effective value of the orbital quantum number is then needed to take into account the effects of multiple electrons as $l^* = n_0^* - 1$ where n_0^* is the effective principal quantum number of the ground state of the atom. Thus it is possible to obtain the following $C^2_{n^*,l^*}$ for the static probability of ionisation:

$$C^2_{n^*,l^*} = \left(\frac{4e}{n^{*2} - l^{*2}}\right) \left(\frac{n^* + l^*}{n^* - l^*}\right)^{l^*+\frac{1}{2}} \frac{1}{2\pi n^*}, \tag{2.17}$$

where e is the Euler number. Then, one can express the atomic field felt by the electron as:

$$E_{at} = \frac{Z^3}{n^{*3}}, \tag{2.18}$$

obtaining a general relation for tunnel ionisation probability in a static external electric field. To consider the effect of an external magnetic field one can use again the adiabatic approximation. It is important, however, to observe two results of the treatment: firstly, when considering a state with $|m| > 0$ the probability of tunnel ionisation is at least 3 orders of magnitude lower than the case of m=0, allowing to neglect all the ionisations happening for the former cases; secondly, the treatment firstly developed in semiclassical approximation, being theoretically valid only for $n \to \infty$, has been experimentally shown to be reliable also for lower values of n.Then, using adiabatic approximation, one can compute the average value of the probability of ionisation in an elliptically polarised

electromagnetic wave using a prefactor for the static probability which can be computed as follows:

$$A(E,\omega,\epsilon) = \left[\frac{\epsilon(1+\epsilon)}{2}\right]^{-\frac{1}{2}} e^{\frac{1-\epsilon}{3\epsilon}\frac{E_{at}}{E}} I_0\left(\frac{1-\epsilon}{3\epsilon}\frac{E_{at}}{E}\right), \tag{2.19}$$

where ϵ is the ellipticity of the electromagnetic wave, E is in the sinusoidal form typical of the electromagnetic wave and I_0 is the Bessel function of imaginary argument. When the polarisation results far enough from the circular one, i.e. $\epsilon \to 0$. The ionisation rate is:

$$p(\epsilon,\omega,E) = \left(\frac{3}{\pi}\frac{1}{1-\epsilon^2}\frac{E}{E_{at}}\right)^{\frac{1}{2}} p_{static}(E). \tag{2.20}$$

When the wave is circularly polarised the prefactor A is unitary and $p = p_{static}$: this happens since the electric field amplitude remains constant in a circularly polarised wave.

2.4. Numerical models for nanostructured foams

To properly describe the interaction between a laser and the nanostructured layer of the DLTs presented in section (1.3.2), one cannot neglect the morphology [74] of the nanostructure. In figure (2.4) some Scanning Electron Microscope (SEM) images of different real foams are shown.

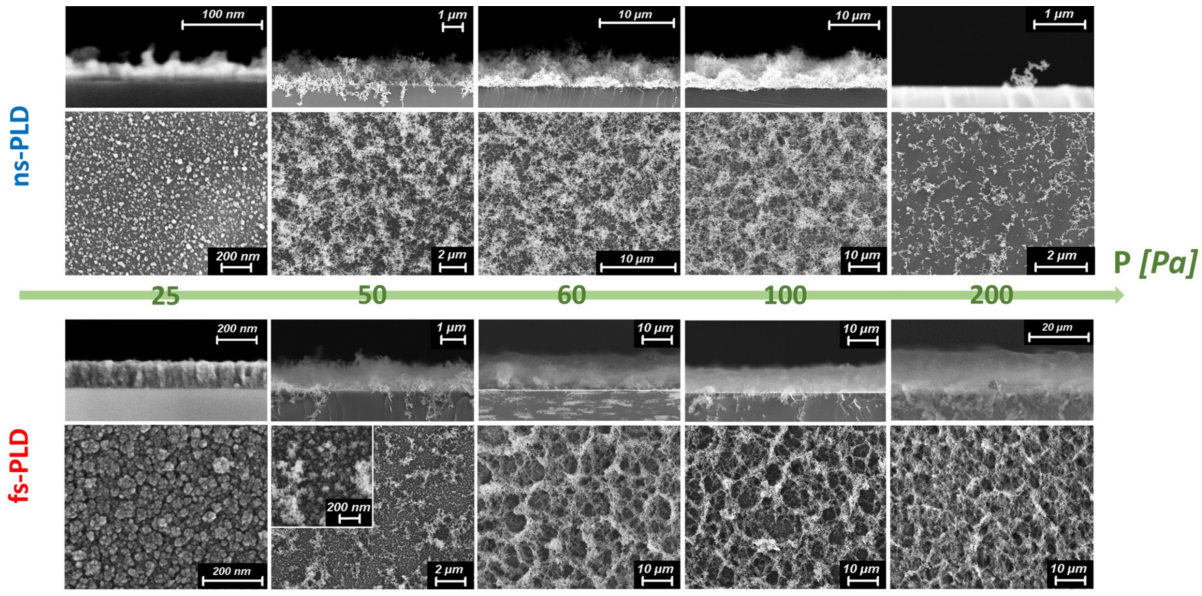

Figure 2.4: Examples of Scanning Electron Microscope (SEM) front and cross-sectional images of nanostructured foams typical of DLTs. Source: [54].

Thus, the numerical description of a porous material is necessary. The description of such materials in a deterministic way is not straightforward and well known, however, simple

Montecarlo codes allow a good reproduction of structures seen in nanostructured materials. The basis of these Montecarlo algorithms is the reproduction of the movement of a particle when diffusing up to the formation of an aggregate. The bases of those algorithms is then the simulation of the Brownian motion of the nanoparticles forming the nanostructured materials and the simulation of the right sticking probability between two particles. These models, then, can be considered non-equilibrium models and have to be studied kinetically [53]. The asymmetry and random nature of the process which characterise the growth of fractal materials is mostly related to non-equilibrium conditions which lead to the irreversible sticking of particles. The majority of the interesting structures in material physics can be studied in terms of near equilibrium processes, in which symmetries hidden by their fractal description can be found [75]. The models which are presented in the following fall into this kind of processes. Many models have been studied, each of them with a different degree of complexity. All of them, nevertheless, are based on stochastic processes. Among the most known one can find the *lattice animals model* [76], based on the growth around the last occupied site in a lattice given by a pre-determined probability, the *random walks models* [77], in which the growth is based on the pattern followed by a random-walker around a starting site, the *Eden model* [78], in which the perimeter of the formed cluster is occupied randomly by a new particle at each step, the *reaction-limited aggregation model (RLA)* [79], in which the cluster grows upon collisions between two particles which have a determined probability of sticking, the *cluster-cluster aggregation model (CCA)* [80], in which particles and clusters move ballistically in a lattice until they collide and stick together, the *diffusion-limited aggregation model (DLA)* [56], in which the random walk of a particle leads to its sticking to a preformed cluster and the *diffusion-limited cluster-cluster aggregation model (DLCCA)* [81], which can be considered a CCA in which clusters and particles move performing random walks. In figure (2.5) it is possible to see examples of clusters created using different models.

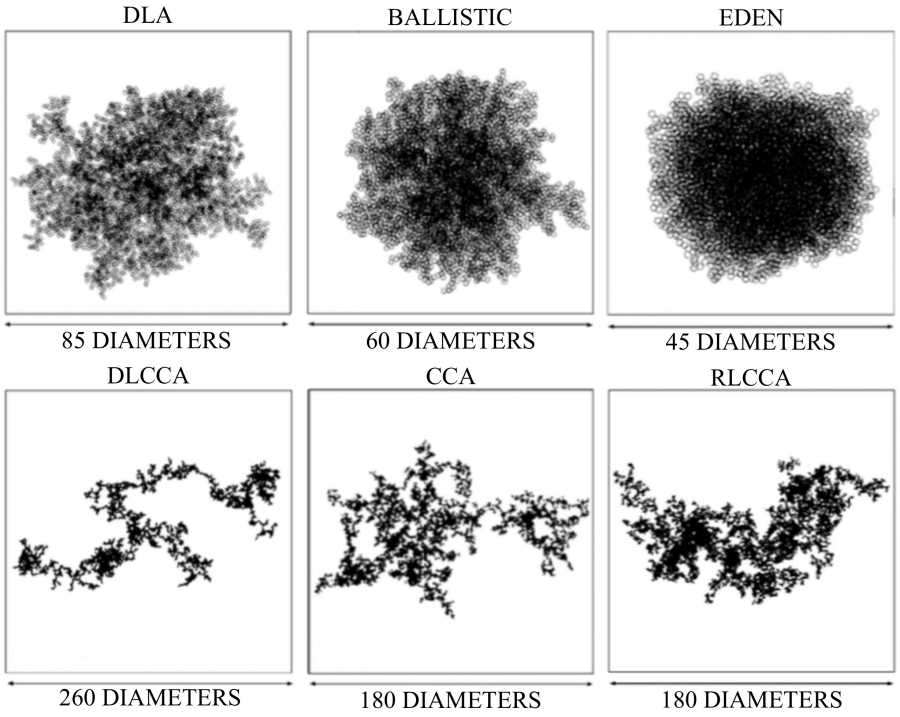

Figure 2.5: Examples of 3D numerical aggregates derived from different aggregation models. Adapted from: [53].

The next sections will be focused on the introduction to the diffusion-limited aggregation family.

2.4.1. Diffusion-Limited Aggregation model

The Diffusion-limited aggregation model was first developed by *Witten T. A.* and *Sander L. M.* [56] in 1981 in order to describe the formation of fractal aggregates of nanoparticles during the condensation of a metal from its vapour phase. The idea came from realising that once particles have formed an aggregate, they coalesce irreversibly. An explanation of the process of formation of such clusters can be given in terms of diffusion of the particles. When interaction potentials are lower than the average kinetic energy of the particles, in fact, their thermal motion, and thus their diffusion, will play the main role in their behaviour. In this sense the formation of the aggregates is dominated by diffusion and therefore called diffusion-limited. In order to explain the growth of a cluster it is necessary to simulate the diffusion of the particles. This process, from a statistical point of view, can be simulated in terms of random walk [82]:

$$p(\boldsymbol{x}, t_{k+1}) = \frac{1}{c} \sum_{\boldsymbol{l}} p(\boldsymbol{x} + \boldsymbol{l}, t_k), \tag{2.21}$$

where $\boldsymbol{x}$ is the position in a lattice, k is the k^{th} time-step, c is the number of neighbour cells of $\boldsymbol{x}$, $\boldsymbol{l}$ is the space step needed to reach the neighbour cells and $p(\boldsymbol{x}, t_k)$ is the probability that a particle finds itself at time t_k in position $\boldsymbol{x}$. To simulate, then, the aggregation one should account for the sticking probability of a particle which, while performing a random walk, encounters another particle: in DLA the choice is to keep this probability unitary, meaning that whenever a particle touches the boundary of another particle, it attaches to the other forming an aggregate. The probability of attachment will be higher in zones in which the radius of curvature of the perimeter of the occupied region is higher, i.e. once a dendrite is formed, it will be more probable for the particles to attach there. In order to simulate the processes that have just been described the choice of *Witten* and *Sander* was to place at the origin of a lattice an immobile particle and then to insert randomly other particles, one at a time, which diffuse thanks to a random walk. Whenever the particle touches the perimeter of an occupied site, it will attach to the ones which were already present in the lattice creating in this way a cluster. Once the particle has attached to the cluster, the random walk is restarted with a new particle. It has been proven for such clusters the universality of their power law description for the cluster mass $M \sim L^{D_f}$, a typical feature of critical phenomena such as the DLA. The fractal dimension D_f for the DLA cluster has been estimated to be around $D_f \simeq 1.7$.

2.4.2. Diffusion-Limited Cluster-Cluster Aggregation model

Diffusion-limited cluster-cluster aggregation model was developed by *Meakin P.* [81] as a combination of the DLA model and CCA model. When considering cluster formation in the DLA algorithm, the initialisation is given by a particle which is fixed in the origin of a lattice and all the other particles move toward it. This kind of process is in some way unlikely to happen in cluster formation. Thus to better represent the physical process, as in CCA, a conspicuous number of particles is initialised at first in the lattice and due to motion led to attach forming a unique cluster. In CCA the motion was a ballistic motion, while in DLCCA a random walk is performed. The particle motion can happen in two different ways [83]:

- in a *lattice model*, i.e. all the particles are led to move in the lattice, when two of them get in contact they are attached forming a cluster, which then moves in a random walk. This model tries to mimic the diffusion in a dense fluid;
- in an *off-lattice model*, in which two particles are randomly chosen and then led to diffuse off-lattice forming a cluster. This cluster can then be chosen again randomly to diffuse and attach to the others.

Both models show the same fractal dimension ($D_f \simeq 1.8$), but the second seems to reproduce in a better way the structure of real clusters. Again, in principle, when a cluster diffuses, its higher mass should decrease its mobility in random walks, leading to smaller steps. However, the numerical results show that no important differences are seen when the consideration of the reduction of mobility is accounted for in numerical simulations [81].

3 | Objectives and Methods of the Thesis Work

This chapter is devoted to the presentation of the motivations, the objectives and the methods which pose the bases for the thesis work. In the first section, the background leading to the development of the work will be presented together with a description of the goals to be pursued. The second section is instead dedicated to the illustration of the methods used to obtain the results needed to achieve the targets of the thesis work.

3.1. Motivations and objectives of the thesis work

After the presentation of the main topics concerning the laser interaction with matter, it is important to summarise the context in which this thesis work arises. The interaction of high-intensity lasers with matter can be used to accelerate different kinds of particles or to produce electromagnetic radiation [84]. Among all, a great interest is placed in the acceleration of low-mass ions. Many methods have been developed over the years to achieve such an objective, surely the use of solid targets has been one of the main focuses of the investigation. To increase the efficiency of the process, the production of non-conventional nanostructured targets was one of the ways which were followed. Their use and theoretical description require precise modelling, which is hardly feasible via analytical models only. When restricting to Double Layer Targets (DLTs), the importance of modelling the nanostructure of the low-density layer positioned on the front of a metallic film has been demonstrated by numerous studies [85]. Thus, an assessment of the modelling of such targets is needed. When focusing on the TNSA process, the use of targets such as DLTs has been proven to be crucial in enhancing laser energy absorption and it has opened the possibility to design interesting proton sources even by using TW-class laser facilities. Lasers of TW-class have the great advantage to be very compact. Indeed, even table-top lasers can deliver a peak power of this order of magnitude. Sources from compact lasers were proven to be suitable for applications such as air pollutant characterisation [86] and they could be used also in other fields, such as cultural heritage conservation, by means

of analysis techniques like laser-driven PIXE [87]. The high grade of non-linearity of the processes happening when a laser interacts with the matter makes the use of analytical models impossible to capture all the physics behind the process. Therefore, the use of numerical tools becomes fundamental to having a deep understanding of it. The use of analytical models is, then, restricted only to the context of estimating some fundamental quantities, like the maximum energy of the accelerated protons. Laser-plasma interaction falls, in fact, onto a relativistic kinetic description. Relativistic, since even with compact lasers the electrons can reach energies in the order of their rest mass. Kinetic since only a kinetic description is able to capture all the non-equilibrium effects which are typical of the process. The only way to solve such a description is the use of computer simulations: among all, the particle in-cell (PIC) method is the most established. The results obtained in computer simulations can be used to optimise and better understand experimental activities, thus they can be complementary to them. The right way to model the interaction of TW-class lasers with plasmas via PIC simulation, however, can be not as straightforward as for higher-intensity lasers. In fact, processes such as ionisation can play an important role when the laser pre-impulse is not intense enough to cause a complete ionisation of the target. Thus, an analysis of their influence and a standardisation of the modelling choices when treating compact lasers is needed. Also, the high computational cost of realistic three-dimensional simulations makes it necessary to make large use of lower-dimensional simulations. Two-dimensional simulations are generally performed to investigate the optimal conditions for enhancing the conversion of laser energy into low-mass ion one. However, the results retrieved from such simulations cannot be used to extract quantitative data and the use of the resource demanding three-dimensional simulations is still needed.

In this context, the work done for this thesis aims to find a solution to some of the just presented open questions. The objective of the work can be summarised by the following list:

- finding a way to be able to construct numerical foam nanostructures which present the desired density and thickness;
- determining the optimal and more reliable way to simulate the interaction between a compact laser and the target which developed in three different fields:
    1. evaluating the effects of ionisation processes in plasmas during the interaction with compact lasers;
    2. evaluating the effects of lower-dimensionality in the simulations and trying to define a method to extract quantitative data from two-dimensional PIC

simulations;

3. evaluating the effects of the presence of the nanostructure when considering a compact laser;

- demonstrating the feasibility of laser-driven proton sources with class-TW lasers. The investigation had two main scopes:

1. evaluating the optimal target when considering a laser the power of which is in the order of tens of TW;

2. determining the best laser and target configuration when considering a commercial sub-TW laser.

The objectives will be fulfilled by using specific codes and methods which will be presented in the following section.

3.2. Numerical tools used during the thesis work

A proprietary code, which allows the growth of DLA or DLCCA numerical foams, was used with the scope of simulating the nanostructure of foams. A great variety of modelling choices in the definition of cluster motion or in the definition of the number of particles per cluster is included in the code. Since the code works in a serial process and the RAM requirements are not too high, the simulations were performed on a personal computer.

Two different numerical tools were used with the scope of simulating the interaction between a laser pulse and a target: Smilei [88] and WarpX [89]. Both the codes are particle in-cell codes which allow a high grade of parallelisation of the processes, an important feature to optimize the use of computational resources. In order to be able to perform realistic simulations in reduced real-time, then, the use of supercomputers is necessary. All PIC simulations of the thesis work were performed on two clusters hosted by CINECA, a large high-performance computing facility in Bologna, Italy: the Intel cluster GALILEO100 and the accelerated cluster MARCONI100. The first is a *Dual-Socket Dell PowerEdge* cluster which is equipped with 528 computing nodes, each containing 2 *Intel CascadeLake 8260* CPUs, with 24 cores running at 2.4 GHz. Each computing node is also equipped with 384GB RAM. The second cluster is instead an accelerated cluster based on *IBM Power9* architecture and *Volta NVIDIA* GPUs. Each computing node is equipped with two *IBM Power9 AC922* CPUs; each of it contains 16 cores, running at 3.1 GHz and is accelerated by four *NVIDIA Volta V100* GPUs with 16 GB of dedicated memory and connected to each other and to CPUs with *Nvlink 2.0*. Each computing node is equipped

with 256GB RAM. The use of an accelerated cluster greatly reduces the computational time needed to perform a simulation. The choice of the used numerical tools is due to their characteristics. They are, as a matter of fact, both fully relativistic, open-source and multi-purpose particle in-cell codes, which include Monte Carlo packages to simulate quantum and collision effects and allow the choice among different numerical strategies.

3.2.1. Numerical tools for foam modelling

The numerical foam generation tool is a C++ code, which creates a DLCCA foam taking some user-defined parameters as input. The user-defined parameters include the transverse dimensions of the foam D, the number of clusters to be deposited N_{clust} and the mean number of particles per cluster $\langle N_{particles} \rangle$, as well as different choices in the distribution of the number of particles per cluster and in the mechanism of deposition of the formed clusters to create a numerical foam. Before explaining the workflow of the code, a scheme that summarises the principle of the loop is presented in figure (3.1).

The first step being executed by the code is the initialisation of two arrays which will be fundamental in the cluster deposition process:

- a two-dimensional array which will contain the positions of all the particles composing a foam, which from now on will be called *deposit*;
- a four-dimensional array which will be used as a grid for the deposition. Three of the four dimensions will be used for determining a cell in a discretised volume, while the fourth dimension will be used for storing the indexes of the particles of the deposit which can be found within that grid cell. This array will be called *deposit grid* from now on.

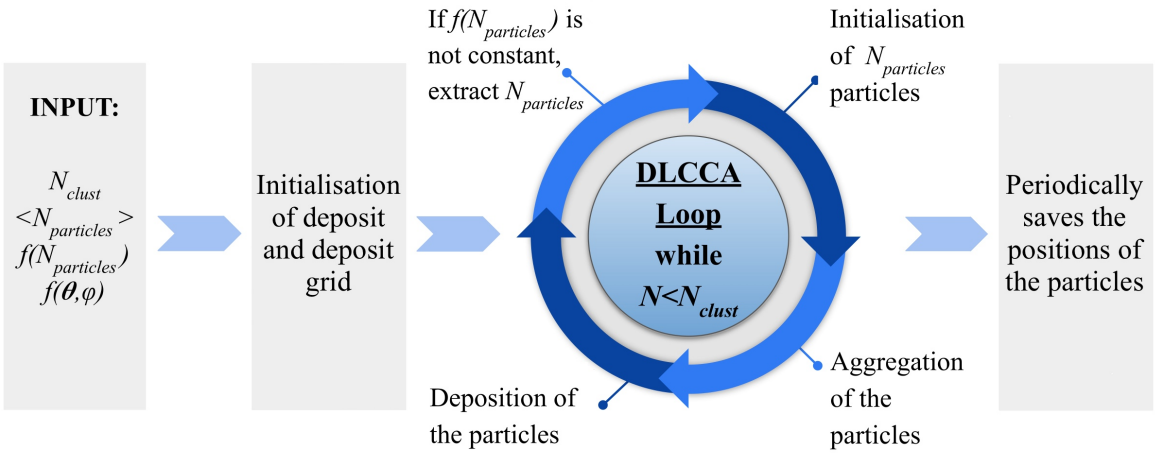

Figure 3.1: Schematic workflow of the DLCCA code.

To create the deposit grid, the user will have to set two parameters: a dimension which will be used for both the dimensions transverse to the deposit direction D and a ratio which will be used to calculate the longitudinal dimension of the deposit grid. In order not to have boundary effects in the longitudinal dimension, one should carefully choose this ratio, taking into consideration the thickness of the foam that one would like to simulate.

After the initialisation of the variables needed for the cluster deposition, a cycle starts to aggregate and deposit $N_{cluster}$ clusters. For each cluster in the first place, the initialisation of a precise number of particles is needed: the number of particles to be initialised depends on the mean number of particles per cluster $\langle N_{particles} \rangle$ and the choice of the probability distribution chosen for the mean number of particles per cluster $f(N_{particles})$. Two are the possibilities: a fixed number of particles equal to $\langle N_{particles} \rangle$ or a sampling of $N_{particles}$ from an exponential distribution the mean value of which is $\langle N_{particles} \rangle$. The aggregation then starts and follows an off-lattice DLCCA algorithm which does not account for the different mobility among clusters and particles [83] until a unique cluster is formed. No angular diffusion is, however, considered. After the conclusion of the aggregation process, the deposition one starts. Then the cluster is initialised in the deposit grid: a random position is chosen for its centre along the transversal directions. Concerning the longitudinal position, the centre is placed higher than the maximum height of the already deposited foam of at least a particle diameter more than the maximum radius of the cluster. The deposition is now started and two possible choices can be taken: a ballistic motion of the cluster in the negative longitudinal direction or a diffusive motion which can happen only downward. The motion stops when a particle of the cluster enters a grid cell of the deposit grid in which the number of first neighbours is different from zero. The cluster is

then moved along the last sampled direction until it does not reach contact with a particle of the deposit. At this point, the cluster undergoes two rigid rotations which lead it to reach three contact points with the deposit.

The deposit is periodically printed in text files during cluster deposition. These files can, then, be read by Ovito [90] to visualise the numerical foam in the growth process.

3.2.2. PIC-Montecarlo loop: numerical strategies and tools

The numerical tools chosen for PIC simulations, both permit the use of different algorithms devoted to the solution of both the equations for the macroparticles and electromagnetic field. In order to be coherent in the choices and to be able to compare the simulations, the choices on the used solvers are the same for both tools, therefore they will be presented before showing the characteristics which are specific for the single tool.

Choice of the spatial shape function for macroparticles

As explained in section (2.1.2), when one performs PIC simulations (using Smilei and WarpX), the choice of the macroparticle shape is among the most important in obtaining smooth and realistic results. The common choice is the use of the B-splines functions. Such functions are polynomial functions in the space which are normalised to unity.

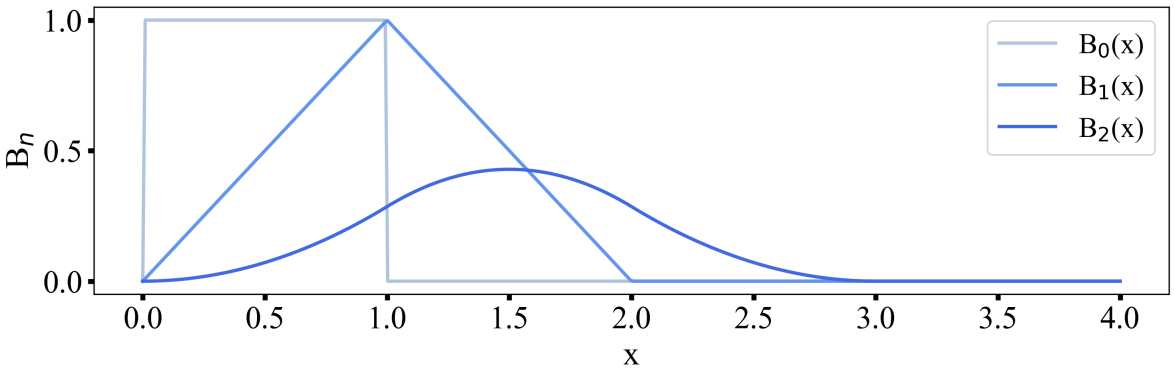

Figure 3.2: Order one, two and three one-dimensional B-splines.

The order of the B-spline is defined as one more than the higher order polynomial power and can be obtained by successive integrations of the first-order B-spline, which in one dimension is defined as follows:

$$B_0(x) = \begin{cases} 1 & |x| < 1 \\ 0 & \text{elsewhere} \end{cases} . \tag{3.1}$$

The usual choices in PIC codes are the first and the second order ones. As one can observe in figure (3.2), this choice is due to the compactness of the first two orders: higher order B-splines usually present long tails which can badly influence the results, leading to a too high reduction of the interaction among the macroparticles.

In this thesis context, the choice was to use the second-order B-spline in order to have a smoother profile, reducing, then, the simulation noise. The macroparticle spatial shape functions have the measuring unit of a number density of particles.

Density and Current deposition

Before the solution of Maxwell equations, to evaluate the self-induced electromagnetic field the charge density and current due to the macroparticles have to be reconnected to the spatial grid associated with the field itself. For what concerns the charge density deposition, the equation (2.8) is used: for each point of the grid, the sum of all the contributions to charge density due to the macroparticles is performed. In one dimension one can, thus, compute the density at each node as follows:

$$\rho^n_{\alpha_i} = \frac{q_\alpha}{\Delta x} \sum_p N_{p-\alpha} \int_{x_{i-1/2}}^{x_{i+1/2}} S(x - x^n_{p-\alpha}) dx, \tag{3.2}$$

where q_α is the species charge, Δx is the space discretisation and $N_{p-\alpha}$ is the number of particles represented by the macroparticle. The most straightforward method to deposit the current on the grid could be similar to the one used to deposit the density, following the discretised equation (2.9). It is possible, though, to demonstrate that such a method does not guarantee charge conservation. In one dimension the solution to the conservation of charge equation or continuity equation leads to a quite simple method to deposit the current which is:

$$\frac{\rho^{n+1}_{\alpha_i} - \rho^n_{\alpha_i}}{\Delta t} = \frac{J^{n+1/2}_{\alpha_{i+1/2}} - J^{n+1/2}_{\alpha_{i-1/2}}}{\Delta x} \tag{3.3}$$

For three or two dimension cases, the solution to this equation is not as straightforward, thus algorithms which allow a solution for the charge conservation equation are needed: the choice falls into the algorithm developed by *Esirkepov T. Zh.* [91] which guarantees charge conservation computing the fluxes of particles entering and exiting the considered grid cell.

Maxwell solver

The solver of Maxwell equations is based on a *second order finite difference time domain (FDTD)* method [92]. The method was first proposed by *Yee K. S.* [93] as a numerical way to solve three-dimensional electromagnetic problems that, especially because of their

boundary conditions, were difficult to solve analytically. The method is based on the use of a second-order centred finite difference to approximate the derivatives in Maxwell equations: the so-called *leap-frog scheme* [94].

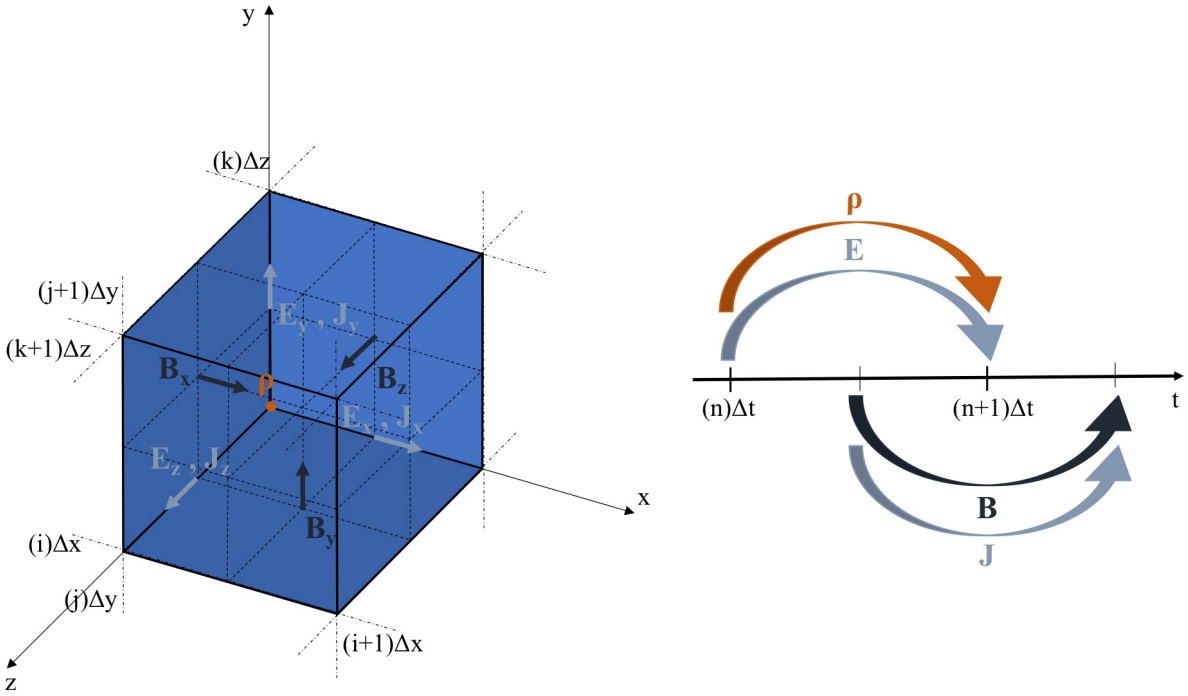

Figure 3.3: Visualisation of the leapfrog algorithm in space and time.

To do so, in the first place it is necessary to define a space grid. In each cell of the grid two points are present: the nodes of the spatial grid, identified by the triplets i, j, k and the half grid nodes, identified by the triplets $i+\frac{1}{2}$, $j+\frac{1}{2}$, $k+\frac{1}{2}$. The i nodes range from 0 to N_x and represent positions which are equally spaced by Δx. An analogous discussion can be made for j and k nodes which represent respectively y and z axes. The process, then, works on *staggered grids*, which are shifted by half-cell along the three spatial directions. The same approach is used in order to discretise time which is indicated by n. By applying the leapfrog scheme to Maxwell equations, thus, one obtains the quantities related to the electromagnetic field, which must be evaluated as follows:

$$\begin{aligned}
\boldsymbol{E}(\boldsymbol{x},t) &\approx \left[E^n_{x_{(i+1/2)jk}},\, E^n_{y_{i(j+1/2)k}},\, E^n_{x_{ij(k+1/2)}}\right],\\
\boldsymbol{B}(\boldsymbol{z},t) &\approx \left[B^{n+1/2}_{x_{i(j+1/2)(k+1/2)}},\, B^{n+1/2}_{y_{(i+1/2)j(k+1/2)}},\, B^{n+1/2}_{z_{(i+1/2)(j+1/2)k}}\right],\\
\boldsymbol{J}(\boldsymbol{x},t) &\approx \left[J^{n+1/2}_{x_{(i+1/2)jk}},\, J^{n+1/2}_{y_{i(j+1/2)k}},\, J^{n+1/2}_{z_{ij(k+1/2)}}\right],\\
\rho(\boldsymbol{x},t) &\approx \rho^n_{ijk},
\end{aligned} \tag{3.4}$$

where $\boldsymbol{E}(\boldsymbol{x},t)$ is the electric field, $\boldsymbol{B}(\boldsymbol{x},t)$ is the magnetic field, $\boldsymbol{J}(\boldsymbol{x},t)$ is the current

density and $\rho(\boldsymbol{x}, t)$ is the charge density. To have a graphical interpretation of how the leapfrog scheme works, see figure (3.3). It is not necessary to solve Maxwell divergences equations: if they are satisfied at the initial time, they remain valid provided that the continuity equation is satisfied for all times. Thus the code will solve only Ampère-Maxwell and Faraday equations. In a one-dimensional treatment, Maxwell curl equations will reduce, thus, to:

$$\begin{cases} B_{x_i}^{n+1/2} = B_{x_i}^{n-1/2}, \\ \dfrac{B_{y_{i+1/2}}^{n+1/2} - B_{y_{i+1/2}}^{n-1/2}}{c\Delta t} = \dfrac{E_{z_{i+1}}^{n} - E_{z_i}^{n}}{\Delta x} \\ \dfrac{B_{z_{i+1/2}}^{n+1/2} - B_{z_{i+1/2}}^{n-1/2}}{c\Delta t} = -\dfrac{E_{y_{i+1}}^{n} - E_{y_i}^{n}}{\Delta x} \\ \dfrac{E_{x_{i+1/2}}^{n+1} - E_{x_{i+1/2}}^{n}}{\Delta t} = -4\pi J_{x_{i+1/2}}^{n+1/2} \\ \dfrac{E_{y_i}^{n+1} - E_{y_i}^{n}}{c\Delta t} = -\dfrac{B_{y_{i+1/2}}^{n+1/2} - B_{y_{i-1/2}}^{n+1/2}}{\Delta x} - \dfrac{4\pi}{c} J_{y_i}^{n+1/2} \\ \dfrac{E_{z_i}^{n+1} - E_{z_i}^{n}}{c\Delta t} = \dfrac{B_{y_{i+1/2}}^{n+1/2} - B_{y_{i-1/2}}^{n+1/2}}{\Delta x} - \dfrac{4\pi}{c} J_{z_i}^{n+1/2} \end{cases} \tag{3.5}$$

Such numerical approach to Maxwell equations, however, imposes a relation between space and time discretisation, which is known as *Courant-Friedrichs-Lewy (CFL)* condition for stability [95]:

$$c\Delta t \sqrt{\frac{1}{\Delta x^2} + \frac{1}{\Delta y^2} + \frac{1}{\Delta z^2}} < 1. \tag{3.6}$$

Field gathering to macroparticles

As one can observe in equation (3.8) the knowledge of the electromagnetic field acting on the macroparticles is necessary to be able to perform their motion. To do so, the average electromagnetic field felt by the macroparticle is computed as follows:

$$\boldsymbol{E}^n(\boldsymbol{x}_{p-\alpha}^n) = \int \boldsymbol{E}^n S(\boldsymbol{x} - \boldsymbol{x}_{p-\alpha}^n) d^3x \quad \text{and} \quad \boldsymbol{B}^n(\boldsymbol{x}_{p-\alpha}^n) = \int \boldsymbol{B}^n S(\boldsymbol{x} - \boldsymbol{x}_{p-\alpha}^n) d^3x. \tag{3.7}$$

Boris pusher for macroparticle motion

To compute macroparticle trajectories the used algorithm was an energy-conserving algorithm based on a leap-frog scheme to solve equations (2.6) and (2.7). This algorithm is

the so-called *Boris pusher* [96]:

$$\begin{cases} \boldsymbol{x}_{p-\alpha}^{n+1} = \boldsymbol{x}_{p-\alpha}^{n} + \dfrac{\boldsymbol{p}_{p-\alpha}^{n+1/2}}{m_\alpha \gamma_{p-\alpha}^{n+1/2}} \Delta t \\ \boldsymbol{p}_{p-\alpha}^{n+1/2} = \boldsymbol{p}_{p-\alpha}^{n-1/2} + q_\alpha \left(\boldsymbol{E}^n(\boldsymbol{x}_{p-\alpha}^n) + \dfrac{\boldsymbol{p}_{p-\alpha}^n \wedge \boldsymbol{B}^n(\boldsymbol{x}_{p-\alpha}^n)}{m_\alpha \gamma_{p-\alpha}^n c} \right) \Delta t \end{cases}, \tag{3.8}$$

where $\boldsymbol{x}_{p-\alpha}$ is the position of the macroparticle centre, $\boldsymbol{p}_{p-\alpha}$ is the macroparticle momentum, $\gamma_{p-\alpha}$ is the relativistic gamma factor, Δt is the simulation time-step and q_α is the species charge. The quantity $\boldsymbol{p}_{p-\alpha}^n$ is not known since the leap-frog algorithm computes the momentum of the macroparticle only at half-integers time-steps. Thus an approximation can be done by averaging the forward and the back time-steps of the momentum, leading after some approximations to:

$$\boldsymbol{p}_{p-\alpha}^n = \frac{1}{1+|\boldsymbol{b}|^2}[\tilde{\boldsymbol{p}}^n + \tilde{\boldsymbol{p}}^n \wedge \boldsymbol{b} + \boldsymbol{b}(\tilde{\boldsymbol{p}}^n \cdot \boldsymbol{b})], \tag{3.9}$$

where:

$$\boldsymbol{b} = \frac{q_\alpha \Delta t \boldsymbol{B}^n(\boldsymbol{x}_{p-\alpha}^n)}{2 m_\alpha \gamma_{p-\alpha}^n c}, \qquad \tilde{\boldsymbol{p}}^n = \boldsymbol{p}_{p-\alpha}^{n-1/2} + q_\alpha \boldsymbol{E}^n(\boldsymbol{x}_{p-\alpha}^n) \frac{\Delta t}{2} \quad \text{and} \quad \gamma_{p-\alpha}^n \approx \sqrt{1 + \frac{\tilde{\boldsymbol{p}}^n \cdot \tilde{\boldsymbol{p}}^n}{m_\alpha^2 c^2}}.$$

Boundary conditions

Many boundary conditions are usually implemented in PIC codes for particles:

- the *periodic boundary conditions*, where the particles which exit the domain re-enter it from the opposite side;
- the *absorbing boundary conditions*, where the particles which exit the domain are lost and cancelled from memory;
- the *reflecting boundary conditions*, in which the particles which exit the domain are reflected at the boundary.

For what concerns, instead, electromagnetic fields, usually the following boundary conditions are present:

- the *periodic boundary conditions*, the field is considered as periodic with a period equal to the length of the dimension considered;
- the *PML boundary conditions*, the field is absorbed at the boundary;

Field ionisation evaluation and back reaction

Field ionisation can be implemented in a PIC code, using a Montecarlo algorithm, following the scheme proposed by *Nuter R.* [97]. The scheme is based on the static rate of ionisation shown in equation (2.16) where the constant is given by equation (2.17). The atom electric field E_{at} shown in the formula, can be related to the ionisation potential as $E_{at} = (2I_p)^{3/2}$. Considering the electric field static in one time-step of the PIC loop, it is possible to compute from the ionisation rat the ionisation probability to singly ionise the ion over the time interval Δt:

$$P^i_{i-1}(\Delta t) = 1 - e^{-p^i_{i-1_{static}}(E)\Delta t)}, \tag{3.10}$$

where $p^i_{i-1_{static}(E)}$ is the ionisation rate computed with eq. (2.16) to ionise from the ionisation state $i-1$ to i and Δt is the PIC loop time-step. The probability that an ionisation happens with a magnetic quantum number different from zero is always neglected. This relation, however, allows taking into account only one single ionisation for time-step, while an atom can undergo more of them during the typical PIC time resolution. Therefore, in order to account for multiple ionisation probability, one should compute the cumulative probability function for the multiple ionisations that bring an ion from the ionisation state $i-1$ to k:

$$\begin{aligned} F^k_{i-1} &= \sum_{j=i-1}^{k} P^j_{i-1}(\Delta t) = \\ &= e^{-p^i_{i-1_{static}}(E)\Delta t} + \sum_{j=i}^{k}\sum_{p=1}^{j} \frac{e^{-p^{j+1}_{j_{static}}(E)\Delta t} - e^{-p^{p}_{p-1_{static}}(E)\Delta t}}{\left(1 - \frac{p^{j+1}_{j_{static}}(E)}{p^{p}_{p-1_{static}}(E)}\right)\Pi^j_{q=1,q\neq p}\left(1 - \frac{p^{p}_{p-1_{static}}(E)}{p^{q}_{q-1_{static}}(E)}\right)}. \end{aligned} \tag{3.11}$$

that can be derived under the hypotheses that each further ionisation of an atom happens in an interval of time shorter than the PIC time-step and that each ion concentration is kept untouched until the new time-step. One can, thus, obtain the probability of ionisation linearising (3.10). From a randomly generated number one can, then, estimate the ionisation state of the ion confronting it with the result of eq. (3.11). Energy conservation is guaranteed by imposing the following relations on the momentum of the electrons and the generated ion:

$$\boldsymbol{p}_e = \frac{m_e}{m_{A^{j+}}}\boldsymbol{p}_{A^{j+}} \quad \text{and} \quad \boldsymbol{p}_{A^{(j+1)+}} = \frac{m_{A^{(j+1)+}}}{m_{A^{j+}}}\boldsymbol{p}_{A^{j+}}, \tag{3.12}$$

and adding to the Ampere-Maxwell equations a current density related to ionisation that satisfies the following relation:

$$(\boldsymbol{J}_{ion} \cdot \boldsymbol{E})\Delta t = I_p, \tag{3.13}$$

where $m_{A^{j+}}$ is the mass of the ion to be ionised, $m_{A^{j+1}}$ is the mass of the ion produced after ionisation, $p_{A^{j+}}$ is the momentum of the ion before ionisation and $\boldsymbol{E}$ is the electric field. Including the J_{ion} contribution allows forcing the reduction in electromagnetic energy due to ionisation.

Smilei code

Smilei [88] is an open-source, highly parallelised and vectorised code. It is an object-oriented code based on C++, taking as an input file a Python-like code. Its outputs are saved in HDF5, an high-performance data software library. It is able to perform simulations in various geometries, such as cartesian one, two or three-dimensional geometries and cylindrical geometries. It allows different configurations of Maxwell solvers and boundary conditions. It is a relativistic PIC code, which has some additional physics modules such as field ionisation, Coulomb collisions and impact ionisation.

WarpX code

WarpX [89] is an open-source, highly parallelised code which can work also on GPU-accelerated computational units, allowing a high reduction of the computational time. It is a C++ based code, which reads AmreX-like inputs. As Smilei it is able to perform simulations in different geometries and with a wide choice of computational methods to solve the equations: however, even though many physical models are present, it cannot account for impact ionisations in plasma. It allows the initialisation of species from external files, however, this kind of initialisation can be done only within some memory limits which make impossible the initialisation of nanostructured plasmas when one would like to perform a full-dimensional simulation.

4 | Analysis and Characterisation of Numerical Foams

This fourth chapter is devoted to the presentation of the results obtained in the characterisation of numerical foams to be used both for realistic fractal material simulations and for the inclusion of the nanostructure in PIC simulations. The first section presents the set-up of the simulations of the numerical foams, the second shows the developed methods to characterise the numerical foams and the last section will be devoted to the presentation and discussion of the results.

4.1. Set-up of a parametric scan to characterise numerical foams

In order to characterise the morphology of the foams generated by the code mentioned in section (3.2.1), it is necessary to perform a scan of simulations. The characterisation has been restricted to the simplest cases, i.e. a monodispersed distribution $f(N_{particles})$ in the number of particles per cluster. The number of particles per cluster was highly varied since one can expect it to be the most influential parameter in producing foams of different densities. Foams having 1, 2, 5, 10, 20, 50, 100, 200, 500, 1000 and 2000 particles per cluster were produced. A set of simulations has been performed, thus, to characterise the foam production when the number of particles per cluster remains fixed in two different strategies for the deposition: the ballistic deposition and the diffusion-like deposition. In both cases, a simulation box with D of 500 particle diameters per dimension transversal to the deposition direction and 1000 diameters in the direction parallel to the deposition has been chosen. A high number of clusters N_{clust}, up to 500.000, was simulated in order to be able to produce different foam thicknesses. The output of each simulation was saved every time the aggregation of 100 clusters has completed, to be able to observe the growth of the foam.

4.2. Development of a tool to characterise a numerical foam

In order to be able to perform the characterisation of a numerical foam, numerical tools are needed to estimate the average density and thickness. To do so, I developed a tool which, taking as input a numerical foam generated from the code mentioned earlier, is able to characterise the foam. The method which was developed tries to reproduce the method proposed by *Meakin P.* [53] for the calculation of the average density and the experimental method to compute the thickness [98].

4.2.1. Estimation of the average density

In order to estimate the average density of the generated numerical foam, the choice is to create an algorithm which is able to sample various positions inside the foam and estimate the average density in each of them. The estimation of the average density is performed by computing the total mass in a cube around the sampled position and dividing it by the volume of the cube. In order to be sure to have a fully grown foam, in which the self-similar fractal propriety applies, the choice is to sample the density only below half the maximum foam height.

Being the length scale of the numerical foams normalised with respect to the nanoparticle diameter and considering that the mass of the particles does not influence the deposition, the particle radius and density have to be given as input to the density calculator. Also, the foam deposition box dimensions depend on the nanoparticle diameter which is given in input. Then, the code is able to read the particle positions and computes the maximum distance from the substrate plane among the particles composing the foam. The size of the edge of the cubes necessary to estimate the density is then chosen to be a quarter of the maximum distance from the substrate plane.

As one can observe in figure (4.1), once the size of the cube is defined, the positions in which evaluating the density are extracted. The extraction happens randomly for the cube centres: the positions are sampled within the box dimension along the transversal section, while within the lower half maximum height along the deposition direction. It is guaranteed that the cube always remains inside the box. The number of sample cubes is proportional to the ratio between the edge size of the cube and the box transversal size. The number of particles present inside each box is then computed and thus, knowing the particle radius and density, one can compute the total mass present inside the cube. The average density of the foam and its mean standard deviation are, at last, computed as a

mean among all the samples.

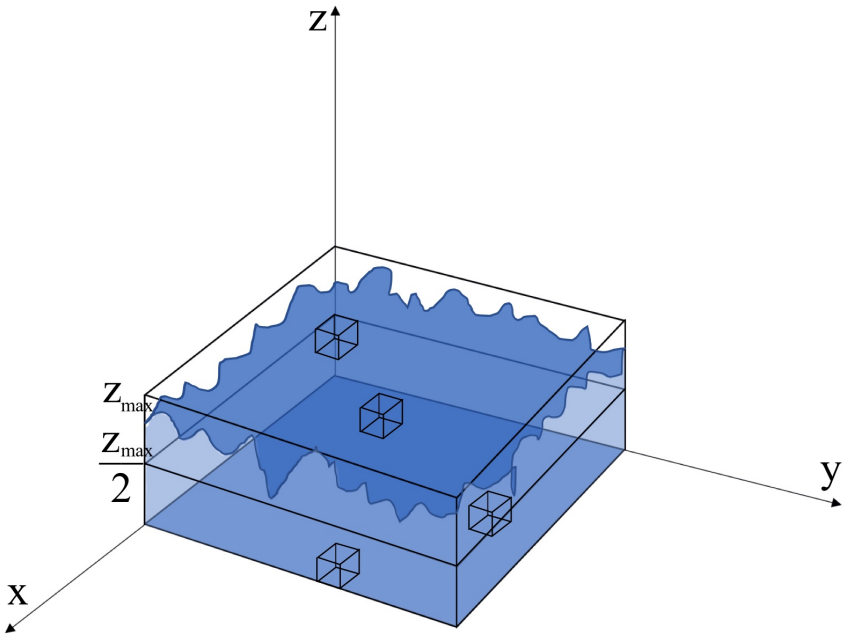

Figure 4.1: Visualisation of the working principle of the density calculator. A general numerical foam is represented in blue: z_{max} is its maximum height. The cubes represent the portion of space in which the foam density is sampled and computed by the code. The $z_{max}/2$ limit is the maximum height at which the foam is sampled.

4.2.2. Estimation of the average thickness

To simulate, instead, the experimental procedure to estimate the thickness of foams, it is necessary to have a cross-sectional image of the numerical foam. In fact, the experimental procedure uses scanning electron microscope (SEM) cross-sectional images to estimate the thickness of nanostructured foams. The thickness is retrieved as the average height of the SEM cross-section.

To do so, only two dimensions are accounted for: the deposition direction and one of the transversal directions. The length of the two dimensions is then divided into a grid the cell of which has a size equal to the diameter of a particle. The total number of particles having a position in which the two considered coordinates fall into the grid cell is then related to each position. As one can see in figure (4.2), for each position along the transversal direction one can find a maximum height, which will be related to the total number of particles which can be found in that slice of foam.

The scheme, then, performs a weighted average among the maximum heights to compute the foam thickness: the weight is given by the number of particles related to the position.

To take into account the possibility of having a height equal to zero in certain positions along the transversal direction, when no particles are present the code automatically assumes a null height for that region with a unitary weight.

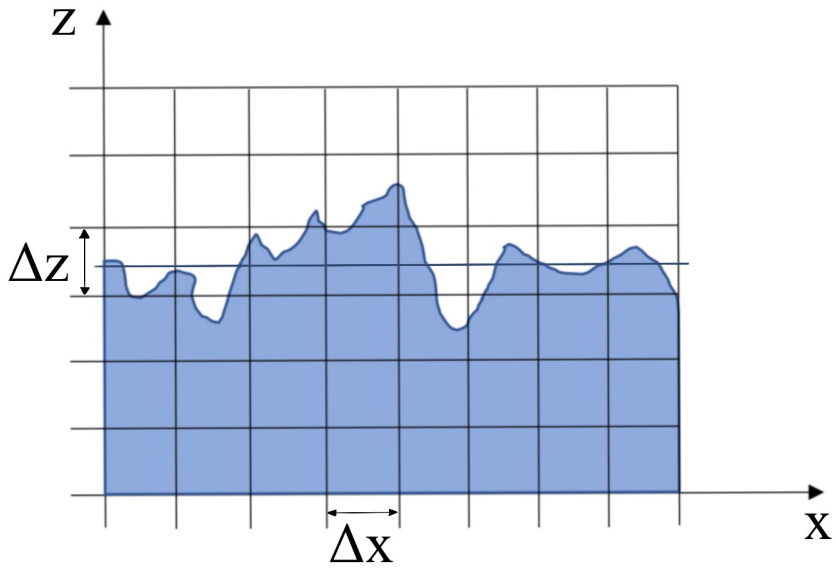

Figure 4.2: Visualisation of the working principle of the thickness calculator. The grid represents the x and z dimensions of the deposition grid of the foam. The grid cell is determined by the values Δx and Δz. The projection of the foam is represented by the blue shape, while the dark-blue line represents the thickness of the foam.

4.3. Analysis of the results

The simulated foams were then analysed in two different cases. Realistic foams, with a radius of the nanoparticle of 10.0 nm and a density equal to the graphite one, i.e. 390 n_c in units of critical density for a wavelength of 800 nm for the electron of the graphite considering the latter as a totally ionised material, and foams which can be used in particle in-cell simulations, i.e. with a radius of 25.0 nm and a total electron density of 25 n_c. The latter was computed in order to keep the total number of atoms in the particle constant with respect to the realistic one. The choice of using graphite density is justified by the fact that carbon is the most common element used in producing foams. Nevertheless, the same procedure can be performed using the density of whichever material, the results on the morphology, thus, do not lose their generality.

By observing the presented structures, one can realise that the results from the code can be subdivided into two different conditions. When the number of particles per cluster is higher than 10 the behaviour is the one of diffusion-limited cluster-cluster aggregated

foams. In figure (4.3) one can observe that when the number of particles per foam is lower than 10 the deposition process prevails on the cluster formation leading to tree-like foams when the diffusion of the cluster is activated, to ballistic foams when the clusters move ballistically.

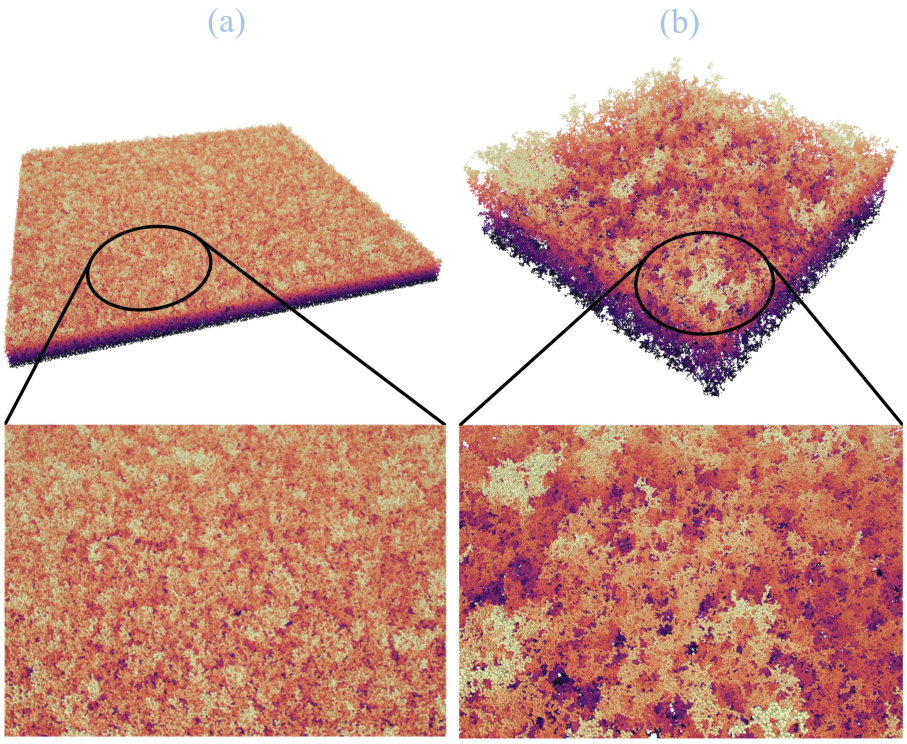

Figure 4.3: Three-dimensional visualisation of two different foams performed with Ovito [90]. In (a) a foam produced with one particle per cluster is presented, while in (b) a foam produced with a hundred particles per cluster. The particles which are positioned at a higher distance from the base of the foam are shown with a lighter colour.

4.3.1. Realistic numerical foams

By estimating the density as shown in section (4.2.1) it was possible to retrieve the results shown in figure (4.4). The *# of nanoparticles* shown in the figure is computed as the product between N_{clust} and $N_{particles}$. It is possible to note that for each case, after a transient moment which in all cases lasts until a number of 3 nanoparticles per D^2, the density reaches a saturation value. When the foam grows enough to show the fractal self-similarity propriety, the density becomes constant and can be seen as a function of the number of particles per cluster only. It is possible also to observe that the density shown by the ballistic deposition of the clusters is always higher than the one in the diffusive regime. This confirms the differences observed between the ballistic and the diffusion-

limited cluster-cluster aggregations: the fractal dimension of the second is, in fact, lower than the first, meaning lower lacunarity is associated with the ballistic aggregation model. It is possible also to observe an increasing trend in density with a decreasing number of particles per cluster, a trend which is justified by the relation shown in equation (1.39). Indeed, a higher number of particles per cluster leads to a higher gyration radius and, therefore, to a lower mean density.

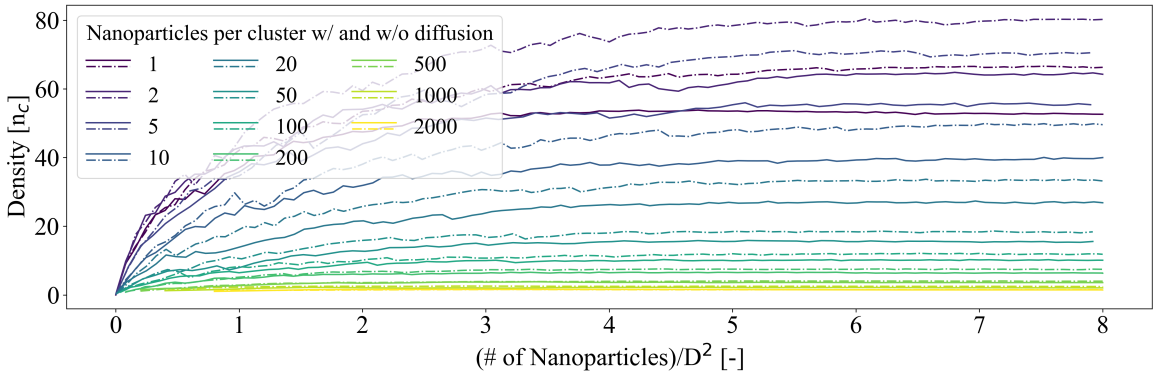

Figure 4.4: Plot of the estimated density with respect to the total number of particles per unit surface cell in the transversal dimension in different conditions in number of particles per cluster. The different colours represent the different number of particles per cluster.

This behaviour is, however, lost when the number of particles per cluster is lower than 10. The density remains almost constant in this region, meaning the hypothesis of the self-similarity between the foam density and the aggregated cluster density is not valid anymore. The deposition process is the one really influencing the foam growth. In fact, when $N_{particles} < 10$ the greatest difference between diffusion and ballistic deposition is observed.

In figure (4.5) the foam thickness behaviour with respect to the total number of particles composing the foam per unit deposition surface is shown for each case. One can observe that as expected for a constant density, a linear trend is present. It is also possible to note a saturation in the thickness for the foam composed of the biggest clusters: this saturation was due to the limitation in the box height which brought the code to a maximum thickness of 20µm. The foams showing lower densities present a larger increase in thickness.

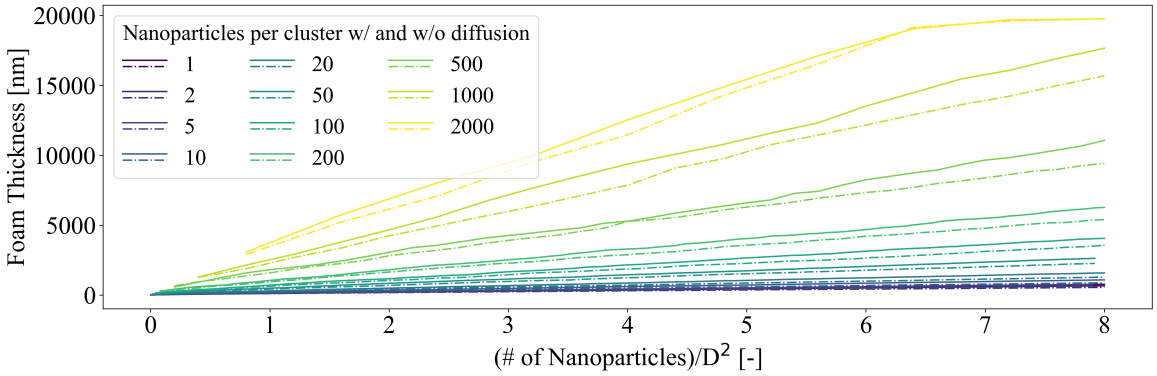

Figure 4.5: Plot of the estimated thickness with respect to the total number of particles $N_{clust} \times N_{particles}$ per unit surface cell in the transversal dimension in different conditions in number of particles per cluster. The different colours represent the different number of particles per cluster.

In order to analyse and characterise the foam, an estimation of the parameter k defined in equation (1.39) is necessary. Having, in fact, the knowledge of that parameter, it is possible to reproduce foams with the requested characteristics. Thus for each simulated case, the theoretical density associated with the clusters created by diffusion-limited cluster-cluster aggregation has been computed and a linear fitting among the foam estimated density and the cluster theoretical density has been performed obtaining the results shown in figure (4.6). The theoretical density was computed using the fractal dimension of the DLCCA process used for aggregating the clusters, i.e. D_f equal to 1.8. It is possible to observe that up to a number of particles equal to 10 the scaling almost perfectly matches the retrieved values, thus the produced foams show an almost perfect self-similarity with the forming clusters. One can also observe that two different values for k are retrieved for the two different deposition methods, meaning the different physical behaviour associated with them is included in k. When the values with a number of particles lower than 10 were inserted in the fitting, it was possible to observe a strong increase in the mean error between the fitting and the estimated density values due to large deviation from the linear trend. This error was generally higher for the values having the number of particles per cluster lower than 10. This effect can be explained as a loss of similarity between the foam and its forming clusters, therefore confirming the hypothesis above.

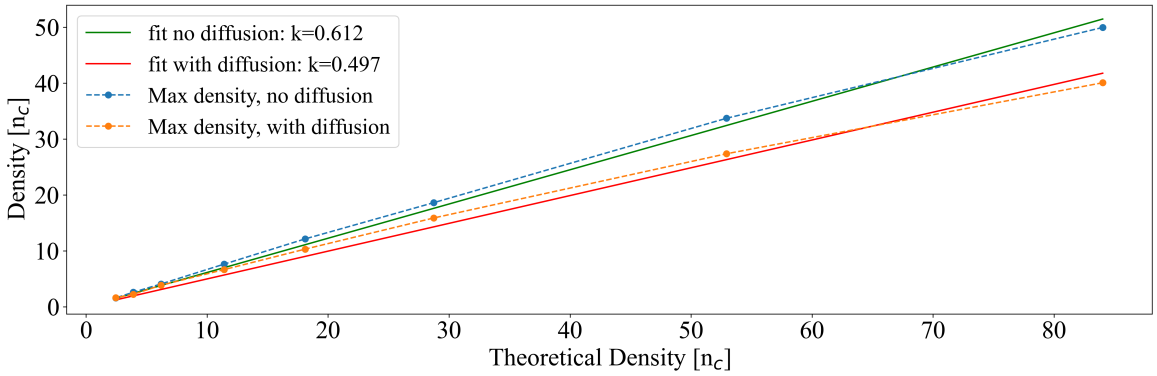

Figure 4.6: Plot of the estimated density with respect to the theoretical density of the cluster composing the foam, computed using a fractal dimension of $D_f = 1.8$ and a nanoparticle density of $\rho_{np} = 390.0$ n_c. The dotted line represents the connection between the saturated values from the simulations represented by the larger points, the continuous line the performed fitting. The description of what is represented by the different colours shown is explained in the legend, they are used to distinguish between the different deposition processes.

When the number of particles per cluster is reduced, the principal mechanism playing a role in the characteristics of the foam is not the cluster aggregation, but the deposition process. It is thus necessary for these values a proper estimation of the mean gyration radius and fractal dimension of the numerical foam after the deposition. However, since the densities reached by the numerical foams associated with such conditions are very high, such an analysis has not been carried out, being out of the scope of this thesis work. The retrieved values for the k coefficient are 0.612 when the deposition process is ballistic, and 0.497 when the deposition process is diffusive. The results are coherent with what is usually shown in the theory, the higher value in the coefficient for the ballistic deposition is, in fact, related to a higher density value, which is related to the higher fractal dimension of the ballistic aggregation. Also, one can observe that the values for k are comparable to experimental results which can be found in literature [54], meaning the code seems to well reproduce the realistic nanostructures.

Due to the independence from the particle radius and density of the code forming the numerical foams, the same comments made for the real foams can be made also for the foams which are useful for particle in-cell simulations.

In figure (4.7) the estimated foam density with respect to the total number of particles per unit deposition surface is shown.

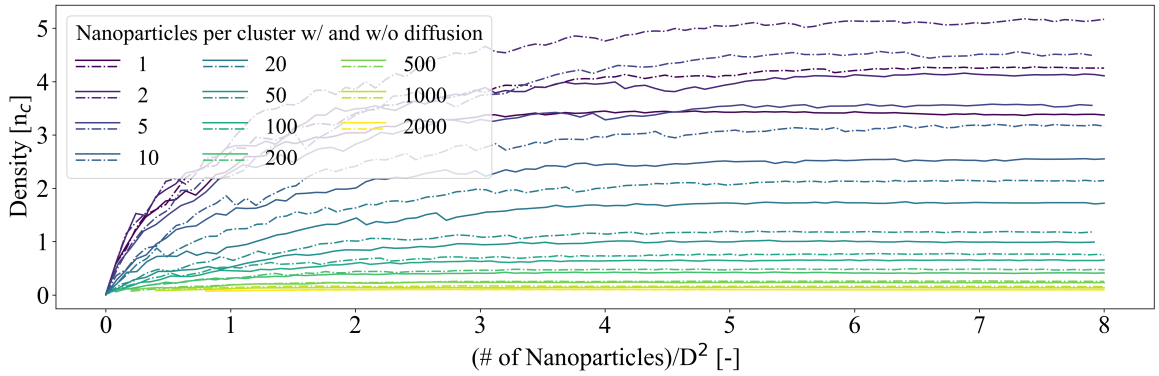

Figure 4.7: Plot of the estimated density with respect to the total number of particles $N_{clust} \times N_{particles}$ per unit surface cell in the transversal dimension in different conditions in number of particles per cluster. The different colours represent the different number of particles per cluster.

In figure (4.8), instead, the thickness evolution with respect to the total number of particles per unit surface is presented.

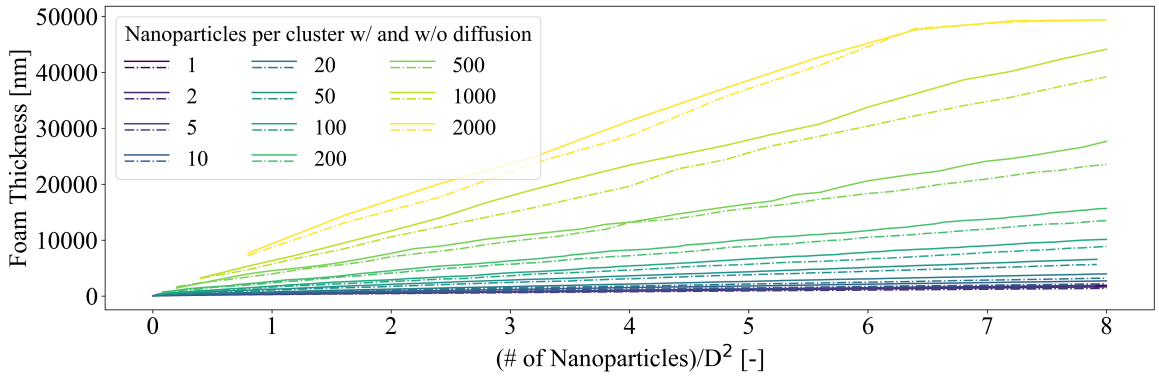

Figure 4.8: Plot of the estimated thickness with respect to the total number of particles per unit surface cell in the transversal dimension in different conditions in number of particles per cluster. The different colours represent the different number of particles per cluster.

5 | Analysis of Modelling of the TNSA with TW-Class Lasers

This chapter is devoted to the presentation of the particle in-cell simulations performed during the thesis work and the relevant analysis of the results. In the first place, a section explaining two considered laser configurations will be presented. Then, the chapter will be subdivided into four macro-areas which are presented following the logical scheme pursued during the simulation activity. Firstly, the simulations performed in order to evaluate the role of the field ionisation process in the TNSA driven by compact lasers are presented. Then the simulation campaigns to evaluate the configuration of the optimal target are described and analysed. An analysis of the effect of reduced dimensionality is then shown. Lastly, an analysis of the role of foam nanostructure in particle acceleration is illustrated. Also, some plots which can integrate specific parts of the analysis are shown in appendix (A).

5.1. Compact laser configurations for TNSA

5.1.1. Configuration of the 20 TW laser

The first laser configuration to be analysed is a standard laser with a peak power of 20 TW, an intensity FWHM of 30 fs and a wavelength of 0.8 µm. The focal spot radius is set to 3λ. The laser is then extremely focused. The resulting peak intensity is then around 2.2×10^{20} W/cm^2, bringing to an a_0 around 10. The configuration is thus able to bring electron energies above the relativistic limit mentioned in section (1.2.2). This kind of laser is commercially available and can be hosted in small/medium size laser facilities.

5.1.2. Configuration of the sub-TW laser

A laser having a pulse energy of 4.5 mJ and a wavelength of 0.8 µm was simulated in two possible different conditions. This laser can be found commercially as a table-top system.

In the first case, the pulse was simulated with an intensity FWHM of 40 fs and a focal spot radius of 3.0 µm, which is easily achievable in compact table-top lasers. This configuration leads to a peak intensity of 7.48×10^{17} W/cm^2, which corresponds to an a_0 around 0.6, i.e. in the non-relativistic regime for the electron motion.

In the second case, the pulse was simulated, instead, with an intensity FWHM of 10 fs and a focal spot radius of 2.5 µm, a condition which pushes the laser facility to its actual limits, but however a possible condition [99]. This configuration leads to an intensity of 4.31×10^{18} W/cm^2 corresponding to an a_0 around 1.4. The configuration exceeds then the relativistic limit for the electron motion.

5.2. Effects of ionisation

5.2.1. 2D simulations to evaluate ionisation importance in the 20 TW laser

In order to evaluate the importance of considering the tunnel ionisation process in particle in-cell simulations for the 20 TW laser case, simulations on a 200 nm aluminium substrate case were performed with WarpX. The impact of ionisation was studied only in the bare substrate case because the low-Z near-critical layer of a DLT is expected to be less affected by this process and is rapidly fully ionized at this intensity regime. Three different situations were simulated. the first case considers the solid as a totally neutral material. The second, i.e. the *pre-ionised case*, considers the valence electrons of the metal as plasma-like electrons, modelling them as free electrons tries to emulate the reflective property of the metal. The last considers the substrate as a totally ionised plasma.

A box of $x \times y = 125\lambda \times 70\lambda$ was chosen, and laser propagation was set to be parallel to the x direction. As found in the literature, reflecting boundary conditions for particles were set along the propagation direction of the laser, while periodic ones were set in the other direction. Concerning the electromagnetic field, periodic boundary conditions were again set in the y direction, while pml ones were in the other direction. The target was positioned at two times the distance travelled by the laser in its field FWHM, to ensure that the laser pulse has completely entered the box before the interaction starts. The simulation duration was set to 500 fs, i.e. one and a half times the time needed for a light pulse to travel along the simulation box.

The aluminium substrate was, in all three cases, simulated with an ion density of $34.6 n_c$. Thus, in order to resolve at least three times the skin depth of impinging laser wave

and avoid numerical heating, the resolution had to be set to 65 points per micron. The number of macroions per cell used to sample the ions was 10 in the cases taking into account the ionisation process, while 3 in the fully ionised case. The choice of the number of macroparticles per cell was done taking into account that when the ionisation process is accounted for, an ion can generate an unknown number of electrons number due to the ionisation process. Therefore, a higher number of macroions is needed to sample properly also the electrons. Concerning, instead, the electron density in the fully ionised case, a density thirteen times the ion number density was chosen for the electrons and it was sampled with 30 macroelectrons per cell. Also, since the considered material is an aluminium foil, the valence electrons to be accounted for in the pre-ionised case are three. They were sampled with the same number of particles per cell used in the totally ionised case and the resulting electron density is three times the ion number density.

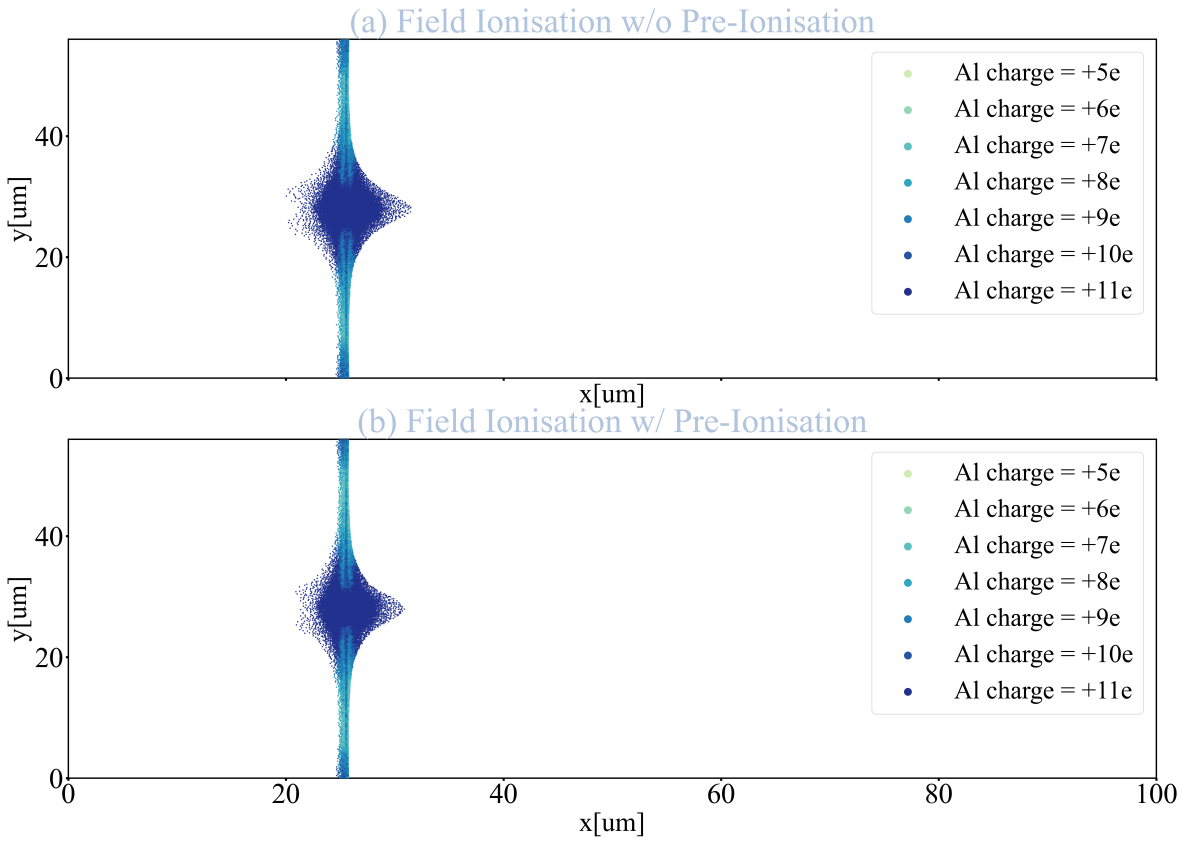

Figure 5.1: Ionisation maps of the aluminium substrate ions extracted at 500 fs after the start of the simulation. The map was generated by plotting all the macroparticles in the simulation colouring them according to their ionisation state. The darker colours show the highest ionisation levels. In (a) the case in which the aluminium target was initialised as completely neutral is shown. In (b) the case in which the aluminium target was initialised as a three times ionised plasma is shown.

In figure (5.1) it is possible to observe a map of the ionisation states in the aluminium substrate: figure (5.1)-(a) shows the ionisation map for of the target simulated as neutral, figure (5.1)-(b) the one of the pre-ionised case. One can see that the ionisation level never reaches its maximum value, i.e. thirteen, neither in the pre-ionised case nor in the neutral case. However, the substrate is always ionised more than three times and, as expected, the aluminium atoms in the laser channel are the most ionised. Indeed, their ionisation level reaches eleven. In this context, it is possible to state that the neglection of the ionisation process, particularly in the presence of a near-critical layer, does not influence in a too-significant way the results of the simulations. The near-critical layer, in fact, reduces the relevance of the substrate in the interaction process.

Figure (5.2) shows the proton spectra obtained for the totally ionised case, the pre-ionised case and the neutral case. It is possible to observe that both the cases accounting for ionisation show a non-negligible increase in proton maximum energy and spectrum slope. Also, the maximum energy reached by the pre-ionised case is lower than the neutral one.

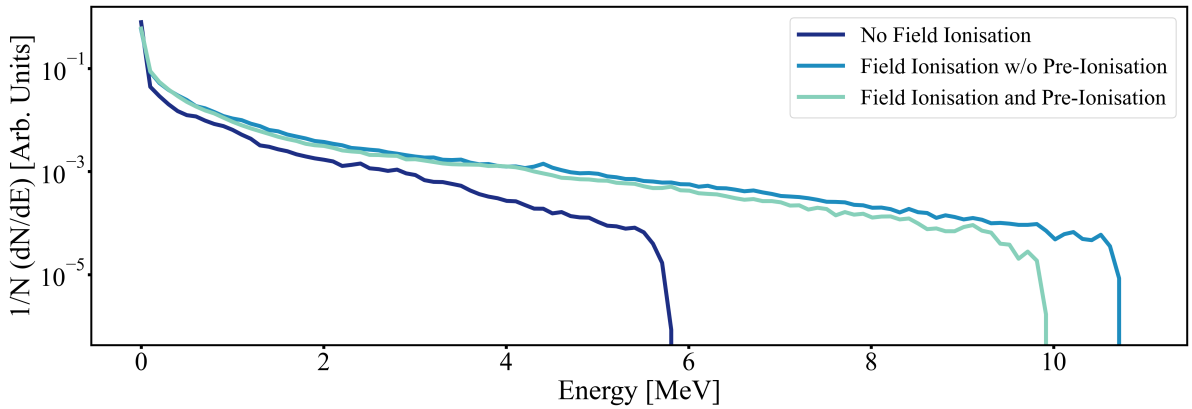

Figure 5.2: Plot of the proton spectra from the plain aluminium substrate retrieved at the end of the simulation in the three different simulation conditions: the darker colour is the spectrum from the totally ionised case, the lighter colours represent in decreasing darkness respectively the spectrum from the neutral case and the pre-ionised case. The terms totally ionised, neutral and pre-ionised refer to the initialisation of the aluminium ion species.

5.2.2. 2D simulations to evaluate tunnel ionisation in the sub-TW laser

To evaluate the importance of the tunnel ionisation process in the interaction of a sub-TW laser with a target, several two-dimensional simulations were performed using WarpX

code. Being lower the laser intensity, this time the complete DLT case is considered since partial ionization of the foam layer could be relevant. The box and resolution choices were the same as in section (5.2.1).

The simulated targets were double-layer targets with a hydrogen contaminant layer on the rear surface. The target start was always positioned at two times the distance travelled by the laser in its field FWHM in the longer pulse laser. It was chosen to position it in a different place in the other case. Due to the shorter pulse duration, the choice was to position the front face of the substrate at 28 µm from the left side of the box. This choice was made to guarantee that the front expansion of the electrons remains confined in the box at least in the first moments after the interaction.

The foam was modelled as a totally neutral carbon foam, which in this case was treated as a homogeneous foam. The foam density was simulated in three different density and thickness conditions for each of the laser cases. For both cases, the optimal foam density was calculated using the model in section (1.3.4). The retrieved optimal case was always simulated. The thickness of each foam was computed as the relevant self-focusing length. Thus in the longer pulse case, the simulated foams were: a 0.3 n_c density foam which was 5.7 µm thick. This foam was computed to be optimal for the case; a 0.95 n_c density foam which was 3.2 µm thick, i.e. the foam having the minimum experimentally achievable density; a 3 n_c density foam which was 1.8 µm thick. It is important to note that, when considering foams, all the densities are expressed as the electron density that the foam would have if it was completely ionised. Concerning the shorter pulse case, the following foams were considered: a 0.2 n_c density foam which was 6.0 µm thick. This foam was computed to be optimal for the case; a 0.95 n_c density foam which was 3.0 µm thick, again, the foam having the minimum experimentally achievable density; a 3 n_c density foam which was 1.7 µm thick.

The substrate was in all cases modelled as 1.0µm thick aluminium foil, having an ion number density of 34.6 n_c. The aluminium was three times pre-ionised to account for the free electrons in the valence band of the metal.

The hydrogen contaminant layer was instead simulated as a totally ionised 0.05 µm thick layer with an ion number density of $10n_c$. The choice of ionising the contaminants was made to be coherent with the pre-ionisation of the valence electrons in the substrate.

The foam ion population was sampled with 4 macroions per cell, the substrate ion population with 5 macroions per cell and the contaminant layer with 100 macroions per cell to have a good statistics. The substrate electron population was sampled with 30 macroelectrons per cell and the contaminant electron population with 100 macroelectrons per

cell.

Foam density	Z^{*-max}_{foam} [-]	$\bar{Z}^{*}_{foam}$ [-]	Z^{*-max}_{subs} [-]	$\bar{Z}^{*}_{subs}$ [-]
	Laser FWMH = 40 fs			
0.30 n_c	6	2.712	5	3.000
0.95 n_c	6	2.760	6	3.001
3.0 n_c	5	0.983	3	3.000
	Laser FWMH = 10 fs			
0.20 n_c	6	2.654	7	3.016
0.95 n_c	6	4.060	6	3.007
3.0 n_c	6	1.702	4	3.000

Table 5.1: Summary of the maximum and average state of ionisation of the species in the simulations of the sub-TW laser. The first row of the table summarises the results obtained when the intensity FWHM of the laser is equal to 40 fs and the second the results obtained when the intensity FWHM of the laser is equal to 10 fs. The first two columns regard respectively the maximum and mean foam ionisation state, the last two the maximum and mean substrate ionisation state

In table (5.1) the summary of the maximum and average ionisation states retrieved at the end of the simulation in the various cases is presented. It is promptly possible to observe that great differences arise when considering both different laser and foam configurations. Concerning foam ionisation, one can first note that almost in all cases, the carbon atoms reach the maximum state of ionisation. The only case when carbon never completely ionises is the overdense case in the non-relativistic limit for the electron motion.

The mean ionisation state of the foam greatly differs among the cases. It can be noted that the latter is generally higher in the relativistic case (10 fs laser). However, the lowest-density cases show a lower mean ionisation level when comparing the relativistic case with the non-relativistic relevant one (40 fs laser). It can also be observed that the highest mean ionisation level is always reached in the 0.95 n_c case, meaning a higher number of electrons is generated in the foam.

When considering instead the substrate ionisation, it is possible to see that the substrate mean ionisation level remains almost constant in all cases setting around three, i.e. almost only the pre-ionised electrons are present at the end of the simulation. However, it is possible to note that the maximum ionisation state reaches values way higher than the mean one. The highest values for the ionisation are always reached in the relativistic case with a maximum in the lowest-density case. However, the aluminium is never totally ionised.

In figure (5.3) the ionisation maps of the foams in the non-relativistic laser case are presented. In figure (5.3)-(a) the ionisation map of the lowest density foam is shown, in figure (5.3)-(b) the one of the 0.95 n_c foam and in figure (5.3)-(c) the one of the overdense foam.

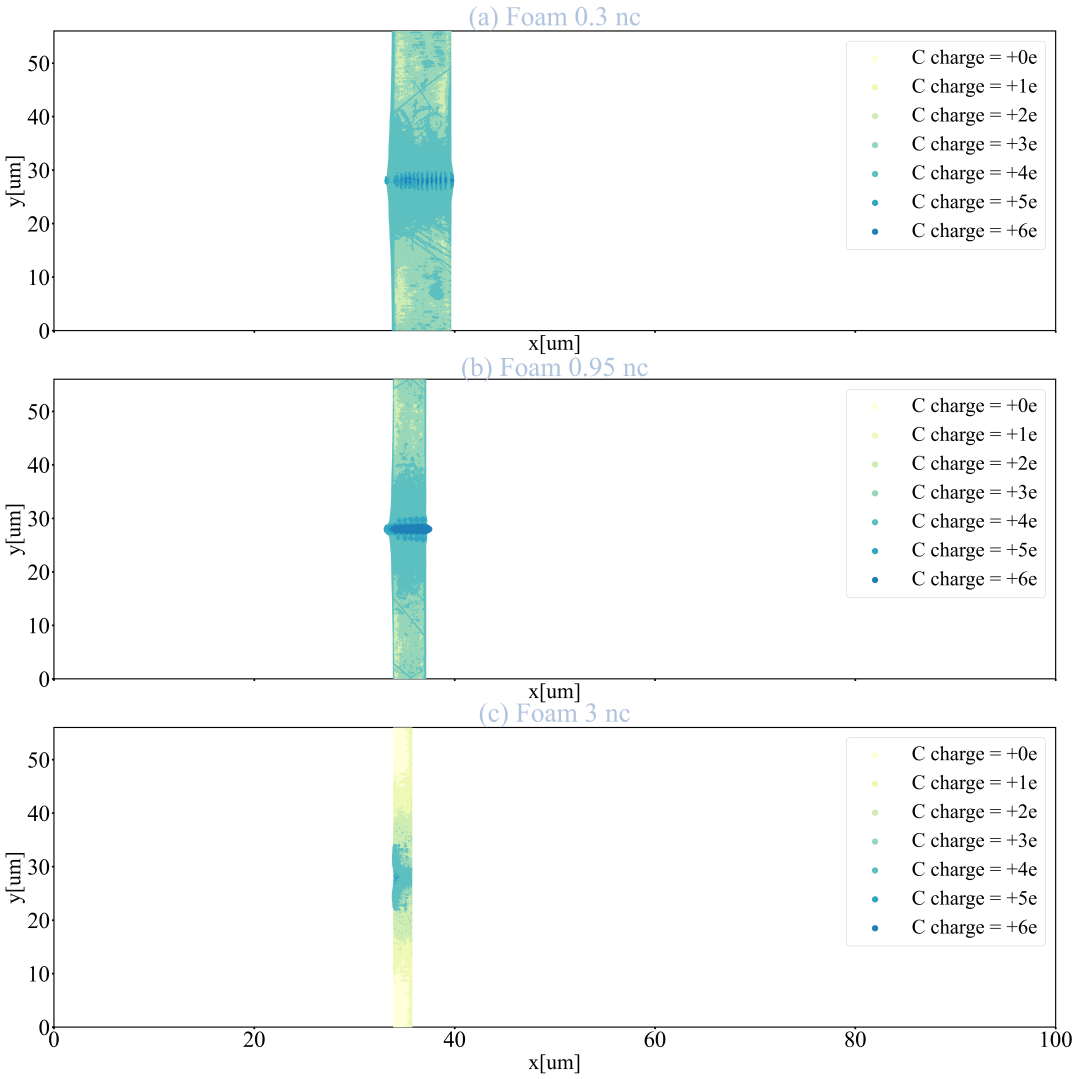

Figure 5.3: Foam ionisation maps at 500 fs for the 40 fs FWHM laser. The map was generated by plotting all the macroparticles in the simulation colouring them according to their ionisation state. In (a) the 0.30 n_c foam is shown, in (b) the 0.95 n_c foam and in (c) the 3.0 n_c foam. The darker colour is related to a higher ionisation level.

As shown also from the results in table (5.1), the densest foam does not get ionised as much as the others. It is possible to observe that the highest ionisation level is reached at the front part of the foam. However, the ionisation front does not propagate up to the rear face of the foam, meaning the field is not high enough to ionise completely the atoms

in the laser channel. In both underdense foams, instead, the laser channel gets completely ionised. The 0.95 n_c foam presents a uniform ionisation state in the channel, while in the 0.3 n_c periodic peaks of ionisation are observed. Taking into consideration the portions of foam farther from the laser channel, one can observe that a high grade of ionisation is reached in underdense foams, while few ionisation events are shown in the overdense foam.

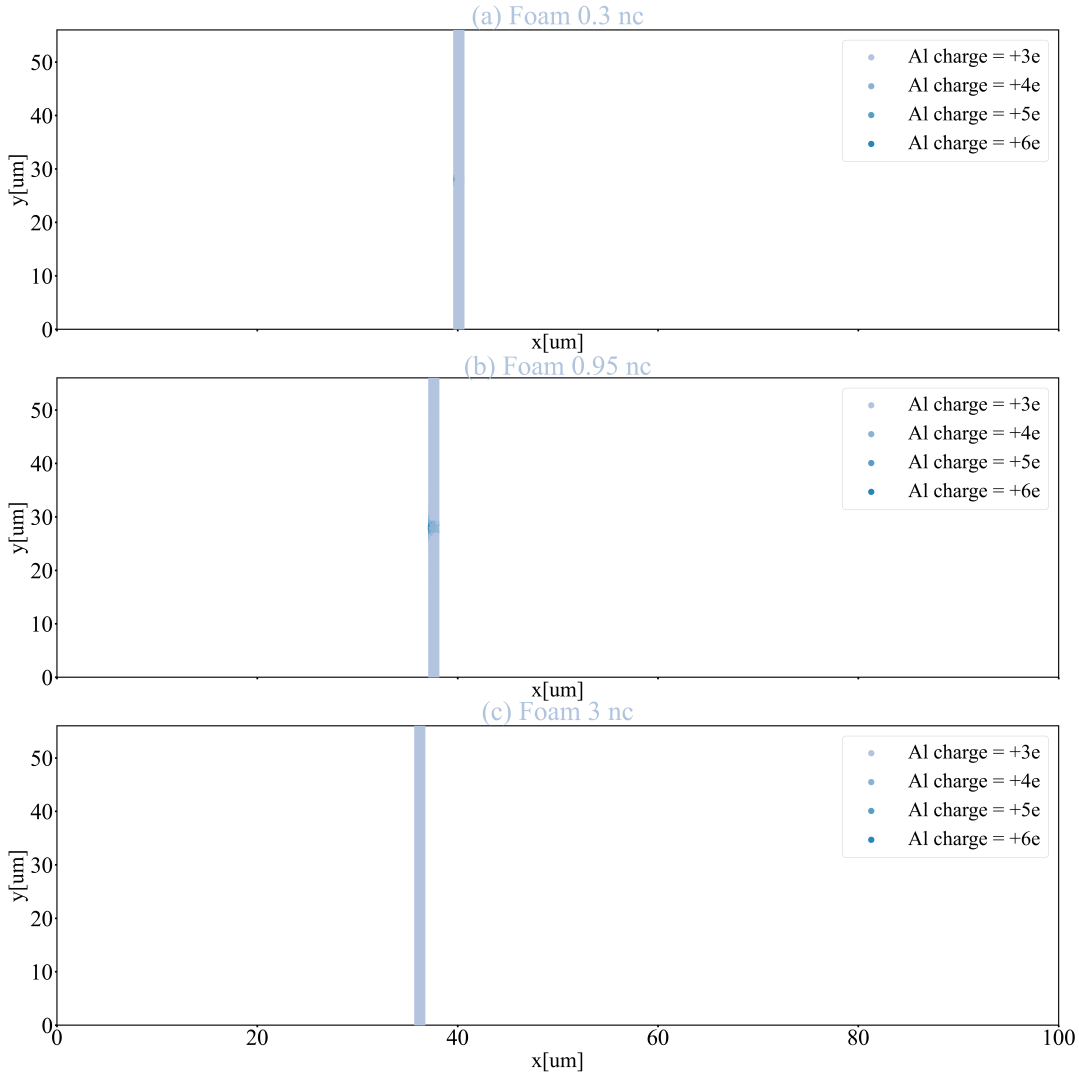

Figure 5.4: Substrate ionisation maps at 500 fs for the 40 fs FWMH laser. The map was generated by plotting all the macroparticles in the simulation colouring them according to their ionisation state. In (a) the substrate in the 0.30 n_c foam case is shown, in (b) the one in the 0.95 n_c foam case and in (c) the one in the 3.0 n_c foam case. The darker colour is related to a higher ionisation level.

In figure (5.4) the ionisation maps of the substrates in the non-relativistic laser case are

presented. In figure (5.4)-(a) the ionisation map of the substrate in the lowest density foam case is shown, in figure (5.4)-(b) the one in the 0.95 n_c foam case and in figure (5.4)-(c) the one in the overdense foam case. By observing the ionisation map, one can readily notice that almost all the substrate remains at its ground ionisation state. No ionisation events happen in the substrate when the foam density is 3 n_c. Instead, in the other two cases, an increase in the ionisation level is noticed. The ionised particles are concentrated on the front side of the substrate where the electromagnetic field is higher and their position is located along the laser channel. The 0.95 n_c case presents the highest grade of ionisation meaning a stronger electric field reaches the rear surface.

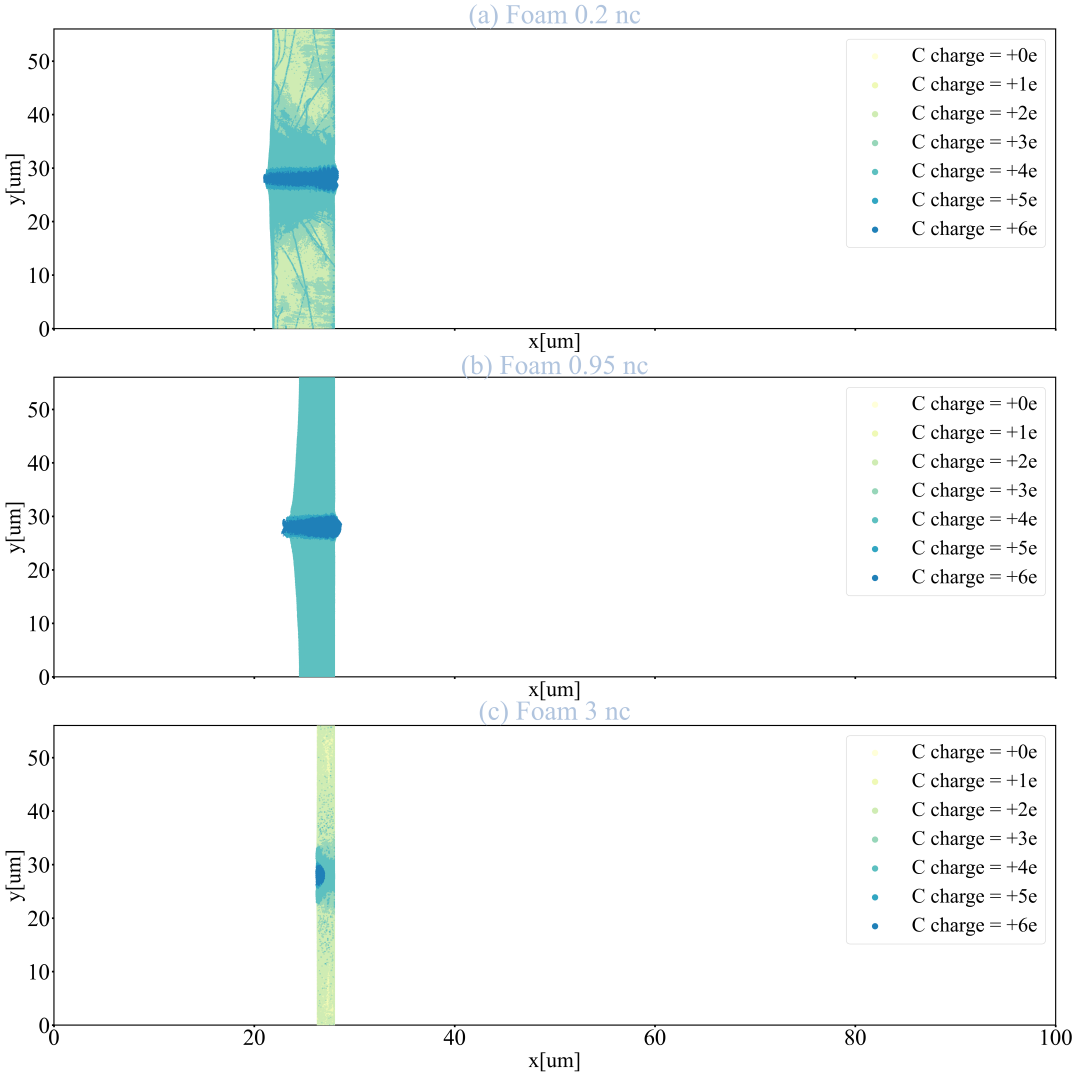

Figure 5.5: Foam ionisation maps at 500 fs for the 10 fs FWMH laser. The map was generated by plotting all the macroparticles in the simulation colouring them according to their ionisation state. In (a) the 0.20 n_c foam is shown, in (b) the 0.95 n_c foam and in (c) the 3.0 n_c foam. The darker colour is related to a higher ionisation level.

In figure (5.5) the ionisation maps of the foams in the relativistic laser case are presented. In figure (5.5)-(a) the ionisation map of the lowest density foam is shown, in figure (5.5)-(b) the one of the 0.95 n_c foam and in figure (5.5)-(c) the one of the overdense foam. By looking at the maps, it is readily possible to notice a great difference with respect to the non-relativistic case. In all cases, the overall ionisation level is higher. The laser channel becomes visible and completely ionises when the density is below the critical value. In the overdense case, instead, it does not completely ionise showing again the lack of propagation of the ionising front across the substrate. The ionisation level far from the channel reaches its highest level in the 0.95 n_c case; the foam in the 0.2 n_c case gets almost completely ionised.

In figure (5.6) the ionisation maps of the substrates in the 10 fs FWHM laser case are presented. In figure (5.6)-(a) the ionisation map of the substrate in the lowest density foam case is shown, in figure (5.6)-(b) the one in the 0.95 n_c foam case and in figure (5.6)-(c) the one in the overdense foam case.

As it happens in the non-relativistic case, the substrate does not ionise as much as the foam, particularly when considering the particles which are located far from the laser spot. It is possible, however, to notice an overall higher grade of ionisation in the substrate when comparing the results with the longer pulse ones. Some ionisation events of the substrate ions occur also in the overdense foam case. Moreover, both the lower-density cases present a partially ionised laser channel in the substrate.

Summing up all the considerations, it is possible to state that generally, when considering cases with low laser intensity, the ionisation process seems to play an important role in the acceleration process. The target, in fact, does not always ionise at such a level to be allowed to neglect the field ionisation process in the modelling and it is unlikely that a strong ionisation could be caused by a prepulse.

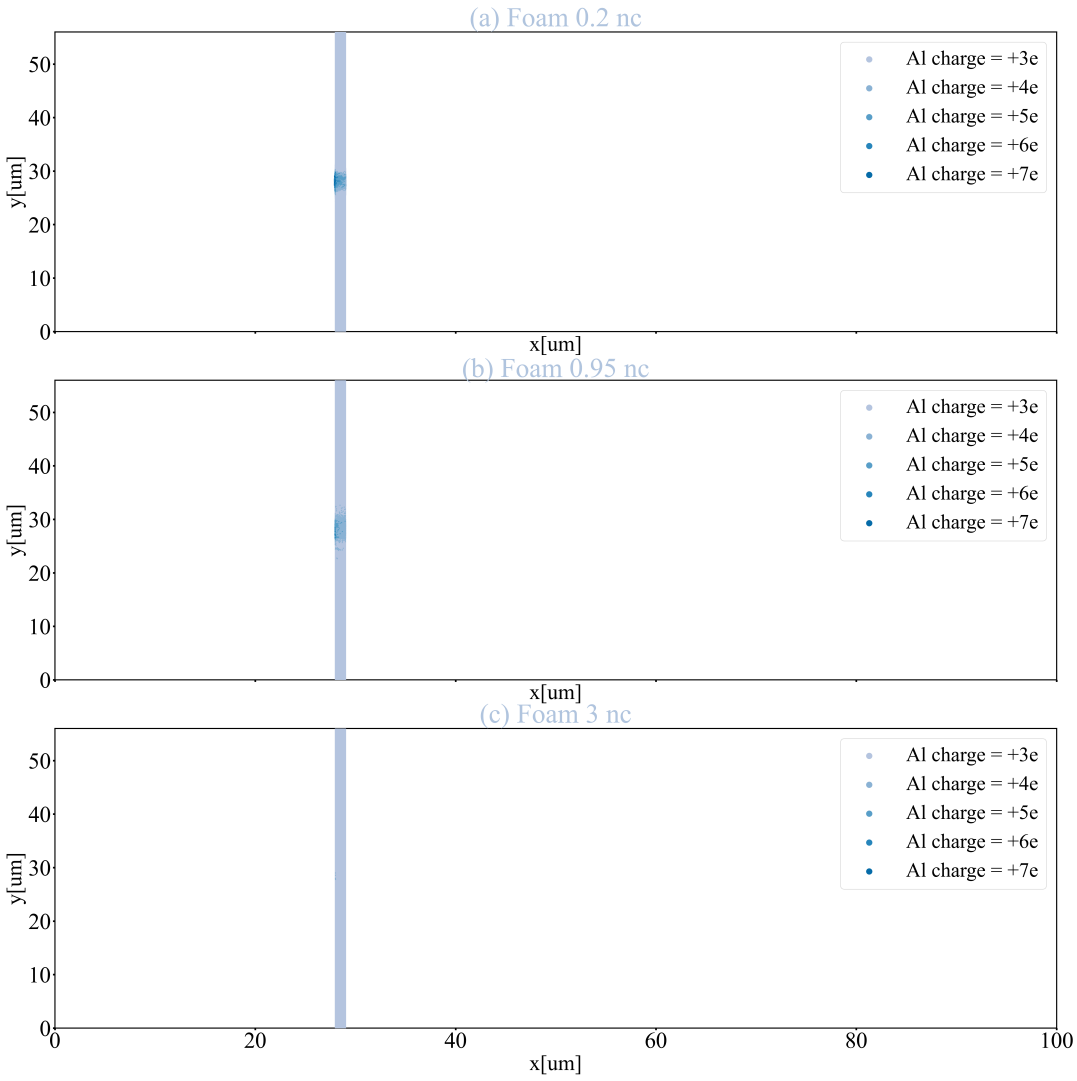

Figure 5.6: Substrate ionisation maps at 500 fs for the 10 fs FWMH laser. The map was generated by plotting all the macroparticles in the simulation colouring them according to their ionisation state. In (a) the substrate in the 0.20 n_c foam case is shown, in (b) the one in the 0.95 n_c foam case and in (c) the one in the 3.0 n_c foam case. The darker colour is related to a higher ionisation level.

In order to evaluate even the possible differences between the ionisation modules in WarpX and Smilei, a simulation for the 0.95 n_c case only was performed in Smilei. The simulation had the same input parameters which were used in the corresponding WarpX simulation. In the table (5.2) a summary of the results is shown.

No substantial differences are visible either in the results in the table or in ionisation maps which are not reported in this chapter. One can, thus, confirm what has been found checking the WarpX and Smilei codes: the implementation of the ionisation process in

Foam density	Z^{*-max}_{foam} [-]	$\bar{Z}^{*}_{foam}$ [-]	Z^{*-max}_{subs} [-]	$\bar{Z}^{*}_{subs}$ [-]
	Laser FWMH = 10 fs			
0.95 n_c	6	3.948	6	3.049

Table 5.2: Summary of the state of ionisation of the species in the simulation performed with Smilei. The first two columns regard respectively the maximum and mean foam ionisation state, the last two the maximum and mean substrate ionisation state.

the two tools is equivalent. This result is coherent with the fact that the implementation of the ionisation process in the two codes is based on the same model.

5.3. Two-dimensional parametric scans to evaluate the optimal condition

5.3.1. Set-up and analysis of simulations of the 20 TW laser

In order to prove the feasibility of using laser-DLT coupling as a proton source to perform material analyses, a parametric scan is needed to evaluate which are the optimal target conditions which improve the average and maximum energy of protons and the conversion efficiency from laser to proton kinetic energy. Indeed, these quantities are the most relevant in some applications of laser-driven protons like PIXE. To do so, two-dimensional simulations are needed, in order to avoid the too-high computational cost which would arise by using full-dimensional simulations. WarpX code was chosen due to the possibility of accelerating simulations with GPUs. This can greatly reduce the computational cost of the parametric scan.

Same conditions as in section (5.2.1) concerning the resolution, the simulation box dimensions, the boundary conditions and the simulation time were chosen. Three different completely ionised aluminium substrates were simulated with an ion density of 34.6 n_c. Three different substrate thicknesses were simulated: 200 nm, 600 nm and 2 µm. The foam was, then, modelled as a completely ionised homogeneous carbon foam, with an electron density of 2.6 n_c. This density was established as a result of the optimal parameters calculated using equation (1.38). Also, the optimal length of the foam was computed following equation (1.37) and resulted in a thickness of nearly 4 µm. In order to compare different cases, the foam thickness was varied, setting it to half and double the optimal one. A plain substrate too was then simulated, to analyse the gain retrieved from the with the addition of a near-critical layer. A 0.05 µm ionised hydrogen contaminant layer was then added to the bottom of the substrate to simulate the hydro-contaminants on the

metal surface. Its density was set to 10 n_c. The contaminant layer is the source of protons on which TNSA is most effective. To simulate realistically the situation, a good statistic for the simulated particles is needed. Thus, 30 macroelectrons per cell were simulated for the substrate, 10 for the foam and 100 for the contaminant layer. 3 macroions per cell for the substrate, 1 for the foam and 100 for the contaminant layer. The choice of simulating a high number of contaminant ions was done to have a better statistics on protons, which are the main focus of the analysis. For each substrate case, all the three different foams and the bare substrate were simulated.

The results of the simulations are summarised in table (5.3).

Foam thickness	E_p^{max} **(MeV)**	$\bar{E}_p$ **[MeV]**	T_p **[MeV]**	**Efficiency** η **[-]**
	Substrate Thickness = 0.2 µm			
No foam	5.86	1.32	1.09	0.52%
2 µm	26.24	3.44	5.03	5.48%
4 µm	31.05	4.2	6.04	8.31%
8 µm	22.83	3.88	4.07	7.28%
	Substrate Thickness = 0.6 µm			
No foam	4.56	1.26	1.03	0.25%
2 µm	21.63	3.55	5.54	3.64%
4 µm	24.04	4.41	5.91	5.72%
8 µm	18.73	3.93	4.16	5.33%
	Substrate Thickness = 2 µm			
No foam	2.69	0.91	0.61	0.07%
2 µm	17.93	3.27	4.13	2.61%
4 µm	19.03	4.02	5.24	4.58%
8 µm	15.92	3.60	3.62	4.50%

Table 5.3: Summary of the results for proton acceleration retrieved with the method based on the model in section (2.2.1). The different rows of the table divide the results into the three different aluminium substrate thicknesses. For the four cases of foam thickness, the columns show in order the proton maximum energy, the mean proton energy, the temperature associated with the proton spectrum and the laser energy conversion efficiency into kinetic energy of the protons.

Before starting with the analysis of the result, it is important to focus on the methodology used to extract the proton spectra, energies and temperature shown in this table. The model shown in section (2.2.1) is firstly used to extract the estimated maximum energy

of the plain substrate and, as a consequence, the simulation time at which extracting the associated proton energy spectrum. Due to the presence of the foam, however, different behaviour of the maximum proton energy during the simulation time is observed. Thus, the model is no more applicable. In order to be coherent with the model, we computed the time difference between the first energy increase of the proton population and the time at which the maximum energy predicted by the aforementioned model was reached. It was then assumed that this time difference is constant even in the presence of foams. This assumption is justified by the fact that the characteristic time of the interaction between the protons and the sheath-like field produced by the electrons can be considered approximately constant for the maximum energy protons. The proton spectra of the double-layer targets are then taken at this same time difference after the first energy increase of each case. The temperature is estimated using an exponential fitting on the central part of the spectra, in order to avoid the influence of the spectrum tails.

As one can observe from the results, in all cases the optimal condition resulting from the simulations (the 4 µm case) confirms the prediction of the model proposed in section (1.3.4). Also, as expected, a great gain in proton energy is always achieved in double-layer targets thanks to the nearcritical layer. Also, the thickness of the substrate seems to play an important role in proton acceleration: higher proton energies are always reached with decreasing substrate thickness.

In figure (5.7) the time behaviour of the total field energy is shown.

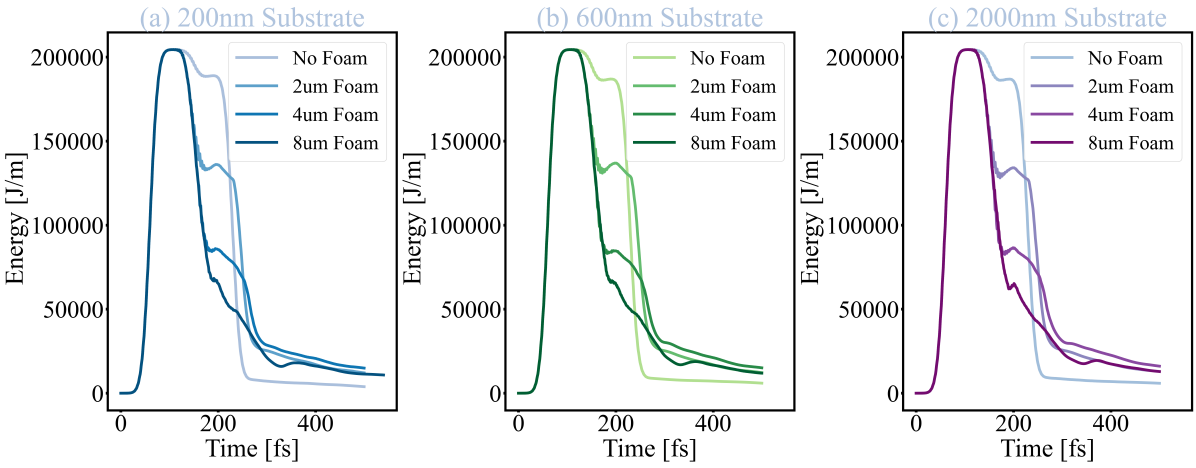

Figure 5.7: Plot of the total energy associated with the electromagnetic field evolution in time. In (a) the results from the 200 nm substrate are presented, in (b) the ones from the 600 nm substrate and in (c) the ones from the 2000 nm substrate. In all cases, the darker colours are associated with an increase in foam thickness.

It is possible to notice that the differences in substrate thickness do not influence in a visible way the time evolution of the energy associated with the electromagnetic field.

On the contrary, the presence of the foam and its thickness seems to have a strong impact on the results. A higher decrease of the field energy is shown in fact with an increasing foam thickness. After the first absorption of the field energy happening at the time of interaction between the laser pulse and the target, it is, then, possible to notice that the energy falls down again due to the pml boundary conditions. However, the remaining field energy after the reflected pulse has exited the simulation box seems to be related to the thickness of the near-critical layer. When no foam is present, the remaining electromagnetic field energy approaches rapidly zero, while this effect is reduced in the presence of foams.

One can also notice that the highest field energy at the final time-steps is associated with the optimal foam in all the cases, while the thinnest and the thickest foam cases show lower field energy. This behaviour seems to be related to the behaviour of the maximum proton energy shown in the table above: the higher the field energy remaining after the field exited the box, the higher the maximum proton energy retrieved from the simulation.

In figure (5.9) the total kinetic energy of the electrons is shown for all the cases.

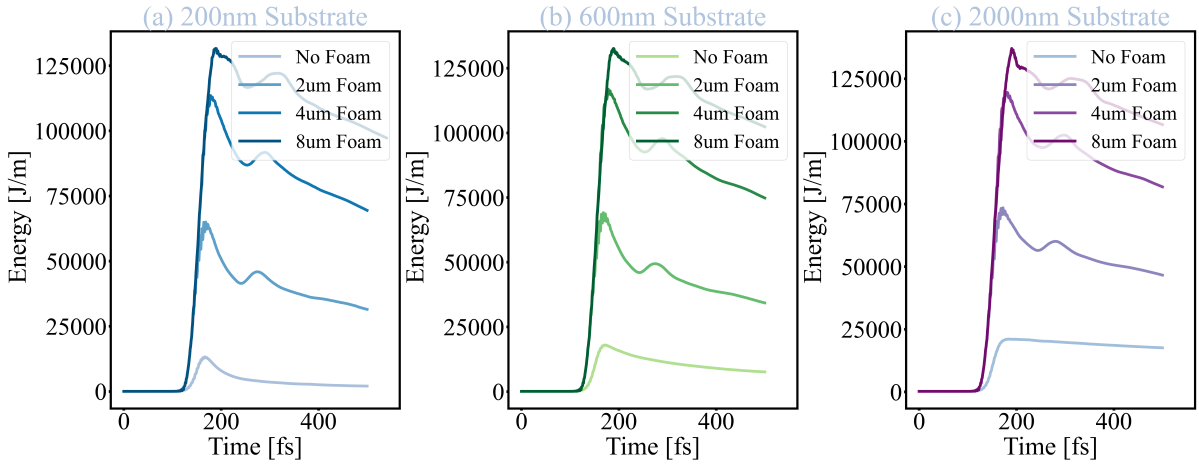

Figure 5.8: Plot of the total kinetic energy of the electron evolution in time. In (a) the results from the 200 nm substrate are presented, in (b) the ones from the 600 nm substrate and in (c) the ones from the 2000 nm substrate. In all cases, the darker colours are associated with an increase in foam thickness.

It is possible to note that the highest electron energy is related to the maximum absorption of the field. Two peaks in the electron energy are present. The first is happening at

the moment of the first interaction between the laser pulse and the target. The second one is visible only when a foam is present. It is related to a further decrease in the electromagnetic field energy due to the interaction with the metallic substrate.

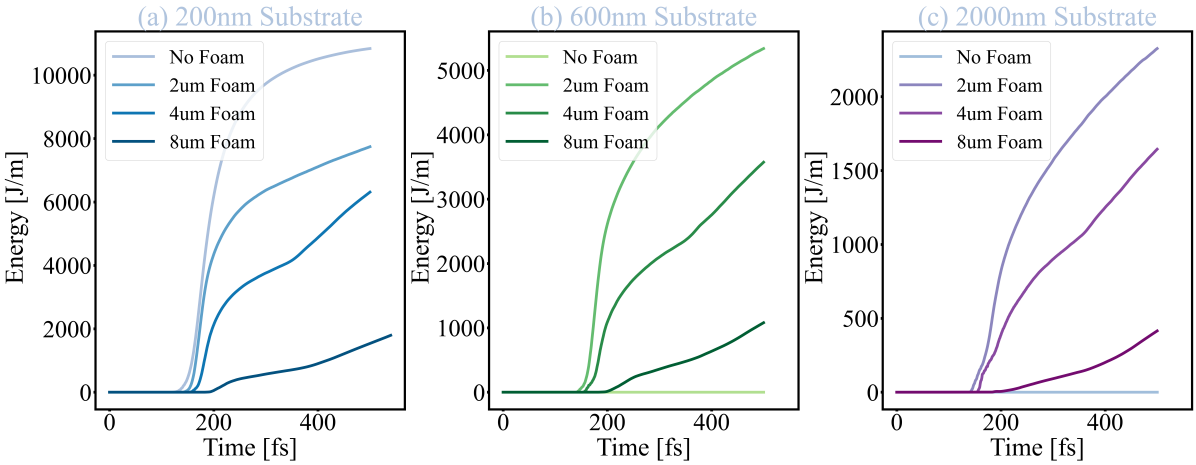

Figure 5.9: Plot of the total kinetic energy of the ions of the substrate evolution in time. In (a) the results from the 200 nm substrate are presented, in (b) the ones from the 600 nm substrate and in (c) the ones from the 2000 nm substrate. In all cases, the darker colours are associated with an increase in foam thickness.

In figure (5.9) the total kinetic energy of the ions of the substrate is shown for all the cases. It is possible to observe that, when a near-critical layer is present, the substrate ions in most cases absorb more energy. Also, a decreasing trend in their energy with foam thickness is always shown. A greatly different behaviour is shown in the case of the 200 nm thick single-layer targets. While the thickest targets show almost no increase in energy during the simulation time, the 200 nm target exhibits a completely opposite tendency. It is in fact the condition showing the maximum energy absorbed by the substrate ions.

Figure (5.10) shows, instead, the proton spectra obtained with the method based on the model in section (2.2.1). In figure (5.10)-(a) spectra from the substrate 200 nm thick are shown, in figure (5.10)-(b) the ones from the 600 nm substrate and in figure (5.10)-(c) the ones from the 2000 nm substrate. Important differences are noticeable between the cases with the foam and the plain target. Both the spectrum slopes and the maximum energies plain targets result lower than the double-layer target ones. This is directly related to the results on the temperature shown in table (5.3): the slope of the spectra is in fact directly related to the temperature when the spectra can be approximated by exponential distributions.

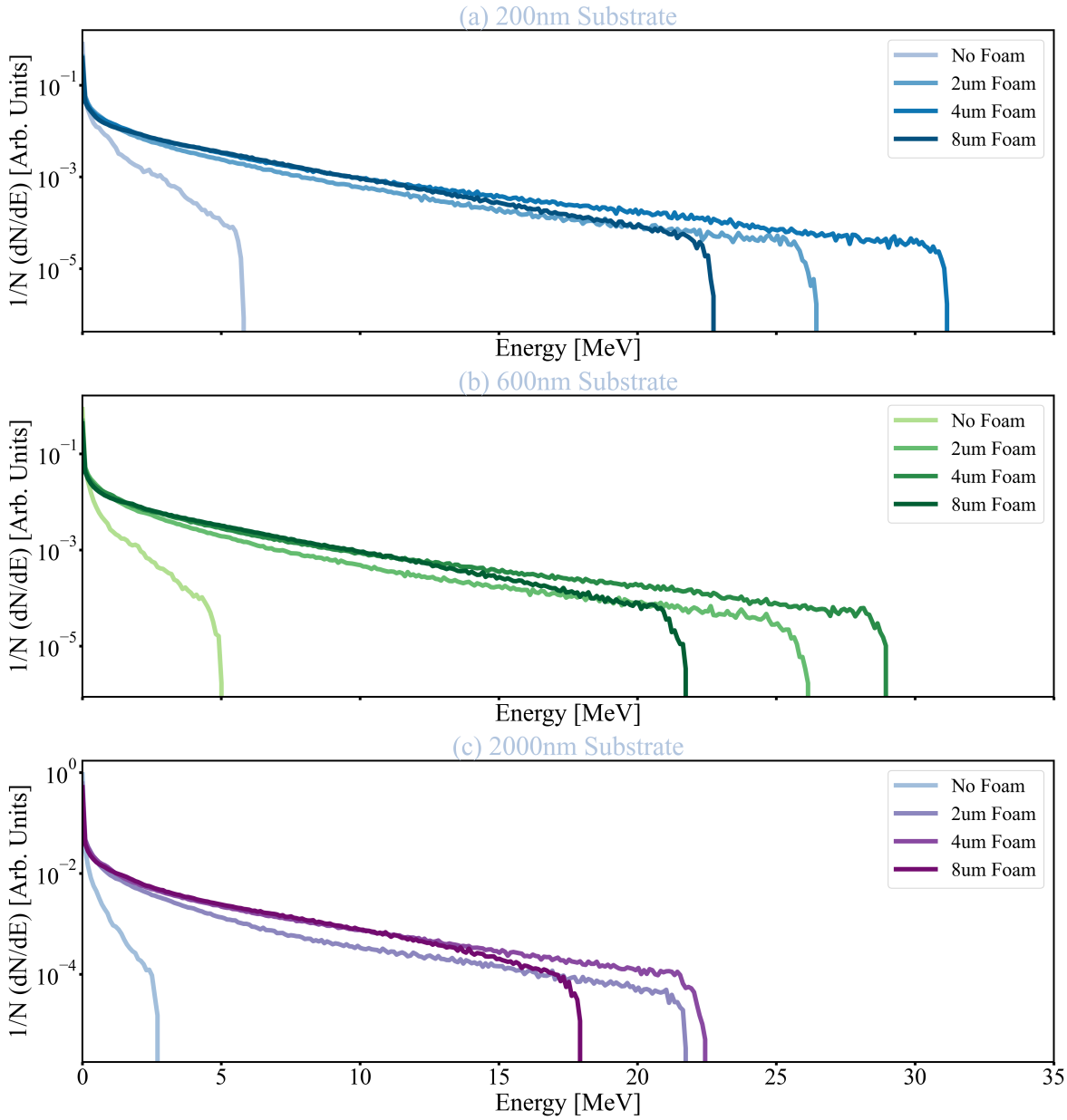

Figure 5.10: Plot of the proton spectra. In (a) the results from the 200 nm substrate are presented, in (b) the ones from the 600 nm substrate and in (c) the ones from the 2000 nm substrate. In all cases, the darker colour is associated with an increase in foam thickness.

In figure (5.11) the electron density maps retrieved from the simulation with the thinnest substrate are shown. It is possible to observe the self-focusing effect happening in the near-critical layer which is enhanced when the thickness is optimal. Also, by looking at figure (5.11)-(a) it is possible to observe that part of the laser electromagnetic field passed through the aluminium substrate, an effect due to the reduced substrate thickness of the

case shown in the figure.

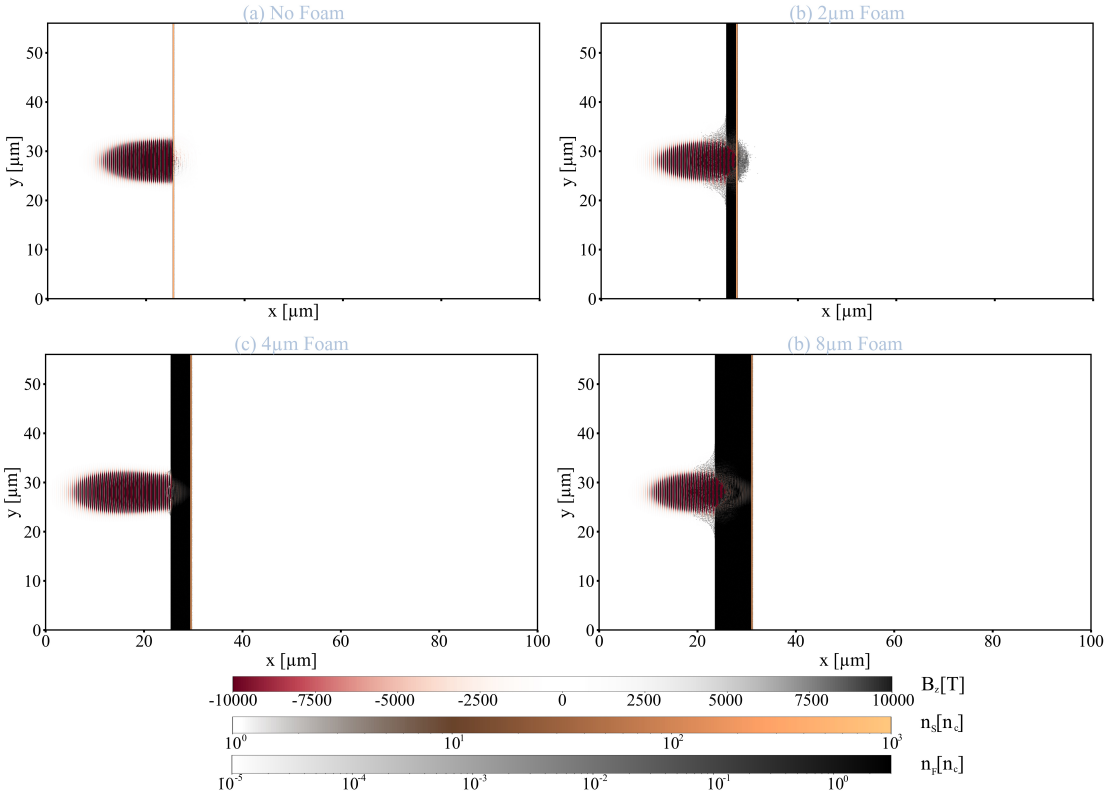

Figure 5.11: Maps of the electron density and the magnetic field B_z retrieved at the moment of the interaction between the laser and the targets. The shown cases are the ones relative to the thinnest substrate (200 nm). In (a) the single-layer target is shown, in (b) the DLT with the 2 µm foam, in (c) the DLT with the 4 µm foam and in (d) the DLT with the 8 µm foam.

5.3.2. Set-up and analysis of simulations of the sub-TW laser

In order to evaluate the optimal target, the same simulations shown in section (5.2.2), set for the analysis of the ionisation effects, were used. Thus the analysis, in this case, is restricted to the research of the optimal laser configuration and the optimal foam conditions for proton and ion acceleration. No analysis of the substrate thickness effects in proton accelerations was performed in this case. In table (5.4) the most significant values for proton acceleration retrieved 200 fs after the first interaction with the substrate, are shown.

By observing the obtained results, one can readily observe a great reduction of the overall proton energy with respect to the values presented in section (5.3.1). The first result to capture the attention is surely the one of the overdense foam: while in the 20-TW case, a

Foam thickness	E_p^{max} [keV]	$\bar{E}_p$ [keV]	T_p [keV]	Efficiency η [-]
	Laser FWMH = 40 fs			
0.30 n_c	355.35	62.26	106.39	0.41%
0.95 n_c	145.15	31.35	26.49	0.14%
3 n_c	5.65	0.00	0.00	0.00%
	Laser FWMH = 10 fs			
0.20 n_c	235.24	41.92	58.39	0.13%
0.95 n_c	980.98	105.63	164.68	3.04%
3 n_c	5.45	0.00	0.00	0.00%

Table 5.4: Summary of the results for proton acceleration in the sub-TW laser. The first row of the table summarises the results obtained when the intensity FWHM of the laser is equal to 40 fs and the second the results obtained when the intensity FWHM: of the laser is equal to 10 fs. For the different cases of foam density and thickness, columns shows in order the proton maximum energy, the mean proton energy, the temperature associated with the proton spectrum and the laser energy conversion efficiency into kinetic energy of the protons.

similar foam resulted in the optimal case for proton acceleration, in the sub-TW regime the laser energy is almost not converted into proton kinetic energy. Also, it is possible to notice that in the two different laser configurations the optimal case, i.e. the one which improves the average and maximum energy of protons and the conversion efficiency from laser to proton kinetic energy, changes. When considering the laser configuration with a pulse of 40 fs the optimal case is, in fact, the subcritical case computed by the model for the optimal foam. When considering, instead, the configuration with the laser pulse duration of 10 fs the optimal case is instead the one with the foam the density of which is 0.95 n_c. This latter case is also the optimal configuration retrievable from the sub-TW laser considered. It is in fact the only one able to reach the MeV order of magnitude in proton energy. Also, the efficiency is similar to the ones observed in the 20 TW case.

In figure (5.12) the field energy time behaviour is shown for both the laser configurations.

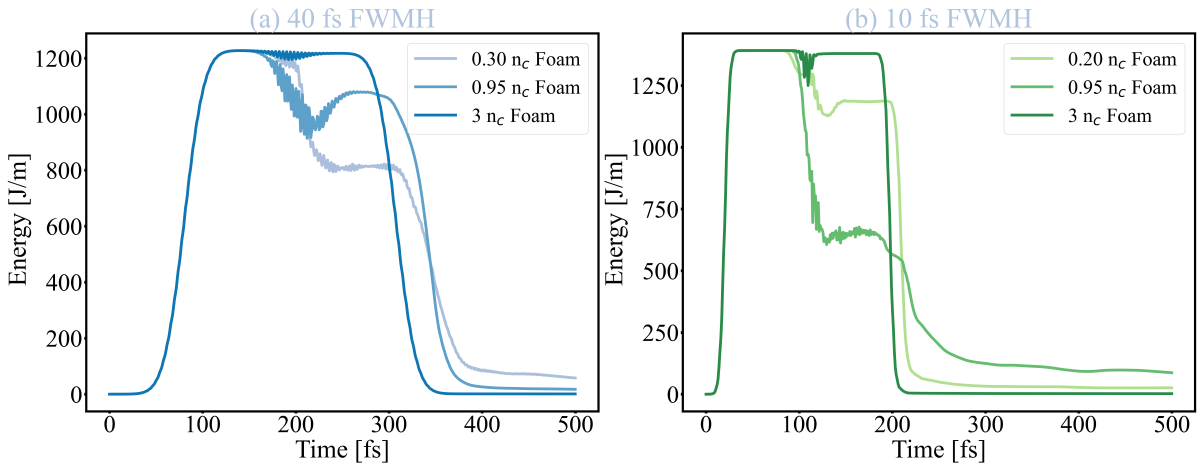

Figure 5.12: Plot of the total energy associated with the electromagnetic field evolution in time. In (a) the results from the laser with 40 fs in intensity FWHM and in (b) the ones from the laser with 10 fs in intensity FWHH. In all cases, the darker colours indicate an increase in foam density.

By the analysis of the plots above, one can immediately notice some important features. Firstly, the behaviour of the field energy when considering the overdense foam in both cases shows almost no absorption. This confirms the results of table (5.4) for the maximum and average proton energy.

Focusing on figure (5.12)-(a) it is possible to observe that the highest absorption of the laser pulse is reached in the sub-critical foam.

Instead when focusing on figure (5.12)-(b) the highest absorption is reached with the 0.95 n_c foam. By comparing the two plots, one can however note two important differences. The first regards the maximum field energy, which is higher in the relativistic case. This effect is caused by two-dimensional effects, which do not take into account the other transversal dimension of the laser spot. The second regards the overall field absorption: it is possible to note that the highest field energy absorption is retrieved in the 0.95 n_c case for the laser having the shorter pulse duration, again confirming the trend seen before in proton energy in table (5.4).

In figure (5.13), the electron energy in time is presented. In figure (5.13)-(a), the results for the laser having the intensity FWHM of 40 fs are presented, while in figure (5.13)-(b) one can find the results for the laser having the intensity FWHM of 10 fs.

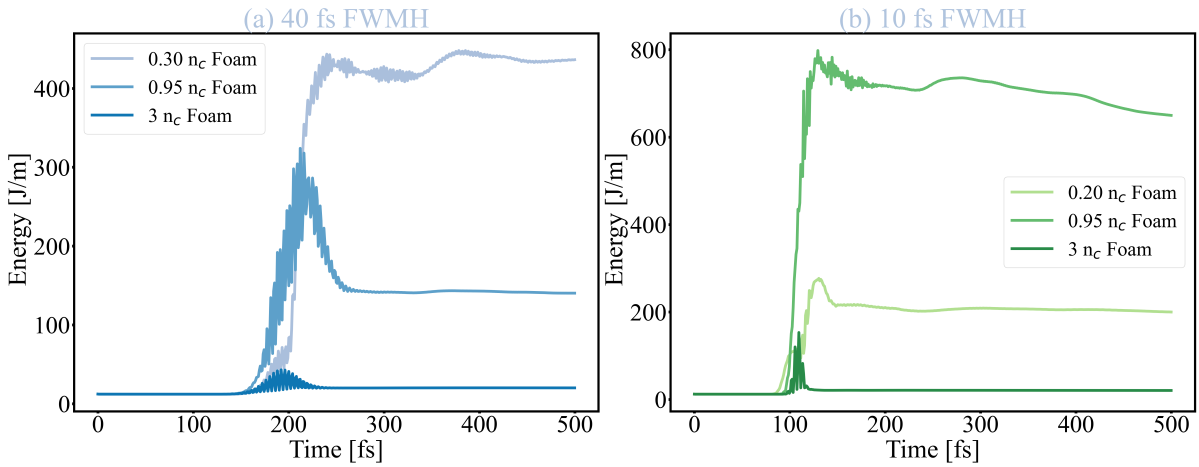

Figure 5.13: Plot of the total electron energy evolution in time. In (a) the results from the laser with 40 fs in intensity FWHM and in (b) the ones from the laser with 10 fs in intensity FWHM. In all cases, the darker colours are associated with an increase in foam density.

The electron energy behaviour is in agreement with the results shown for the electromagnetic field. The electrons are the particles which absorb the greatest part of the field energy. Also, comparing the behaviour with the one shown in figure (5.8) a visible oscillating trend is shown during the electron heating and can be an effect of considering the ionisation. After the first peak, the electron energy seems to remain almost constant during the simulation. An exception can be observed for the optimal case: in fact, the mean energy seems to slightly decrease.

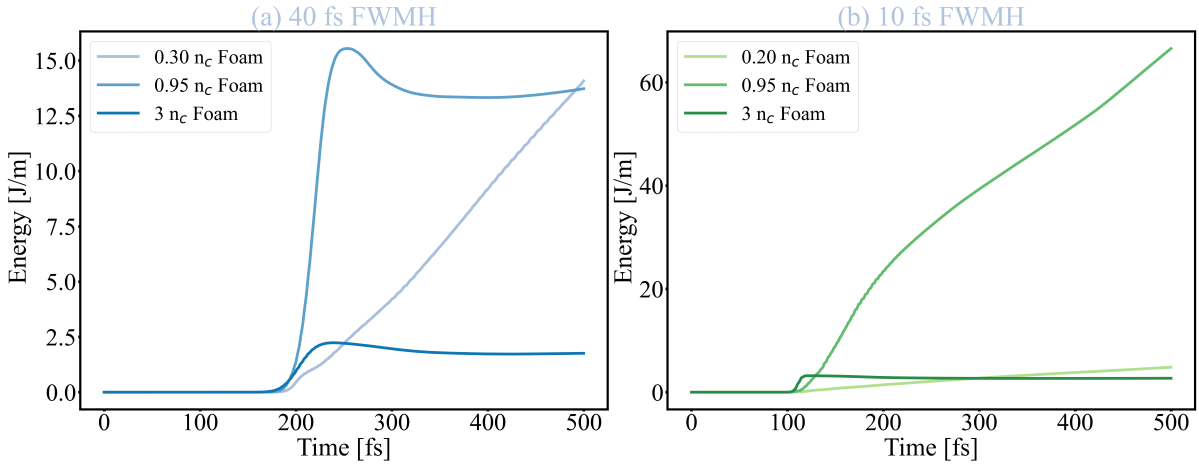

Figure 5.14: Plot of the foam ion energy evolution in time. In (a) the results from the laser with 40 fs in intensity FWHM and in (b) the ones from the laser with 10 fs in intensity FWHM. In all cases, the darker colours are associated with an increase in foam density.

In figure (5.14), the behaviour in time of the foam ion energy is shown. In figure (5.14)-(a) the results for the laser having the intensity FWHM of 40 fs are presented, while in figure (5.14)-(b), one can find the results for the laser having the intensity FWHM of 10 fs. From the plots, it is possible to see great differences in foam ion behaviour among all the cases. When considering the lower-intensity laser one can notice that the increase in energy of the 0.95 n_c case is faster than the other cases. After a reduced time delay, their energy reaches a plateau. A similar condition is shown by the overdense case, even though the energy increase is smaller. The 0.30 n_c case, instead, shows a continuous increase in their energy. When considering the higher-intensity laser, both the lower-density cases show a continuous increase in the ion energy. The maximum is shown by the 0.95 n_c case. The behaviour of the overdense case is, instead, similar to the one retrieved in the other laser condition.

In figure (5.15) the proton spectra retrieved at 250fs after the first interaction with the substrate of the target are shown.

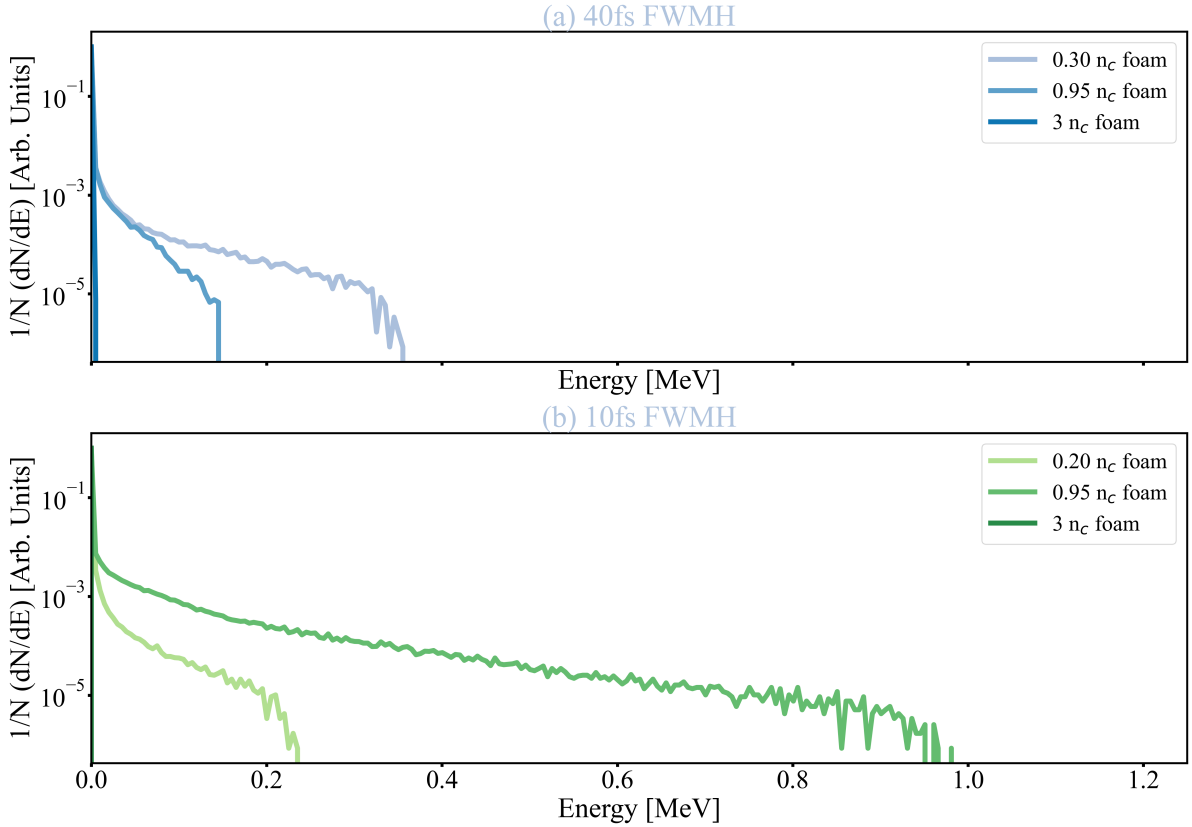

Figure 5.15: Plot of the proton spectra retrieved 250 fs after the first interaction. In (a) the results from the laser with 40 fs in intensity FWHM and in (b) the ones from the laser with 10 fs in intensity FWHM. In all cases, the darker colours are associated with an increase in foam density.

In figure (5.15)-(a), the ones from the laser with the intensity FWHM of 40 fs, in figure (5.15)-(b), with the FWHM intensity of 10 fs. It is possible to note the great differences among the various cases. Firstly, the overdense case is almost not visible due to its low energy. Secondly, the 0.95 n_c case for the shorter pulse in addition to the higher energy, presents a higher number of accelerated protons. The great increase in the efficiency can be justified by this.

Also, in table (5.5) the results for the simulation of the optimal case performed in Smilei in order to compare the results between the two simulation codes are presented. No significant differences can be observed in proton acceleration by comparing the results obtained from Smilei and WarpX.

Foam thickness	E_p^{max} **[keV]**	$\bar{E}_p$ **[keV]**	T_p **[keV]**	**Efficiency** η **[-]**
	Laser FWMH = 10 fs			
0.95 n_c	1021.02	106.34	162.40	3.04%

Table 5.5: Summary of the results for proton acceleration in the sub-TW laser simulation for the 0.95 n_c case performed with Smilei when the intensity FWHM of the laser is equal to 10fs. The columns show in order the proton maximum energy, the mean proton energy, the temperature associated with the proton spectrum and the laser energy conversion efficiency into kinetic energy of the protons.

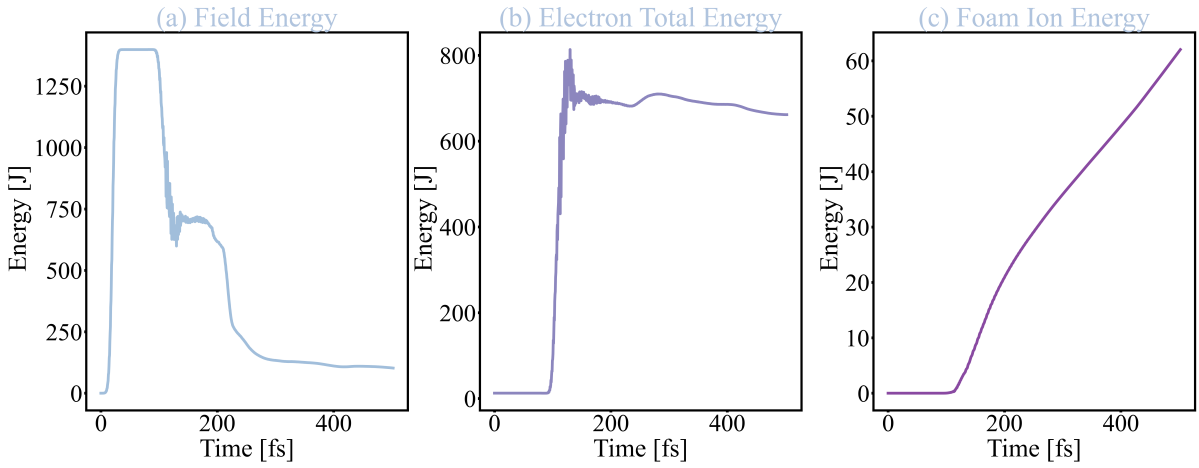

Figure 5.16: In (a) the evolution of the total field energy in the Smilei simulation with 0.95 n_c foam is shown, in (b) the evolution of the total kinetic energy of the electrons and in (c) the total kinetic energy of the foam ions.

In figure (5.16), the energy behaviour of field and particle energy is shown. The evolution

of the field is shown in figure (5.16)-(a), the total electron kinetic energy in figure (5.16)-(b) and the total kinetic energy of the foam ions in figure (5.16)-(c).

The same behaviour retrieved from WarpX simulations can be observed, even though it is possible to notice slightly higher field energy in the Smilei simulation. This effect depends on the differences in the electromagnetic field initialisation between the two codes.

In figure (5.17) the proton spectrum retrieved from Smilei simulation is shown.

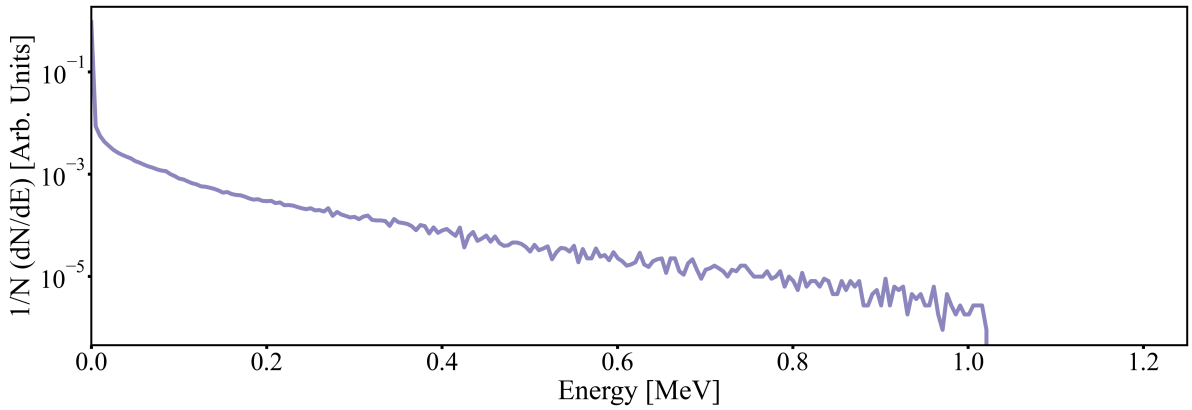

Figure 5.17: Plot of the proton spectrum retrieved 250fs after the first interaction in the optimal case with 0.95 n_c foam for sub-TW laser with 10 fs of intensity FWHM performed with Smilei.

No noticeable difference is shown with respect to the corresponding WarpX simulation spectrum. Thus, it is possible to use indifferently one or the other code to simulate proton acceleration when one wants to use features which are the sole prerogative of one of the two codes.

5.4. Effects of reduced dimensionality

5.4.1. Set-up of a 3D homogeneous simulation of the 20 TW laser

In order to assess the effects of the reduced dimensionality on particle and field dynamics a three-dimensional homogeneous simulation for the optimal case was performed. Due to the high computational cost of three-dimensional simulations, which can reach even more than ten times the one of an equivalent two-dimensional simulation, the resolution was decreased with respect to the corresponding case in two dimensions. Again, the use of WarpX was preferred for this investigation to benefit of GPU acceleration. The

simulation parameters were chosen in order to be able to compare the results of the three-dimensional simulation to the two-dimensional relevant one, thus a totally ionised plasma was considered. In order to avoid numerical heating of the electrons, the reduction in resolution had to be accompanied by a decrease in the substrate density: the choice was to set this density as the maximum density at which the simulation can be performed avoiding numerical artefacts, i.e. $80n_c$. Both the foam and the contaminant layer densities remained untouched with respect to the two-dimensional case. The resolution was set to 25 points per micron and the simulation box was reduced in dimensions with respect to the 2D case to reduce the computational cost. Thus, the simulation box was set to $x \times y \times z = 87\lambda \times 62\lambda \times 62\lambda$. In order to be able to simulate the contaminant layer with lower resolution, its thickness had to be slightly increased to 0.05 µm, i.e. to guarantee a density deposition on at least two contiguous cells of the simulation grid.

A different particle sampling was used in order to reduce again the computational cost: one macroion per cell was simulated to sample the ion population of the substrate, one macroion per cell to sample the foam and sixty macroions per cell to sample the contaminant layer; concerning the electrons, instead, ten macroelectrons per cell were used for the substrate electrons, two macroelectrons per cell to sample the foam electrons and sixty macroelectrons per cell to sample the contaminant layer population. The choice of a higher number of particles per cell in the contaminant layer population was again decided to increase their statistics. The simulation duration was set to 300 fs.

Particle boundary conditions were set to be periodic in the dimensions transversal to laser propagation and open boundary conditions in the dimension parallel to the laser propagation. Concerning field boundary conditions, instead, again periodic ones were set in the transversal dimensions and pml in the parallel direction.

5.4.2. Analysis of the results

In table (5.6) a summary of the quantities related to proton energy is presented.

It is readily possible to notice that by comparing the values with the ones obtained by the same case in the two-dimensional simulation in table (5.3), many differences are present. The maximum proton energy results, in fact, around 10 MeV lower than the two-dimensional case. In particular, the greatest difference can be observed in the efficiency. The latter was calculated as the total kinetic energy of the protons on the total field energy of the pulse before interaction. The three-dimensional case shows an efficiency which is four times lower than the two-dimensional one. A lower number of protons, thus, is accelerated by the laser. A great reduction can be seen, also, when considering the mean

Foam thickness	E_p^{max} (MeV)	$\bar{E}_p$ [MeV]	T_p [MeV]	Efficiency η [-]
	Substrate Thickness = 0.2 µm			
4 µm	23.94	2.13	2.91	2.47%

Table 5.6: Summary of the results for proton acceleration in the 20-TW laser 3D homogeneous simulation for the optimal case of foam thickness 4 µm and density 2.6 n_c performed with WarpX. The columns show in order the proton maximum energy, the mean proton energy, the temperature associated with the proton spectrum and the laser energy conversion efficiency into kinetic energy of the protons.

proton energy and the temperature associated with the spectrum. These latter values in the 3D simulation are less than half the corresponding ones in the 2D simulation.

In figure (5.18), the field and particle energy behaviour in time is shown. The evolution of the field energy is shown in figure (5.18)-(a), the total electron kinetic energy in figure (5.18)-(b) and the total kinetic energy of the foam ions in figure (5.18)-(c).

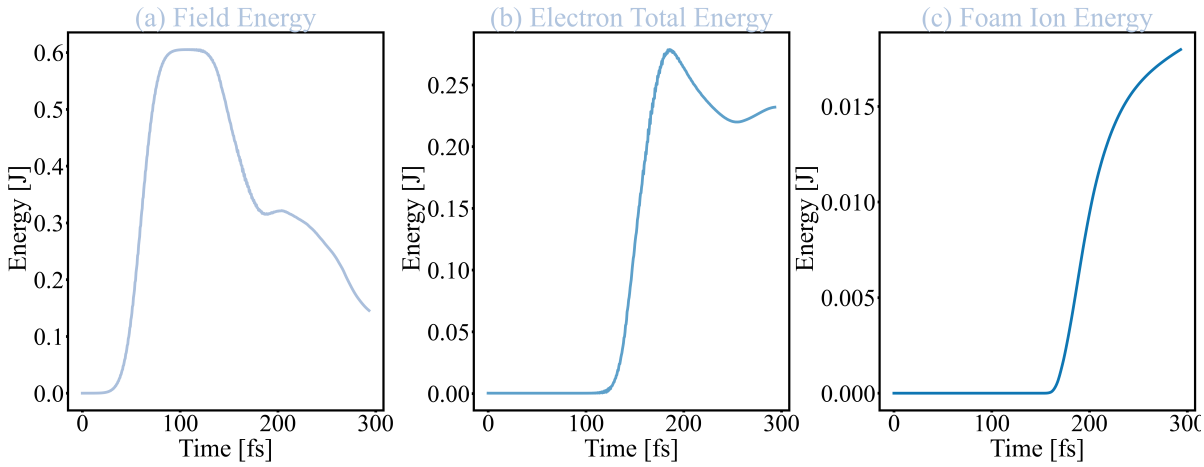

Figure 5.18: In (a) the evolution of the total field energy in the 3D simulation with 4 µm 2.6 n_c homogeneous foam simulation is shown, in (b) the evolution of the total kinetic energy of the electrons and in (c) the total kinetic energy of the foam ions.

When considering the behaviour associated with the total energy of the field and of the particles no direct comparison can be done with the one observed in two-dimensional simulations. The latter ones, in fact, cannot predict the total energy due to the loss of a dimension and the results are given in units of energy over length. However, a comparison considering the ratio between the maximum field energy and the energies evaluated at each time-step can be significant. Indeed these ratios are dimensionless. If considering the ratios, even from the comparison between the two plots in figure (5.18)-(a) and figure

(5.7)-(a) it is possible to observe that right after the interaction with the target, the field energy absorption happening in the two-dimensional simulation is more effective than in the three-dimensional simulation. It is also worth mentioning that, from figure (5.18)-(c), one can observe that the foam ions at the end of the simulation, have not still reached a plateau in their total energy.

In figure (5.19) the proton energy spectrum retrieved at the end of the simulation is shown.

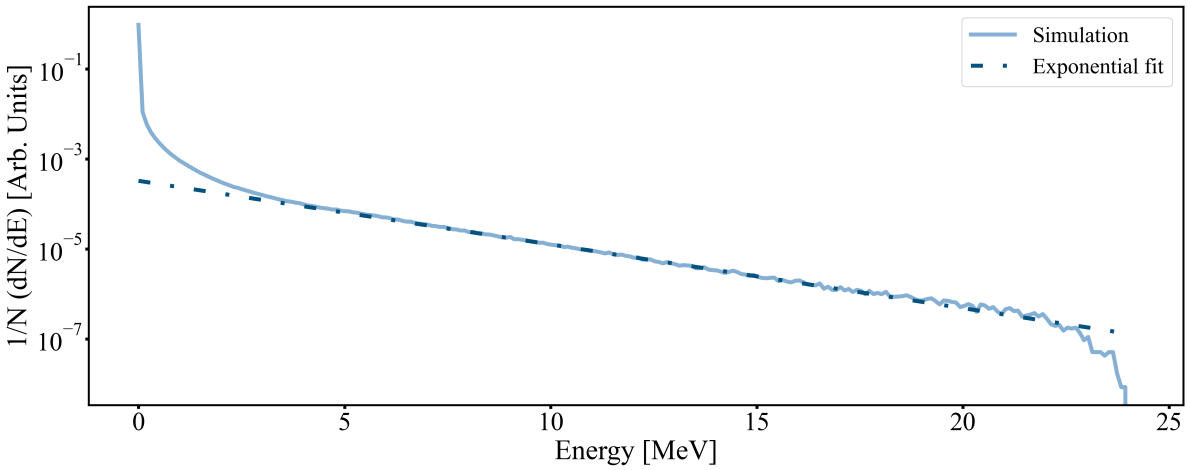

Figure 5.19: Plot of the proton spectrum retrieved at the end of the 3D simulation in the optimal case (4 µm and 2.6 n_c) for the 20 TW laser performed with WarpX.

It is possible to observe that a good accordance between the exponential distribution and the proton spectrum is observable at least in the central part of the spectrum. When comparing to the ones presented in figure (5.10)-(a) one can immediately observe differences. Firstly maximum proton energy in two-dimensional simulations is always higher than the one retrieved from the three-dimensional one. Secondly, a lower number of accelerated particles is seen in the 3D case. Also, a higher slope is observable in the 3D simulation proton spectrum, leading to a reduction in the mean energy/temperature of the protons.

In figure (5.20), it is possible to observe two interesting shots obtained from the 3D simulation.

The first shot, i.e. figure (5.20)-(a), shows the first instants of laser interaction with the foam of the target, in which hot electrons are generated.

In the second shot, i.e. figure (5.20)-(b), it is possible to observe two different phenomena: the first, visible thanks to the cross-section of the target, is the expansion of the electron on the rear face of the target; the second is that protons are mostly accelerated in the central region of the laser spot.

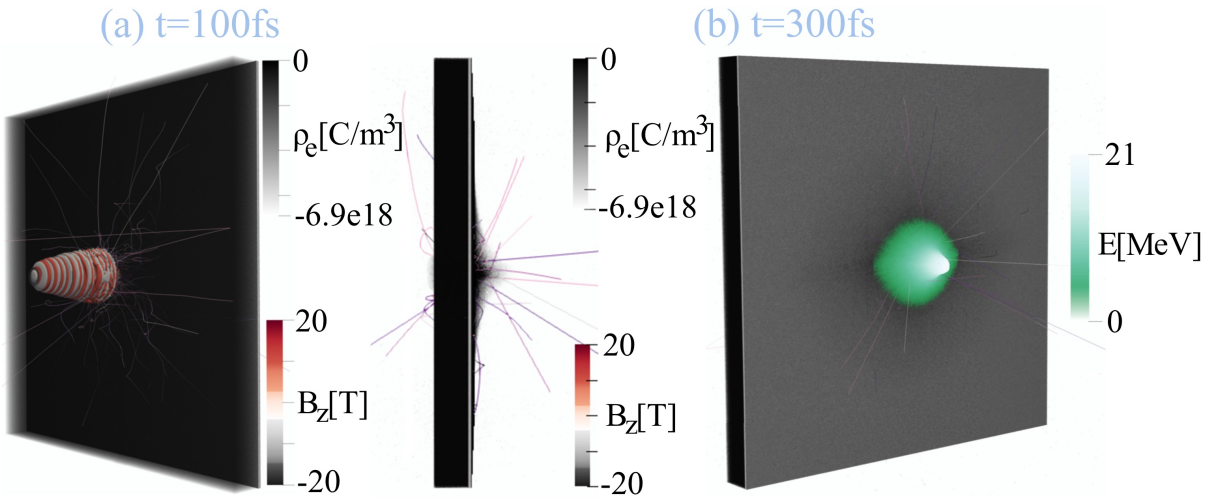

Figure 5.20: Electron charge density ρ_e in international system units at two different time-steps in the homogeneous 3D simulation with 2.6 n_c 4 µm foam. In (a) the moment of interaction between the laser (B_z field contour) and the plasma is shown. In (b) the electron density at the final time-step of the simulation is shown both in cross-section and rear-surface together with the positions of some sampled protons at the end of the simulation. Protons are coloured according to their energy E. The trajectories of some sampled electrons are always shown in purple.

5.5. Effects of nanostructured foam

5.5.1. Set-up and analysis of a 3D simulation of the 20 TW laser

In order to evaluate the effects of the presence of the nanostructure when considering the interaction between the 20TW laser and the double-layer target a three-dimensional simulation has been performed in the same conditions shown in section (5.4.1). The simulation was, however, performed with the Smilei code, even though the benefit of the GPU acceleration is lost. The choice was made to be able to insert as input the density of the nanostructure which, due to memory limitations, could not be used in WarpX. The simulation box and the boundary conditions were chosen with the same logic used in the homogeneous simulation. The choice of the set-up for sampling the density was the same as the homogeneous case when considering the substrate and the contaminant layer, while some considerations on the foam morphology brought the necessity of different configurations in its set-up.

The foam morphology was an output of the aforementioned DLCCA code. Its average density was 2.6 n_c and its average thickness 4.0 µm. The morphology consists of nanopar-

ticles the density of which is 20.78 n_c and the diameter of which is 80.0 nm. Such density and thickness are not realistic ones for the particles, however, their choice falls almost in the maximum resolution which can be used in 3D simulations without a prohibitive computational cost. The foam density was sampled with 20 macroelectrons per cell and 2 macroions per cell. All the species were modelled as completely ionised plasmas.

In table (5.7) a summary of the quantities related to proton energy is presented.

Foam thickness	E_p^{max} **[MeV]**	$\bar{E}_p$ **[MeV]**	T_p **[MeV]**	**Efficiency** η **[-]**
	Substrate Thickness = 0.2 µm			
4 µm	15.05	1.85	2.20	4.58%

Table 5.7: Summary of the results for proton acceleration in the 20-TW laser 3D nanostructured simulation for the optimal case (4 µm and 2.6 n_c) performed with Smilei. The columns show in order the proton maximum energy, the mean proton energy, the temperature associated with the proton spectrum and the laser energy conversion efficiency into kinetic energy of the protons.

By comparing the values in the table above and the ones in table (5.4.1), it is possible to make some significant observations. It is, firstly, possible to notice a great reduction in the maximum proton energy retrieved when the nanostructure presence is considered in the simulation. This reduction is accompanied by a reduction of both the mean energy and the temperature of the protons. This latter reduction is, however, less prominent than the one regarding proton maximum energy. Despite the reduction in the other values, a considerable increase in the efficiency is noticeable. This is related to a higher number of protons being accelerated with a lower mean energy. The efficiency results in around double the homogeneous case efficiency and it is comparable with certain values obtained in the 2D simulations.

In figure (5.21) the field and particle energy behaviour in time is shown. The evolution of the field is shown in figure (5.21)-(a),the total electron kinetic energy in figure (5.21)-(b) and the total kinetic energy of the foam ions in figure (5.21)-(c).

By comparing the results with the ones shown in figure (5.18) it is possible to make some observations.

Firstly by looking at figure (5.21)-(a), immediately one can observe that a lowering in field energy absorption happens when the nanostructure is present. This behaviour can be captured in total electron energy too. Electrons gain less energy in the nanostructured case. Despite the lower absorption by electrons in the plasma, it is however possible to observe an opposite trend in foam ion energy: the ions which are present in the foam

absorb more energy when a nanostructure is present. Even in this case however, it is possible to notice that the energy of the ions has not reached a plateau: it is probable that the ion energy retrieved from this simulation is not the maximum value that ions can reach.

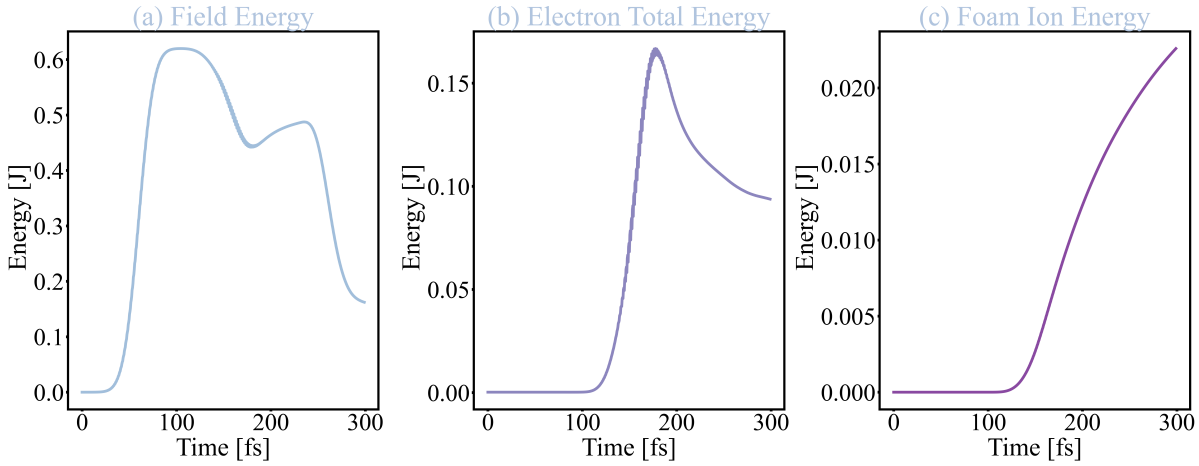

Figure 5.21: In (a) the evolution of the total field energy in the specific 3D simulation with 4 µm 2.6 n_c nanostructured foam is shown, in (b) the evolution of the total kinetic energy of the electrons and in (c) the total kinetic energy of the foam ions.

In figure (5.22), the proton energy spectrum retrieved at the end of the simulation is shown.

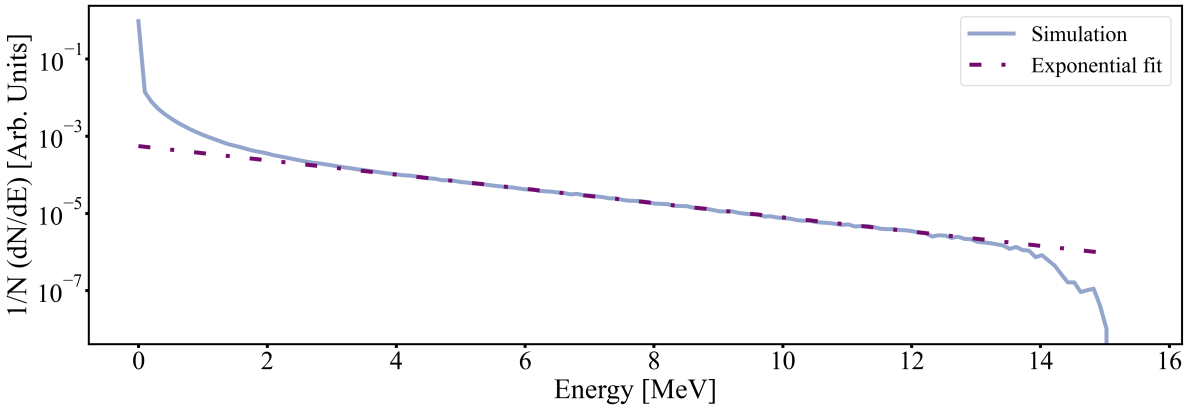

Figure 5.22: Plot of the proton spectrum retrieved at the end of the 3D simulation with 4µm 2.6nc nanostructured foam in the optimal case for 20-TW laser performed with Smilei.

Even in this case, it is possible to observe a good accordance between the exponential distribution and the proton spectrum in its central part. The temperature can thus be a

good indicator of the mean energy of the protons. It is possible, also, to notice a higher number of protons at low energies when comparing the spectrum to the homogeneous case one. This is related to the increase in the efficiency.

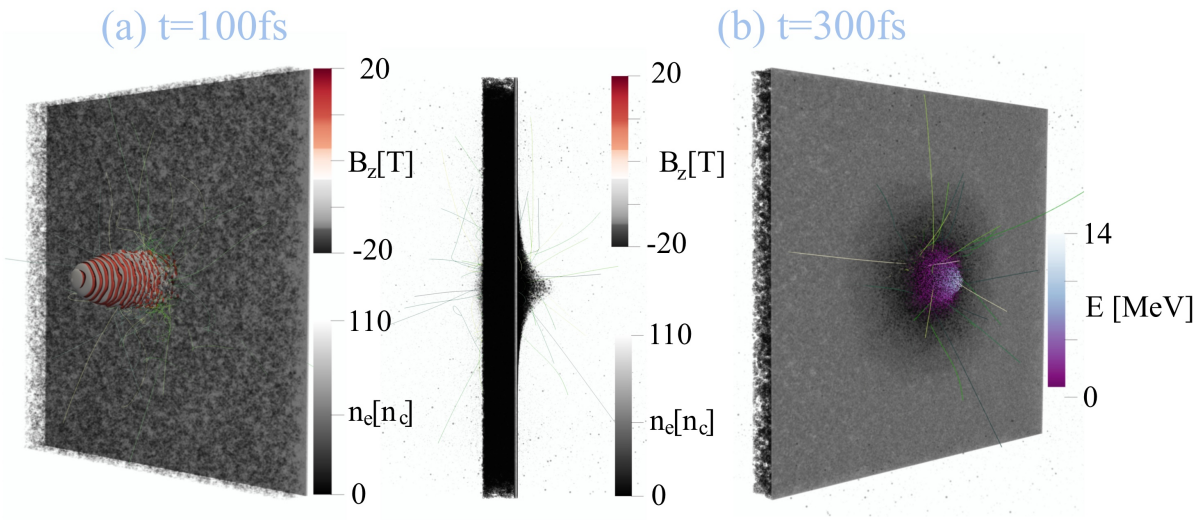

Figure 5.23: Electron density n_e in units of n_c at two different time-steps (3D nanostructured simulation of the 4 µm and 2.6 n_c foam and 200 nm substrate). In (a) the moment of interaction between the laser (B_z field contour) and the plasma is shown. In (b) the electron density at the final time-step of the simulation is shown in cross-section and together with the trajectories of some sampled protons coloured according to their energy E. The trajectories of some sampled electrons are always shown in green.

In figure (5.23), two different shots from the 3D simulations are shown. In figure (5.23)-(a), it is possible to observe again the expansion of the first electrons heated by the laser. In figure (5.23)-(b), it is possible to observe a cross-section of the target at the end of the simulation time in which the rear expansion of the hot electrons is present and the rear side of the target together with the final positions of some sampled protons. The same comments made for the homogeneous case can be made for the nanostructured case. However, it is possible to observe the morphology of the nanostructure in the latter case.

5.5.2. Set-up of 2D simulations of the sub-TW laser

In order to investigate the effects of the presence of a nanostructure in the interaction between the sub-TW laser and the target, firstly a set of two-dimensional simulations was performed.

A first set was performed by using WarpX considering both 40 fs and 10 fs laser configurations. The box, the resolution, the boundary conditions and the target position were

chosen accordingly to the ones in section (5.2.2).

A 4 µm nanostructure, retrieved as a slice of the three-dimensional DLCCA numerical foam used in section (5.5.1), was used in two different conditions: a foam average density of 0.95 n_c and a foam average density of 3 n_c. As previously stated in section (5.2.2), when referring to foam density one always refers to the density of the foam as if it was completely ionised. The foam morphology is composed of circular carbon particles the diameter of which is 80 nm. As a first approximation, to vary the average density of the foams, the density of the nanoparticles was varied keeping it in the overdense region. The lower density case was simulated with nanoparticles having an ion number density of 1.45 n_c, while the higher density case with a ion number density of 4.68 n_c. Due to WarpX limitations, the ionisation process was not accounted for in these cases. The foam electron density, thus, was chosen in order to keep the same total number of electrons generated in the homogeneous case, multiplying the ion number density by an approximation of the mean ionisation shown in table (5.1) for the relevant density case.

Concerning the substrate, the same choice as in (5.2.2) was made concerning the thickness. By analysing the mean ionisation state shown in (5.1) the choice was to consider the substrate as a three-time ionised aluminium substrate. The contaminant layer was instead simulated accordingly to the choices made before.

The number of macroions and macroelectrons per cell was the same as in previous sections for what concerns substrate and contaminant layer. Since the foam is a nanostructured foam, instead, composed of overdense macroparticles, the choice was to sample the foam electron population with 8 macroelectrons per cell for the lower density foam and 28 macroelectrons per cell for the higher density foam. An analogous decision was taken for the foam ion population.

The second set of simulations was performed instead with Smilei. In order to be able to observe whether the presence of the nanostructure can cause differences in the ionisation process, a simulation of the optimal case was performed considering also the tunnel ionisation effect. To have a comparison with an equivalent case, an analogous simulation neglecting the ionisation effect was also performed.

The choice in the box dimensions, resolution and boundary conditions were always the same as in the first set. Also, the target position is set as before.

Concerning the simulation which considered the ionisation effect, the substrate and the contaminant layers were modelled as in section (5.2.2); when considering the simulation which neglected the ionisation effect, the modelisation was the same as the other simu-

lations accounting for the nanostructure presence previously performed in WarpX. Only the laser configuration which brought to the optimal condition was simulated, i.e. the one with a shorter pulse FWHM.

The main difference in these Smilei simulations with respect to WarpX ones can be found in the foam morphology: a different nanostructure is in fact used. The mean thickness and density of the foam were simulated to be equal to the one leading to the higher proton energy, i.e. having a thickness of 3µm and a density of 0.95 n_c when considering the atoms as completely ionised. The morphology is composed of particles having a diameter measuring 50 nm and the ion density of which is 3.09 n_c. When the ionisation process was accounted for the foam was modelled as a neutral carbon foam. The ion density was sampled with 4 macroions per cell. In the case which did not account for the ionisation process, again 4 macroions per cell were simulated to sample the ion density, while 10 macroelectrons per cell were used for sampling the electron population. The electron density of each macroparticle was chosen to keep the total number of electrons constant with respect to the number of electrons generated in the simulation accounting for ionisation, i.e. 12.36 n_c. It is important to notice that the nanostructure used in these last simulations was retrieved as a section of a numerical foam produced by the means of the DLCCA code formed by 16800 diffusing clusters containing 50 particles each.

5.5.3. Set-up of a 3D simulation of the sub-TW laser

A three-dimensional simulation was performed taking into account the ionisation effect. The choice of considering them was done on the basis of the two-dimensional simulations which showed a non-negligible effect of the ionisation process in the interaction between a sub-TW laser and a target. Also, due to the reduction in the number of total particles in the simulation, the computational cost does not increase prohibitively due to the Monte Carlo process involving ionisation.

The simulated case was the one which was shown to be optimal for proton acceleration by 2D simulations, i.e. the laser with a shorter pulse and the 0.95 n_c foam. The simulation box, the resolution and the boundary conditions were the same as the ones in section (5.5.1).

The substrate was modelled as a three-times-ionised aluminium substrate, as usual, to account for the free electrons in the metal, with a thickness of 1 µm and an ion number density of 6.15 n_c. The reduction in the density with respect to the real aluminium density is due to the necessity of performing a simulation with a lower resolution in order to limit the computational cost associated with the simulation. The contaminant layer

was simulated as a 0.05 µm completely ionised hydrogen layer at the rear face of the target. Its density was set to $10n_c$. The aluminium ions were sampled with 1 macroion per cell while the electrons were with 10 macroelectrons per cell. Both contaminant electrons and ions were sampled with 60 macroions per cell.

The carbon foam was modelled as a DLCCA foam retrieved from the simulation of a numerical foam composed of 16800 clusters each containing 50 nanoparticles. The mean thickness and density were computed as 3.07 µm and 0.95 n_c. The morphology is composed of particles having a diameter of 50.0 nm and an ion number density of 4.17 n_c. The choices in the density and the diameter are again made in order to be able to solve them within the given constraints in the resolution. Further explanations are given in section (4.3.1). The foam was simulated as a neutral material and the ion density was sampled with 2 macroparticles per cell.

5.5.4. Analysis of the results of the sub-TW laser simulations

In table (5.8) the results from the two-dimensional simulations performed with WarpX are summarised.

Foam thickness	E_p^{max} **[keV]**	$\bar{E}_p$ **[keV]**	T_p **[keV]**	**Efficiency** η **[-]**
	Laser FWMH = 40 fs			
0.95 n_c	465.46	65.91	108.30	0.71%
3 n_c	135.14	28.52	35.98	0.10%
	Laser FWMH = 10 fs			
0.95 n_c	515.51	62.76	124.35	1.04%
3 n_c	300.30	41.19	74.37	0.51%

Table 5.8: Summary of the results for proton acceleration in the sub-TW laser with nanostructured foams of different thicknesses. The first row of the table summarises the results obtained when the intensity FWMH of the laser is equal to 40 fs and the second the results obtained when the intensity FWHM of the laser is equal to 10 fs. The columns show in order the proton maximum energy, the mean proton energy, the temperature associated with the proton spectrum and the laser energy conversion efficiency into kinetic energy of the protons.

By comparing these values with the ones retrieved in the table (5.4), it is possible to observe a reduction in the proton maximum energy and efficiency concerning the optimal case. The other cases, instead, show an increase in both efficiency and energy in the presence of the nanostructure.

In figure (5.24), the variation of the field energy in time is reported. In figure (5.24)-(a),

the results for the laser with an intensity FWHM of 40 fs are shown, while in figure (5.24)-(b), the ones for the laser with an intensity FWHM of 10 fs are shown. By comparing these plots with the ones retrieved from the homogeneous simulations, it is possible to observe an increased absorption of the electric field related to the nanostructure. The highest laser absorption is shown in the higher-intensity laser configuration, confirming the results observed in the homogeneous cases.

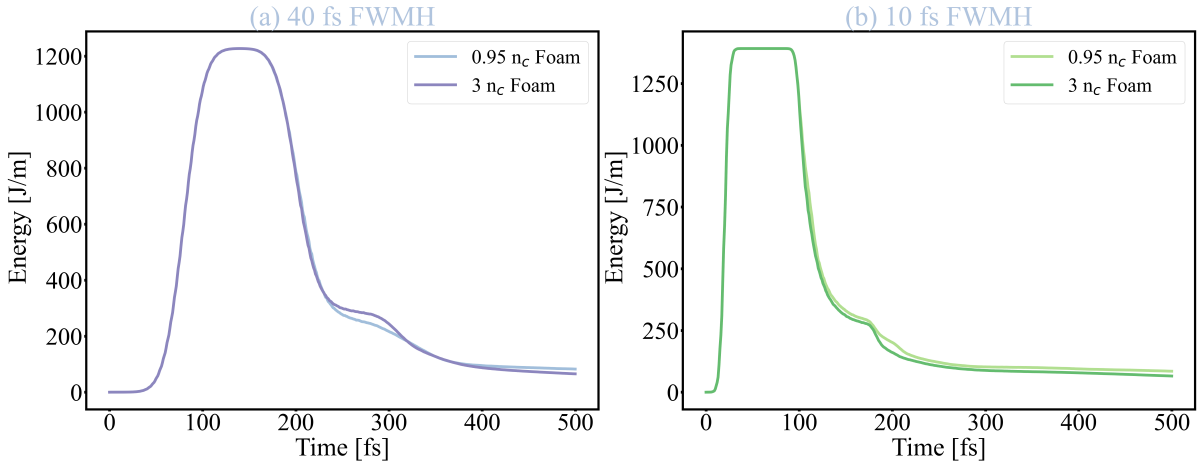

Figure 5.24: Plots of the total energy associated with the electromagnetic field evolution in time of the 2D nanostructured simulations of the sub-TW laser performed in WarpX. In (a) the results from the laser with 40 fs in intensity FWHM and in (b) the ones from the laser with 10 fs in intensity FWHM. In all cases, the darkest colour is associated with the highest foam density.

In figure (5.25), the time behaviour of the total energy associated with the electrons is shown. In figure (5.25)-(a), the results for the laser with an intensity FWHM of 40 fs are shown, while in figure (5.25)-(b), the ones for the laser with an intensity FWHM of 10 fs. In most cases, particularly when comparing the overdense foams, it is possible to see an increase in the total electron energy as an effect of the nanostructure. In the optimal case, the opposite effect is instead observed. When the foam is the 0.95 n_c in the higher intensity laser case in fact the electron energy is higher in the homogeneous case.

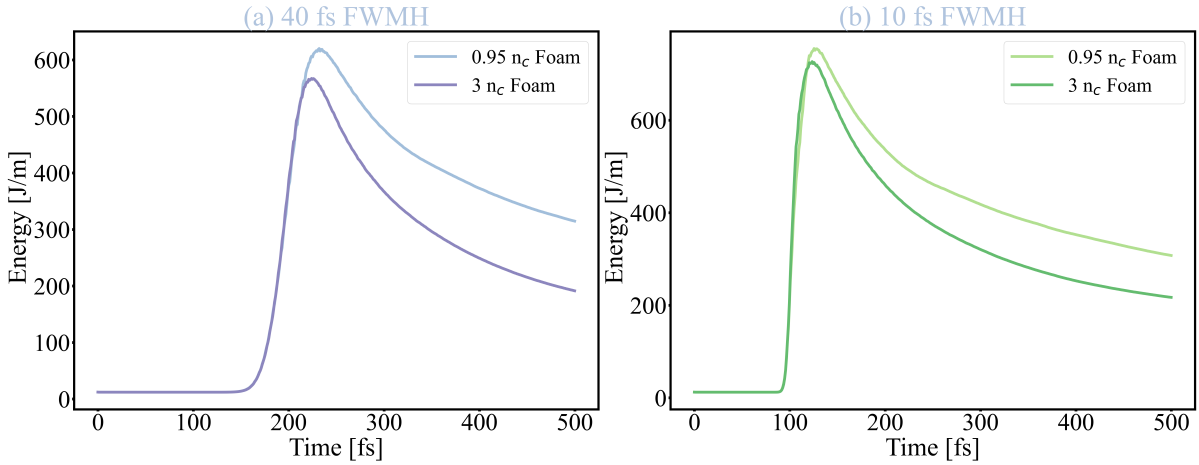

Figure 5.25: Plots of the total electron energy evolution in time of the 2D nanostructured simulations of the sub-TW laser performed in WarpX. In (a) the results from the laser with 40 fs in intensity FWHM and in (b) the ones from the laser with 10 fs in intensity FWHM. In all cases, the darkest colour is associated with the highest foam density.

In figure (5.26) the time evolution of the energy of the foam ions is shown.

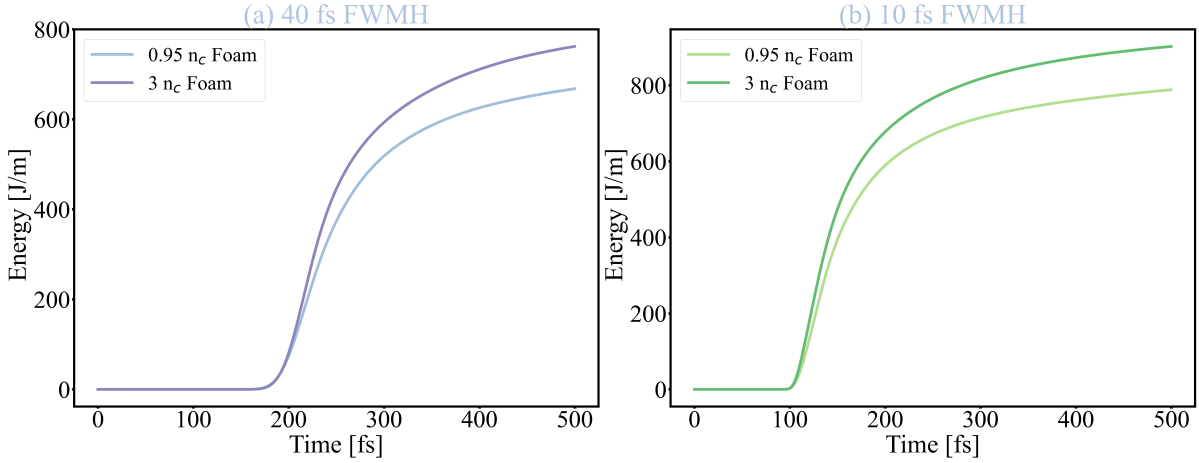

Figure 5.26: Plots of evolution in time of the total kinetic energy of foam ions of the 2D nanostructured simulations of the sub-TW laser performed in WarpX. In (a) the results from the laser with 40 fs in intensity FWHM and in (b) the ones from the laser with 10 fs in intensity FWHM. In all cases, the darkest colour is associated with the highest foam density.

In figure (5.26)-(a) the results for the laser with an intensity FWHM of 40 fs are shown, while in figure (5.26)-(b) the ones for the laser with an intensity FWHM of 10 fs. Concerning the foam ion energy, a great increase in its value is observed in all the cases in

which the nanostructure is accounted for. This increase is coherent, also, with what was seen previously in the 20 TW laser case. The nanostructure seems to play an important role in the conversion of the laser energy into the kinetic energy of the foam ions.

In figure (5.27), it is possible to observe the proton spectra retrieved from the simulations 250fs after the interaction between the substrate and the laser pulse. In figure (5.27)-(a), the ones from the laser with the intensity FWHM of 40 fs, in figure (5.27)-(b), with the intensity FWHM of 10 fs.

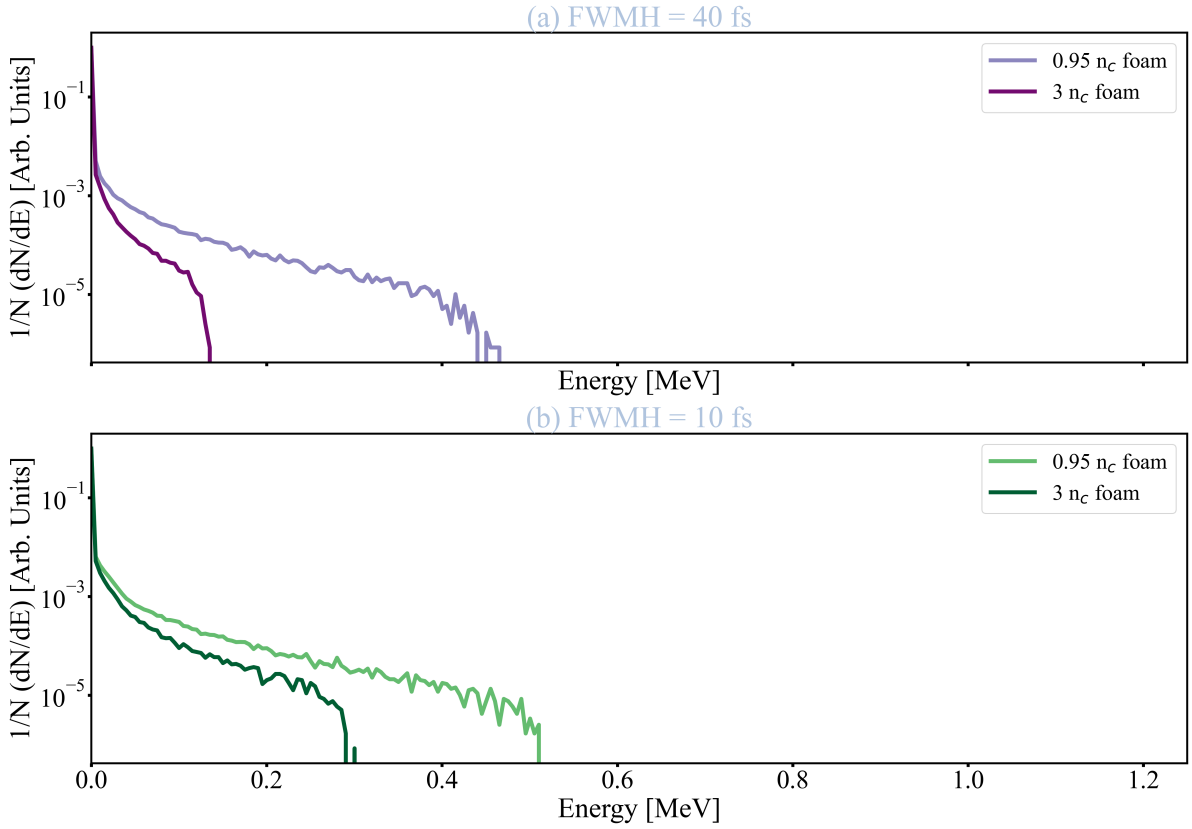

Figure 5.27: Plots of the proton spectra retrieved 250fs after the first interaction in the 2D simulations with nanostructured foam and sub-TW laser performed with WarpX. In (a) the results from the laser with 40 fs in intensity FWHM and in (b) the ones from the laser with 10 fs in intensity FWHM. In all cases, the darkest colour is associated with the highest foam density.

Again, the choice of the time at which extracting the spectra was only made in order to be able to compare the different conditions. As observable, also, from the table (5.8), a reduction in the energy of the protons is shown in the optimal case. The nanostructure seems to be beneficial in the worst cases, leading to comparable maximum energies among all the conditions. The central part of all spectra is linear in the logarithmic scale: the

approximation with the exponential distribution is then a good approximation in that region.

The results of the simulation performed with the nanostructure in the optimal density (0.95 n_c 3.0 µm) and thickness conditions both when considering the ionisation process and when neglecting it are presented in table (5.9). These simulations were performed with Smilei.

Foam thickness	E_p^{max} **[keV]**	$\bar{E}_p$ **[keV]**	T_p **[keV]**	**Efficiency** η **[-]**
	Tunnel Ionisation			
0.95 n_c	545.54	61.36	141.29	1.47%
	No Tunnel Ionisation			
0.95 n_c	470.07	53.31	108.98	1.07%

Table 5.9: Summary of the results for proton acceleration in the sub-TW laser obtained in the nanostructured 2D simulations for 0.95 n_c performed in Smilei. The first row of the table summarises the results obtained when the tunnel ionisation process is accounted for and the second when it is neglected. The columns show in order the proton maximum energy, the mean proton energy, the temperature associated with the proton spectrum and the laser energy conversion efficiency into kinetic energy of the protons.

It is possible to observe that results similar to the ones in table (5.8) are retrieved. The first observation which can be made is about the efficiency in the conversion of the field energy in proton energy. The ionisation process, in fact, seems to impact in a positive way the conversion of laser energy into kinetic energy of the protons. The same enhancement was shown in section (5.2.1) for the 20TW case, meaning the ionisation process influence in a non-negligible way the acceleration of the contaminant ions.

In figure (5.28) it is possible to observe the evolution of the energy of the field and the particles during the simulation. The evolution of the field is shown in figure (5.28)-(a), the total electron kinetic energy in figure (5.28)-(b) and the total kinetic energy of the foam ions in figure (5.28)-(c).

Both cases present a similar behaviour concerning the field energy. However, as expected from the values in table (5.9), the absorption of the field energy is more pronounced when the ionisation process is accounted for. Also, it is possible to note great differences in foam ion energy, meaning that probably the difference in the absorption of the electromagnetic field energy depends on the foam ionisation. The greatest difference is however encountered in the total electron energy, which seems to increase more when the tunnel ionisation is not included in the treatment. This increase in the total energy is due to the heating of the substrate electrons starting around 200fs after the start of the simulation.

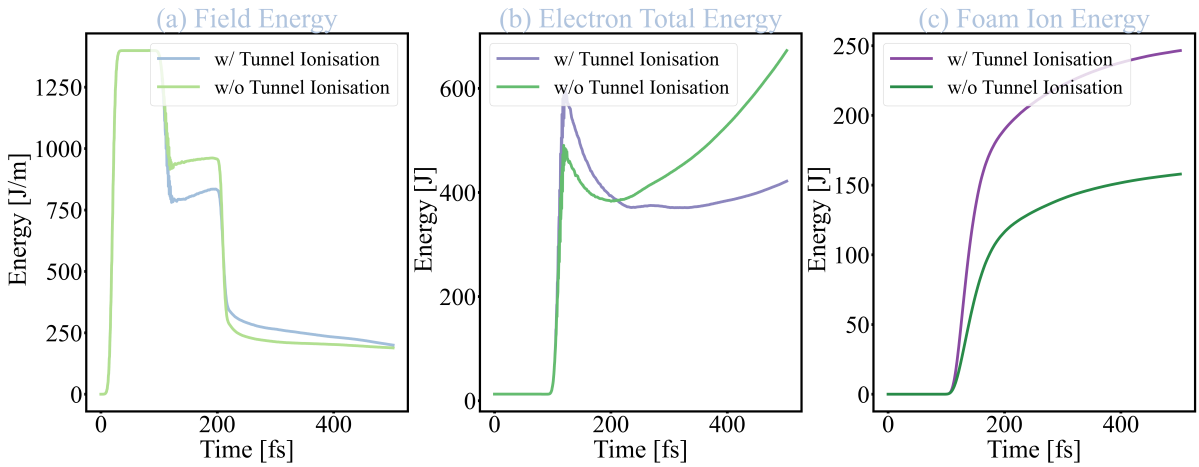

Figure 5.28: In (a) the evolution of the total field energy in the nanostructured 2D simulations for 0.95 n_c performed in Smilei is shown, in (b) the evolution of the total kinetic energy of the electrons and in (c) the total kinetic energy of the foam ions. The plots in green represent the case performed without considering the tunnel ionisation process, the ones in purple represent the case accounting for it.

In table (5.10) the most important parameters related to the ionisation process are summarised.

Foam density	Z^{*-max}_{foam} [-]	$\bar{Z}^{*}_{foam}$ [-]	Z^{*-max}_{subs} [-]	$\bar{Z}^{*}_{subs}$ [-]
	Laser FWMH = 10 fs			
0.95 n_c	6	4.093	13	3.534

Table 5.10: Summary of the state of ionisation of the species in the 2D nanostructured simulation performed with Smilei. The first two columns regard respectively the maximum and mean foam ionisation state, the last two the maximum and mean substrate ionisation state.

One can observe that both the mean ionisation level of the foam and of the substrate increase with respect to the corresponding homogeneous case. Of particular importance is the increase in the mean ionisation level in the substrate. It is, in fact, accompanied by an increase also in the maximum ionisation level of the aluminium. Aluminium ions having the maximum achievable charge are, in fact, observed. It is important, thus, to know where these ionised ions are located and, also, the distribution in the ionisation level.

In figure (5.29) the ionisation maps relative to the nanostructure and the substrate are presented. Concerning figure (5.29)-(a), it is possible to observe that in the laser channel

the foam is completely ionised and that the rest of the foam has a high grade of ionisation. Considering, instead, figure (5.29)-(b), one can note that, as in the homogeneous foam case, the greatest part of the ionisation processes in the substrate happens in the laser propagation direction with an ionisation level around 7. However, on the front surface, some ionisation processes bring the ionisation level of a few particles above 11. This means an intense electric field is present on the front surface of the substrate. The nanostructure, thus, greatly influences the ionisation process, leading to a higher level of ionisation particularly in the substrate.

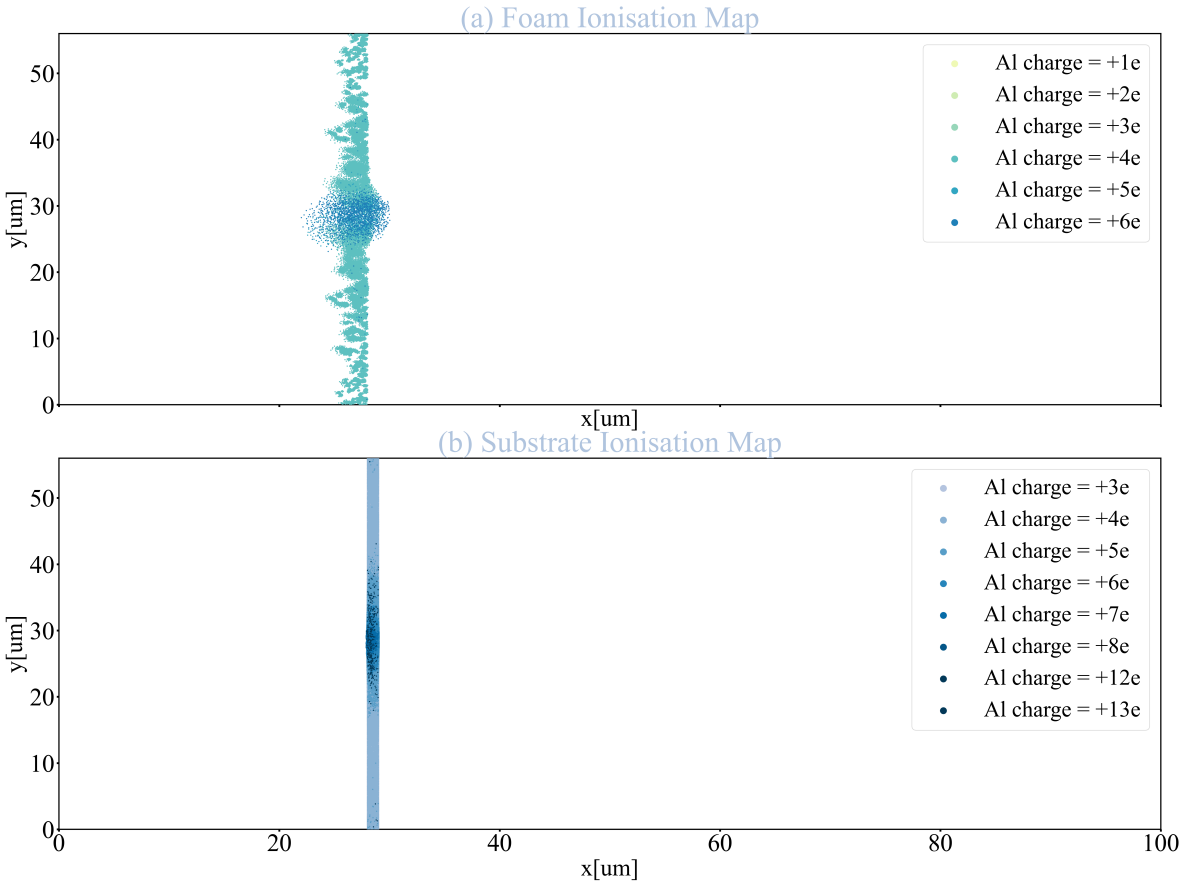

Figure 5.29: Ionisation maps at 500fs for the nanostructured 2D Smilei simulation of the optimal case (0.95 n_c 3.0 µm). In (a) the foam ionisation map is shown, in (b) the substrate ionisation map. The darker colour is related to a higher ionisation level.

In figure (5.30) the plot of the proton spectra retrieved in the two simulations is presented. The comparison between the two spectra allows one to observe that when ionisation is accounted for, the number of protons which are accelerated and their energy are overall higher. Also, no great differences are shown with respect to the corresponding case in average density shown in figure (5.27)-(b).

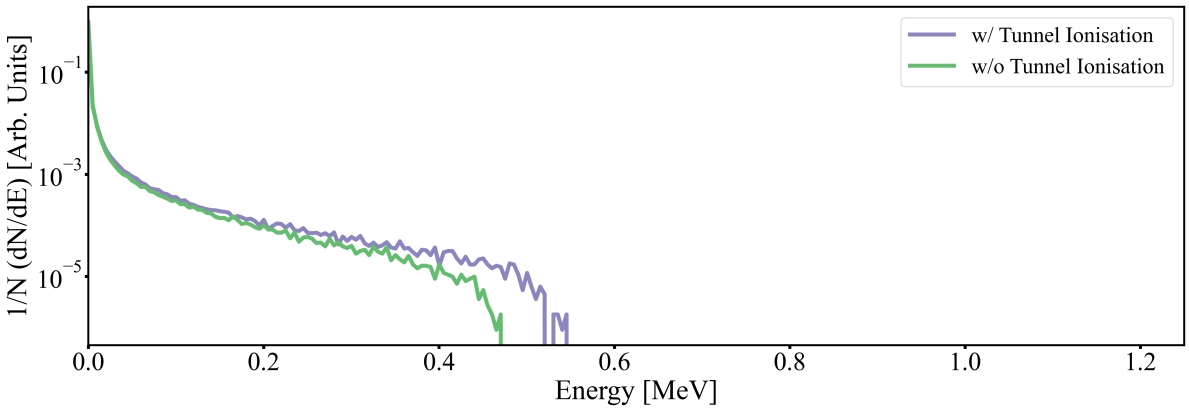

Figure 5.30: Plot of the proton spectra retrieved 250fs after the first interaction the nanostructured 2D simulations for 0.95 n_c performed in Smilei with and without tunnel ionisation.

In table (5.11) the main values retrieved from the three-dimensional simulation performed in Smilei with a 0.95 n_c dense and 3.0 µm thick nanostructured foam are summarised.

Foam thickness	E_p^{max} **[keV]**	$\bar{E}_p$ **[keV]**	T_p **[keV]**	**Efficiency** η **[-]**
	FWMH = 40 fs			
0.95 n_c	135.14	22.74	18.62	0.62%

Table 5.11: Summary of the results for proton acceleration in the sub-TW laser obtained in the nanostructured 3D simulation for the optimal condition (0.95 n_c 3.0 µm) including tunnel ionisation. The columns show in order the proton maximum energy, the mean proton energy, the temperature associated with the proton spectrum and the laser energy conversion efficiency into kinetic energy of the protons.

It is possible to notice a reduction in the maximum proton energy and in the efficiency when comparing the results with the corresponging two-dimensional case in table (5.9).

In table (5.12), the main values to describe the ionisation state of the foam retrieved from the 3D simulation are shown. The decision to show the parameters relative to the foam only is due to the choice of saving only the state of the foam ion macroparticles during the simulation. Saving the macroparticles, in fact, affects the computational time in a non-negligible way.

The results in the table show a great reduction in the mean ionisation level due to dimensional effects. To investigate which are these effects, an ionisation map is presented in figure (5.31).

Foam density	Z_{foam}^{*-max} [-]	$\bar{Z}_{foam}^{*}$ [-]
	Laser FWMH = 10 fs	
0.95 n_c	6	1.983

Table 5.12: Summary of the state of ionisation of the species in the 3D nanostructured simulation performed with Smilei for the optimal condition (0.95 n_c 3.0 µm). The first two columns regard respectively the maximum and mean foam ionisation state.

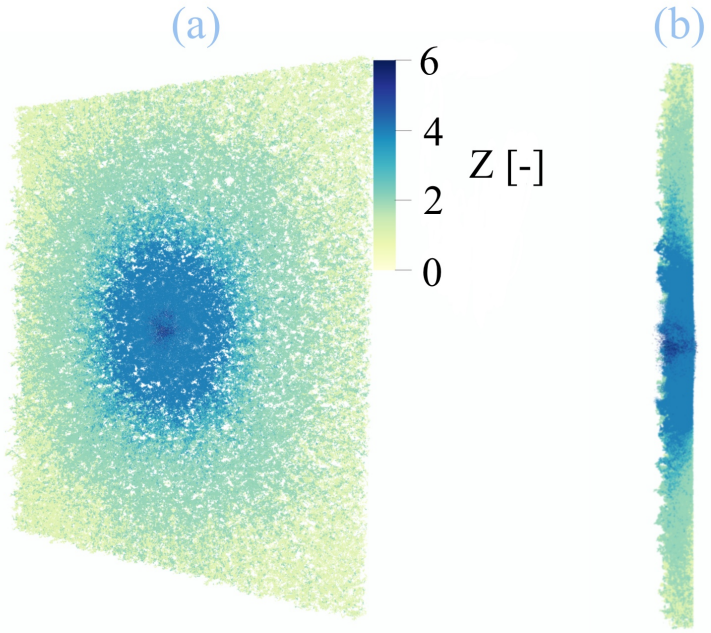

Figure 5.31: Foam ionisation map at 300fs for the nanostructured 3D Smilei simulation of the optimal case. In (a) the foam front surface is shown, in (b) the cross-section cut at half the target. The darker colour is related to a higher ionisation level.

As it is shown in figure (5.31)-(a), it is possible to notice that the geometrical differences between the two-dimensional simulations and the three-dimensional one are the main cause in the reduction of the mean ionisation state. The laser channel, having a circular shape instead of the one of an infinite stripe lead to a lower number of highly ionised atoms. By observing figure (5.31)-(b), one can see that the fully ionised ions can be found in the laser channel. Also, the majority of the highly ionised ions are concentrated near the interaction region.

In figure (5.32), the energy of the particles and of the electromagnetic field is shown. An important absorption of the electromagnetic field by electrons and ions is visible by observing figure (5.32)-(a). Also, it is possible to notice in figure (5.32)-(b) that the electron heating first happens among the foam electrons, while in the last part of the

simulation, the main electron species contributing to the overall electron kinetic energy is the substrate one, which shows an increasing trend. Among the different ion species, the one absorbing the higher part of the energy is the foam ion population, showing, thus, an important role of the nanostructure in the process. In figure (5.32)-(c), their evolution is shown. Also,

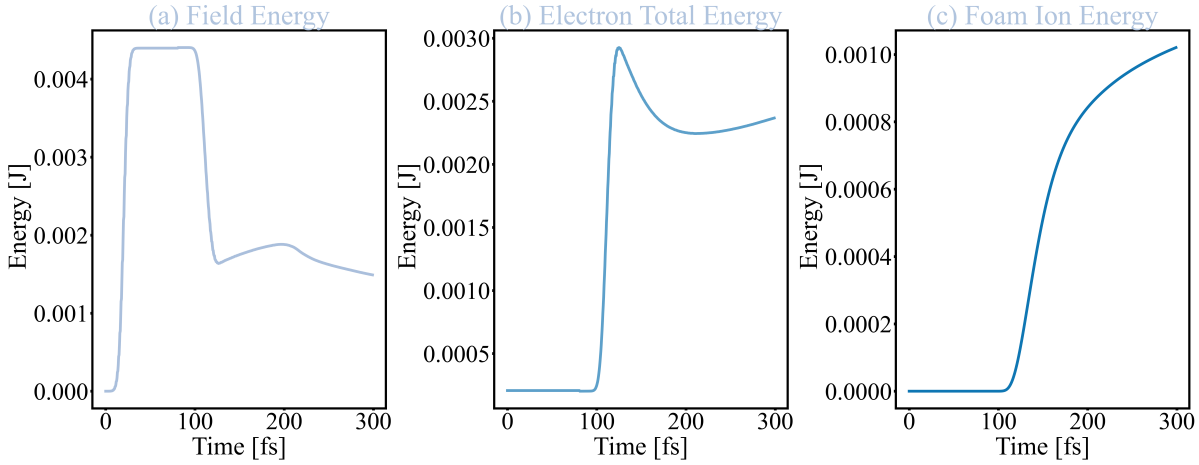

Figure 5.32: In (a) the evolution of the total field energy in the simulation is shown, in (b) the evolution of the total kinetic energy of the electrons and in (c) the total kinetic energy of the foam ions in the 3D nanostructured simulation performed with Smilei for the optimal condition (0.95 n_c 3.0 µm).

In figure (5.33), the spectrum retrieved at the end of the simulation is shown.

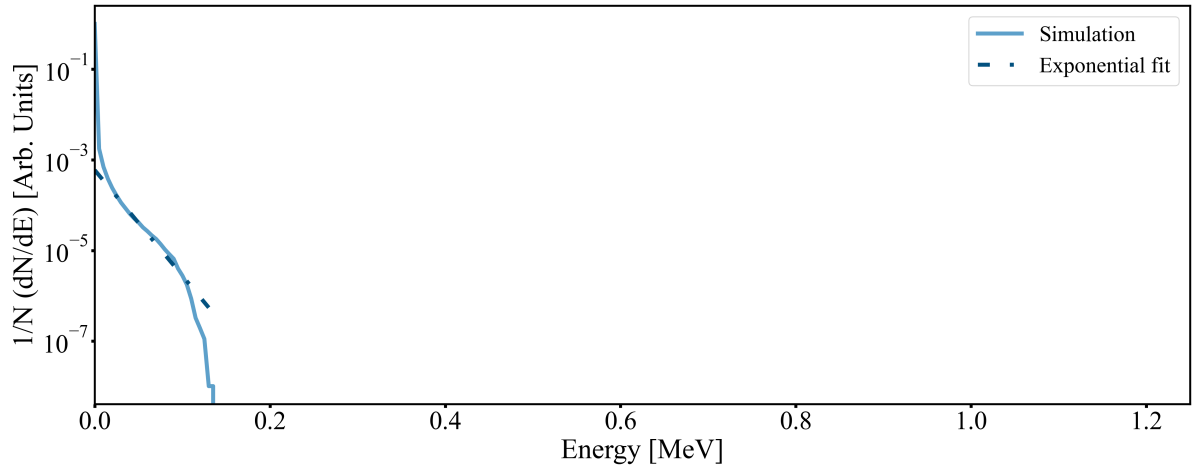

Figure 5.33: Plot of the proton spectrum retrieved at the end of the 3D nanostructured simulation including tunnel ionisation in the optimal case for sub-TW laser performed with Smilei (0.95 n_c 3.0 µm)

The spectrum shows a lower maximum energy when comparing it with the two-dimensional one and also a lower number of particles is accelerated. A consideration on the contaminant ion energy has to be done. Their energy is, in fact, not saturated, meaning the simulation is not showing the highest energy that can be reached by the protons. Both these effects take part in the decrease in the efficiency reported in table (5.11). It is also possible to observe a good agreement between the exponential fit and the spectrum.

In figure (5.34), it is possible to observe two interesting shots obtained from the 3D simulation. The first shot, i.e. figure(5.34)-(a), shows the first instants of laser interaction with the foam of the target, in which hot electrons are created and the ionisation process of the foam is happening. In the second shot, i.e. figure (5.34)-(b) it is possible to observe the acceleration of the protons which is again higher in the central part of the laser spot.

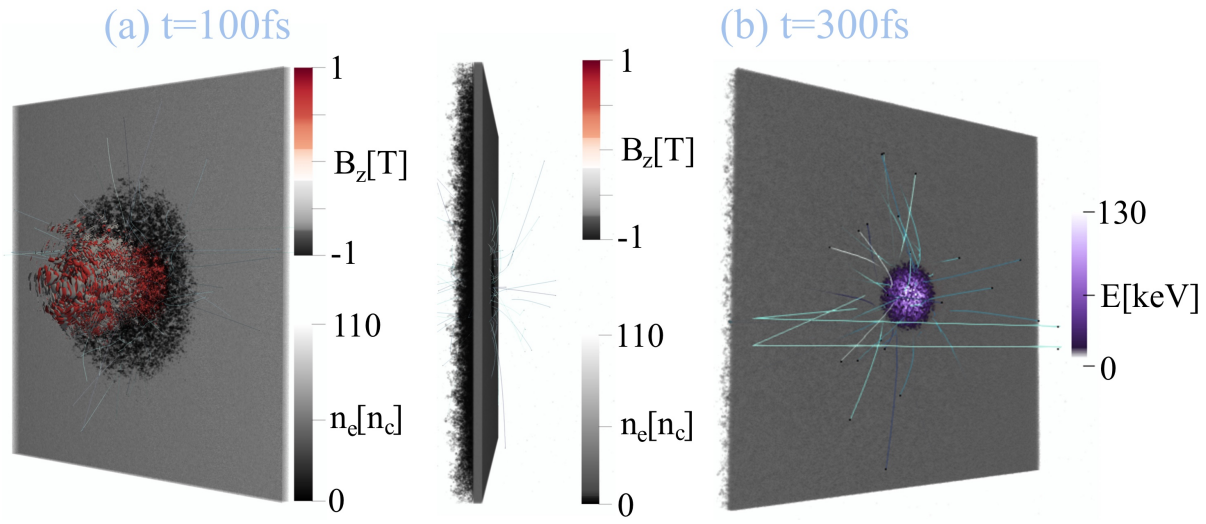

Figure 5.34: Electron density n_e in units of n_c at two different time-steps. In (a) the moment of interaction between the laser (B_z field contour) and the plasma is shown. In (b) the electron density at the final time-step of the simulation is shown in cross-section and together with the positions of some sampled protons at the end of the simulation coloured according to their energy E. In all the shots some electron trajectories are plotted in light-blue.

6 | Discussion on the results

This last chapter is devoted to the discussion of the results presented in the previous chapter. Firstly, the discussion on the reliability of two-dimensional simulations for extracting quantitative data is presented. A discussion on the optimal simulation configuration to describe the interaction of a 20TW laser with a target follows together with the discussion on the results of the simulations. After that, the same kind of discussion will be proposed for a sub-TW laser. The last part of the chapter will be dedicated, instead, to the comparison between the 20 TW and sub-TW different regimes of the interaction between lasers and solid targets.

6.1. General discussion on 2D simulation reliability

The reliability of the results of the two-dimensional simulations has been studied during this thesis work, particularly in the case of the 20 TW laser. By comparing the results presented in section (5.3.1) and (5.4.1), one can observe great differences both in the efficiency of the conversion of the laser energy into kinetic energy of the contaminants and in the energy spectrum of the latter. In both cases, the two-dimensional geometry seems beneficial in enhancing the energy conversion due to all the effects which were presented in section (2.2). Thus, the procedure which was applied to retrieve the simulation time at which extracting the spectrum does not seem to compensate for these effects. There can be many possible explanations for explaining why the procedure did not work properly. First of all, the three-dimensional simulation did not reach the saturation in the total energy of the contaminant ions. Then, the spectrum retrieved at the end of the simulation could not be the right one to compare the results, since the energy of the contaminant ions could continue increasing by absorbing energy from the heated electrons. Secondly, the procedure which was used was based on a model created for metallic single-layer target simulations. The physics behind the acceleration of the electrons in the double-layer targets is highly different, as can be seen even by analysing the simple model presented in section (1.3.4). Processes such as direct laser accelerations can, in fact, play an important role in the temporal evolution of the contaminant ion energy. The evolution of the proton

energy in the DLT cases shows, in the early stages of contaminant acceleration, strong deviations from the logarithmic behaviour predicted by formula (2.15) probably due to the enhanced acceleration processes in the presence of foams. A model which accounts for these processes too, could be more appropriate in describing the two-dimensional results and, thus, it could be more precise in predicting the right time to get the contaminant ion spectrum. Taking into account these processes, however, is not as straightforward as the methodology proposed during this thesis work. The decision of investigating a simpler method was made in order to analyse whether there was a simple way to get quantitative data from two-dimensional simulations. Nevertheless, three-dimensional simulations are the only way to show the physical processes which, due to the constraints in particle motion, are lost in two-dimensional ones. Therefore, even if it had been possible to obtain quantitative data from the latter, the use of three-dimensional simulations is essential to study the physics behind the interaction between lasers and solid targets.

6.2. Discussion on simulations for the 20TW laser

The simulations related to the 20TW laser allow us to make many observations on different themes. First of all, by analysing the ionisation in the substrate, it is possible to see that even without considering a possible laser prepulse, the plain substrate ionises several times. Being the electric field developed by the laser intense enough to ionise almost completely the metallic target, it will be surely able to ionise the foam. The ionisation energies related to the carbon ions are in fact lower than the ones related to aluminium ions due to the reduced nucleus positive charge. Thus, it is possible to neglect the process also in DLTs without losing validity in the results of the simulation. However, by the analysis performed in section (5.2.1), modelling in the three different ways the plain substrates, it is possible to observe a reduction in the energy conversion from laser energy into contaminant kinetic energy when the process is not accounted for. This effect can be explained as an effect of a reduced reflection of the laser pulse by the solid target when the ionisation is considered. The less numerous electron population, in fact, allows the laser to penetrate more inside the material, converting a bigger part of its energy into electron kinetic energy. This increased absorption has an important effect on the evolution of the contaminant ion energy and it is confirmed by observing the electric field in the substrate at the moment of the interaction. The more the target is already ionised at the moment of the interaction, the less the evanescent wave penetrates inside the solid. It is possible to see that, at least when considering the single-layer target, this effect is not completely negligible. However, the majority of the electrons which lead to the TNSA process are usually created in the near-critical layer in double-layer targets. This effect is

surely less visible in transparent materials, therefore, neglecting the ionisation process in the other simulations can be justified. Also, a study on the role of the impact ionisation process should be performed concerning the metallic layer. It is possible to see that this process becomes non-negligible only when the target goes beyond hundreds of nanometers of thickness [100], thus the studied case should not be affected by the effects of the latter process.

Secondly, the role of the target configuration in the acceleration of the contaminant ions was studied. By analysing as first variable, the substrate thickness many observations can be done. It has been proved by several experiments and computational studies that substrate thickness plays an important role in enhancing electron recirculation and heating [101]: the lower the thickness of the substrate the higher the conversion into ion kinetic energy. This is true however until the laser prepulse becomes too high, damaging the target structure [39]. Being the prepulse neglected in the simulations, this same effect is observable by comparing the three different substrate cases. The reduction in the substrate thickness results in an increase in both efficiency and maximum energy of the contaminant protons. This effect can be observed also in the presence of a nearcritical layer, even though it gets mitigated by the latter. By observing, however, the total kinetic energy associated with the substrate ions when the substrate thickness is 200nm, a great difference can be seen comparing it to the other cases, particularly when considering the single-layer target case. The kinetic energy gained by the ions in the thinnest case is in fact orders of magnitude higher than in the others: this effect can be explained in terms of the Coulomb explosion of the substrate [102], which takes place in the first instants after the acceleration. This process is effective in increasing ion energy when a target having a dimension lower than the laser wavelength gets depleted of electrons. The created electric field makes the ion expand until 3D effects, taking place in plane geometry, reduce its effects. This hypothesis can be confirmed by the fact that right after the interaction the ion total energy saturates. Analysing the foam effects, instead, one can observe that the prediction of the optimal foam thickness and density made by the model in section (1.3.4) seems to be correct in the case of the 20TW laser, meaning that an optimisation of the target can be performed, in this regime, by using the simple formulae proposed in the model. Also, it is possible to observe that in all cases the foam brought an increased proton energy, enhancing, thus the laser conversion efficiency.

When analysing also the modelling choices for the foam, one can observe a great impact on the result retrieved from simulations, making the inclusion of the nanostructure important. The relatively low intensity of the laser, in fact, does not allow homogenisation of the foam during the prepulse or during the rising part of the pulse and the nanostructure

plays an important role in the interaction of the foam with the laser pulse [57]. The propagation of the pulse, thus, happens differently between the homogeneous case and the nanostructured case. In the homogeneous case, the DLA process plays an important role in electron heating, creating then, a denser surface in the propagation front. In the nanostructured case, the coulomb explosion of the nanoparticles absorbs the laser pulse. The latter, however, continue propagating among the vacuum spaces reaching the substrate. These two different behaviours, on one hand, lead to an increase in the maximum proton energy of the homogeneous case due to resonance effects; on the other hand, the reduction of the pulse reflection, happening in the homogeneous case due to the denser front, leads to the increased laser absorption shown by the nanostructured case.

At last, comparing the results with experimental results in similar conditions of peak intensity and duration of the pulse [103] for the single-layer target (200 nm thick aluminium), it is possible to observe that the results retrieved from the 3D nanostructured simulation seem to be in agreement with what experimentally observed. In the experiments, in fact, a proton maximum energy of $\sim$ 10 MeV was observed. The order of magnitude of this value is the same one retrieved by the simulation ($\sim$ 15 MeV). The higher value observed in the simulation can be connected to the benefits caused by the presence of a nanostructured layer in front of the metal target, confirming the relevance of the nanostructured foams in enhancing the laser coupling with the target.

6.3. Discussion on simulations for the sub-TW laser

The simulations on the sub-TW laser were performed with the scope of investigating a completely different regime in the interaction between lasers and solid targets. This regime shows many complications in the modelling due to the extremely low energy of the laser pulse. Also, the shaping of the pulse can play a fundamental role in enhancing the energy conversion. Reducing the intensity FWMH, in fact, showed a positive influence in the absorption of the electromagnetic energy by the particles. Keeping the output energy constant and at the meantime reducing the pulse duration, in fact, lead to an increase in the intensity of the field onto the target. The normalised vector potential associated to the laser increased from 0.6 to 1.4, i.e. reaching the relativistic limit. The overcoming of the relativistic limit produces several beneficial processes as the self-induced transparency and self-focusing effect which were presented in section (1.2.3), leading to higher absorption of the laser pulse by the particles.

Concerning the ionisation process, it is possible to observe a great influence of the process on the results. In both laser configurations, in fact, the target never ionises completely.

Thus, the neglection of the process can greatly influence the results of the simulations. This can be observed by comparing the results for the two-dimensional nanostructured case simulated in Smilei with and without ionisation: the final distribution of the energy among the particles looks different in the two cases shown in figure (5.28). The ionisation process, in fact, can lead the ions to absorb a higher part of the laser energy: when the laser interacts with the matter, in fact, encounters a lower number of electrons and this can enhance the laser energy absorption by the ion population. Also, one can observe that neither the foam does completely ionise: an analysis of the impact ionisation effect in the process should be then performed. Foam thickness can be on the order of several micrometers, therefore the impact could be not negligible [100]. However, when considering a real nanostructured foam the particles are usually orders of magnitude lower than the micrometric scale. In this context, thus, the impact ionisation effect could however be negligible. Also, peaks in the ionisation level are observed in figure (5.3) in the lower density case when the intensity does not exceed the relativistic limit: this effect can be explained by observing that the distance between two peaks is almost equal to half a wavelength. The laser pulse, thus, is intense enough to ionise completely the foam only when it reaches the maximum of its intensity, which is found exactly every half cycle. Concerning the foam effect, instead, it was possible to observe an enhancement of the proton maximum energy in all the cases in which the foam was subcritical (see figure (5.15) and table (5.4)). When the foam was even slightly overcritical the laser could not propagate through the first layer and was reflected. This effect, which is observed only in the low-intensity laser, is due to the loss of the relativistic self-induced transparency when the electrons do not reach the relativistic regime. It is also possible to observe that in this case the model proposed in section (1.3.4) is not always suggesting the optimal parameters for the optimisation of the target: particularly in the higher intensity pulse one can note a greater decrease of the mean and maximum proton energy when the foam is the one computed as optimal by the model with respect to the minimum experimentally achievable density one (0.95 n_c). One can explain the result considering the fact that the foam does not get completely ionised during the interaction, while the model considers it as if the ionisation process is negligible. Thus, the electron density computed by the model is not the same that really arises during the interaction and a confirmation of this can be seen by observing the mean ionisation level of the foam. The foam is not completely ionised, thus the real electron population is lower than the one considered in the model.

Besides ionisation, also nanostructure presence influences in a significant way the results: first of all, an enhancement of the proton energy is observed in the overdense foam case

with respect to the homogeneous one. This effect is due to the Coulomb explosion of the nanoparticles which absorb energy without blocking the propagation of the pulse by reflection. The nearcritical case (0.95 n_c) results, instead, in a lower maximum energy with respect to the homogeneous one, as it happened for the 20TW case. This effect can be explained as before as the reduction of the DLA on the electrons of the foam due to the inhomogeneities. Moreover, the nanostructure influences even other aspects: first of all a great increase in the foam ion energy is retrieved when the nanostructure is present (5.26). This effect can again be explained in terms of the Coulomb explosion of the nanoparticles. This process is probably the cause of the greater energy conversion into foam ion kinetic energy than into the contaminant layer ion one: the field accelerating the contaminant layer seems to be, in fact, lower than the one present in the nanostructure. Also, the ionisation process is influenced by the nanostructure: when the nanostructure is present, a few aluminium ions on the front surface are completely ionised.

Lastly, by comparing the results retrieved from the 3D nanostructured simulation with Smilei, it is possible to observe confirmation of the order of magnitude of the proton energy ($\sim$ 100 keV) with respect to known experimental work. Indeed, there are currently only a few experimental works performed with sub-TW class lasers and more experiments would be needed to assess the data from such a regime.

6.4. Analysis and comparison of the two different regimes

As it is possible to observe by the results presented in the previous sections, the two lasers show two very different regimes of the interaction between lasers and solid targets. The regime obtained by the 20TW laser, in fact, brings electrons to ultrarelativistic energies and the field intensity is able to ionise almost completely the target even in the rising part of the pulse. The interaction of the laser pulse happens already with a highly ionised target, allowing the neglection of the process in the numerical description. The sub-TW laser, in both configurations, is not able to ionise completely the target, thus the ionisation process becomes fundamental in describing the interaction. Also, the energy of the obtained protons shows a great decrease when the laser is the less energetic one: a reduction of two orders of magnitude is shown, which is coherent with the reduction in intensity. However, it is possible to observe that for lower-intensity lasers, the TNSA process involving protons becomes less efficient than other ion acceleration processes. The Coulomb explosion of the foam nanoparticles, for example, always results to be very efficient in compact lasers (see figure (5.26)). This reduction in the efficiency of the

TNSA process is associated also with the possibility to perform non-destructive material analysis using the proposed configurations. The high efficiency in converting laser energy into proton kinetic energy (4.58%) and relatively high maximum energy of the protons (15 MeV) retrieved from the most realistic 3D nanostructured simulation for the 20 TW case have proven such a configuration able to perform analyses using, for example, the laser-driven PIXE process [86]. In particular, PIXE requires protons with average energy $\simeq$1 MeV which are easily provided by the studied setup with a 20TW laser and an optimized DLT target. On the contrary, the relatively low efficiency (0.62%) and proton maximum energy (135.14 keV) obtained in the most realistic 3D nanostructured simulation for the sub-TW case make impossible the use of such a laser in the proposed configuration for this scope. The mean energy is, in fact, way under the $\simeq$1 MeV energy required for PIXE analysis. Nevertheless, the efficiency of the Coulomb explosion could be crucial in allowing the use of the sub-TW laser for material analysis. The two different regimes show even differences in the interaction with slightly overdense homogeneous foams: the sub-TW laser, in fact, having an intensity such as the relativistic self-induced transparency has no such influence on the laser propagation, does not show the propagation of the pulse in the denser foam, drawing benefit from the nanostructure presence, which mitigates the reflection of the pulse; the 20TW laser, instead, always shows a deterioration of the maximum proton energy when the foam is nanostructured. However, the increase in the conversion efficiency due to the nanostructure in the 20TW case was not always seen in the sub-TW case. This effect should be investigated more since the comparison between the nanostructured case and the homogeneous case was only performed in two-dimensional simulations, in which the shape of the foam particles is seen as an infinite cylinder.

Conclusions and Future Developments

The interaction of low-power high-intensity lasers with solid targets can be used to produce compact radiation sources which can be employed in various contexts. They can overcome some of the space and investment drawbacks of conventional radiation sources. Moreover, laser-driven sources are more flexible. The same device can potentially be used to produce different radiations only by small changes in the configuration. Ion acceleration is one of the most studied laser-driven radiation sources. The most prominent mechanism to accelerate ions is surely the Target Normal Sheath Acceleration (TNSA) mechanism, which is effective in accelerating the hydro-contaminants naturally present on the surfaces of solid targets. Many strategies have been developed over the years to increase the efficiency of this process. Among the others, the use of non-conventional solid targets is surely one of the most promising. At Nanolab laboratories (Politecnico di Milano), the production of such targets has focused on two main strategies: firstly, the production of ultra-thin metallic films (e.g. using HiPIMS); secondly, the growth of low-density nanostructured layers on the front surface of metallic films with advanced techniques such as Pulsed Laser Deposition (PLD). This latter configuration is referred to as double-layer target. In this thesis work, a numerical investigation of the use of double-layer targets with carbon foams to realise compact sources was performed.

The results of the first part of the thesis work brought to the estimation of two coefficients k, coming from equation (1.39), which characterise the numerical foams grown with different deposition methods using a proprietary code. Such characterisation provides a simple way to set the simulation parameters in order to construct a numerical foam with the desired characteristics, at least up to a certain density range. For high-density foams, the estimation of the mean gyration radius, i.e. the characteristic distance from the centre of the clusters in the foam at which their mass can be concentrated keeping constant the moment of inertia, was not straightforward and further investigation is needed. The two k resulting from the analysis of the numerical foams (0.611 for the ballistic deposition and 0.495 for the diffusive deposition) and the experimental data are in good agreement.

The code seems to reproduce accurately the realistic foams.

The vast numerical campaign focused on analysing the TNSA process in tens of TW and sub-TW lasers brought, instead, to many conclusions. The use of known analytical models to account for the reduced-dimensionality effects is not applicable in the presence of the nearcritical layer typical of the DLTs. Great importance of the ionisation process is observed when the energy of the laser pulse is relatively low. The process is negligible in other cases. It was also shown that when the laser peak power is in the order of tens of TW, the relations proposed by simple models for the interaction between the laser and a DLT are able to predict the optimal condition in enhancing the TNSA process. For sub-TW lasers, instead, the neglection of the ionisation process in the model probably causes the failure of these simple modelisations. The influence of the metal substrate thickness was also shown confirming that a decrease in the substrate thickness always brings to a higher energy conversion. This effect is even more evident in the single-layer target case. Indeed, the foam presence mitigates the differences. It was also shown that when considering tens of TW and sub-TW lasers, the results varied in a non-negligible way when the nanostructure presence was accounted for. The nanostructure, in fact, does not homogenise during the rise of the laser pulse. In particular, in many situations, the nanostructure was shown to be beneficial in increasing the efficiency in converting the laser energy into kinetic energy of the contaminant ions. However, it also causes the suppression of resonance processes, such as Direct Laser Acceleration (DLA), happening in homogeneous nearcritical layers. Therefore, the maximum proton energy is reduced. When the laser cannot propagate inside the nearcritical layer, however, the nanostructure is always beneficial. It was also shown that in all cases considering the nanostructure, the kinetic energy acquired by foam ions shows an important increase which can be explained in terms of the Coulomb explosion of the particles. The results have shown that the 20 TW laser, having a maximum proton energy of around 15 MeV and a mean energy of around 2 MeV, is suitable for applications in material analysis such as PIXE. On the contrary, the sub-TW laser, having maximum proton energy in the order of some hundreds of keV, is not suitable for such applications using the proposed configuration.

In conclusion during the thesis work a clarification of the most appropriate modelling strategies for the interaction between tens of TW and sub-TW lasers and solid targets was obtained. The characterisation of the numerical foams retrieved from the proprietary Diffusion-Limited Cluster-Cluster Aggregation (DLCCA) code allowed the production of the numerical foams necessary to include the right nanostructure in PIC simulations. Lastly, a qualitative analysis of the possible applications of the proposed configurations was performed. Many possible future perspectives have opened in light of the result of

this thesis work and they are listed hereinafter.

- Concerning the numerical foams, a continuation of the analysis of the foams generated by the proprietary DLCCA code. The characterisation of the high-density foams produced by using a few particles per cluster should be performed. Also, enabling the extraction of the number of particles per cluster from a general distribution could allow more realistic modelling of foams. At last, also an optimisation of the use of numerical resources by the code, such as RAM, should be performed.
- Concerning the simple analytical modelling, firstly a model taking into account the foam effects in the acceleration could be proposed in order to estimate the maximum energy of the protons from two-dimensional simulations. Secondly, a way to introduce the effects of the ionisation process in the model of the propagation of the laser pulse in the foam could be investigated. This could be useful to extend the model to the interaction of lower-energy lasers with DLTs.
- Concerning the numerical modelling, firstly the effects of the substrate thickness in ionisation should be investigated by performing two-dimensional simulations, also in the 20 TW case. An investigation of the substrate thickness effect both in ionisation and in proton energy should be performed also for the sub-TW case. In general, a deeper analysis of the effects and the evolution of the field ionisation process should be performed. Also, the possible effects of Coulomb collisions and impact ionisation should be investigated, with a particular emphasis on the sub-TW case. Also, the effects of the prepulse on single-layer targets with ultrathin substrates should be investigated via hydrodynamical simulations. This would be useful to understand when the prepulse causes an expansion of the target which decreases the benefits of the thin substrate.
- Concerning the optimisation of the proton acceleration, an investigation of the use of nanostructured plastic foams as nearcritical layers could be performed. The high conversion efficiency of the laser energy into the kinetic energy of the foam ions in nanostructured foams could be beneficial in enhancing the proton acceleration process both in tens of TW and sub-TW lasers, possibly allowing the acceleration of protons up to MeV order of magnitude also in the sub-TW case. Particular focus, in this case, should be directed, also, to the analysis of the proton emission angular distribution.
- Lastly, experimental campaigns could be useful to both confirm the results obtained from the performed simulations and to demonstrate the feasibility of compact laser-driven sources using class-TW lasers. The numerical simulations could also be useful

in understanding some physical processes behind the performed experiments.

All the proposed future perspectives regarding both numerical and experimental investigations have the scope to design compact radiation sources by means of TW-class laser facilities. These radiation sources could be used in contexts in which the use of conventional sources is prohibitive.

Bibliography

[1] O. Svelto. *Principles of Lasers*. Springer, New York, fifth edition, 2010.

[2] A. L. Schawlow and C. H. Townes. Infrared and optical masers. *Physical Review*, 112:1940–1949, 1958.

[3] F. J. McClung and R. W. Hellwarth. Giant Optical Pulsations from Ruby. *Journal of Applied Physics*, 33(3):828–829, 2004.

[4] H. W. Mocker and R. J. Collins. Mode competition and self-locking effects in a Q-switched ruby laser. *Applied Physics Letters*, 7(10):270–273, 2004.

[5] R. Baumgartner and R. Byer. Optical parametric amplification. *IEEE Journal of Quantum Electronics*, 15(6):432–444, 1979.

[6] G. Strickland, S.and Mourou. Compression of amplified chirped optical pulses. *Optics Communications*, 56(3):219–221, 1985.

[7] G. A. Mourou, N. J. Fisch, V. M. Malkin, Z. Toroker, E. A. Khazanov, A. M. Sergeev, T. Tajima, and B. Le Garrec. Exawatt-zettawatt pulse generation and applications. *Optics Communications*, 285(5):720–724, 2012.

[8] T. J. M. Boyd and J. J. Sanderson. *The Physics of Plasmas*. Cambridge University Press, 2003.

[9] V. E. Golant, A. P. Zhilinskiĭ, and I. E. Sakharov. *Fundamentals of Plasma Physics*. Plasma Physics Series. J. Wiley, 1980.

[10] G. Purcella and S.E. Segre. *Fisica dei plasmi*. Zanichelli, 2009.

[11] Plasma 21 Committee, Plasma Science Committee, and National Research Council, editors. *Plasma Science: Advancing Knowledge in the National Interest*. National Academy of Sciences, 2013.

[12] L. Gallmann, I. Jordan, H. J. Wörner, L. Castiglioni, M. Hengsberger, J. Osterwalder, C. A. Arrell, M. Chergui, E. Liberatore, U. Rothlisberger, and U. Keller.

Photoemission and photoionization time delays and rates. *Structural Dynamics*, 4(6):061502, 2017.

[13] A. Macchi. *A Superintense Laser-Plasma Interaction Primer*. Springer Dordrecht, 2013.

[14] A. I. Akhiezer and R. V. Polovin. Theory of wave motion of an electron plasma. *Soviet Physics JETP*, Vol 3, 1956.

[15] T. Tajima and J. M. Dawson. Laser electron accelerator. *Physical Review Letter*, 43:267–270, 1979.

[16] A. Pukhov, Z.-M. Sheng, and J. Meyer-ter Vehn. Particle acceleration in relativistic laser channels. *Physics of Plasmas*, 6(7):2847–2854, 1999.

[17] P. Mulser and D. Bauer. *High Power Laser-Matter Interaction*. Springer Tracts in Modern Physics. Springer Berlin Heidelberg, 2011.

[18] E. S. Weibel. Anomalous skin effect in a plasma. *Physics of Fluids*, 10(4):741–748, 1967.

[19] P. J. Catto and R. M. More. Sheath inverse bremsstrahlung in laser produced plasmas. *Physics of Fluids*, 20(4):704–705, 1977.

[20] J. Albritton and P. Koch. Cold plasma wavebreaking: Production of energetic electrons. *Physics of Fluids*, 18(9):1136–1139, 1975.

[21] F. Brunel. Not-so-resonant, resonant absorption. *Physical Review Letter*, 59:52–55, 1987.

[22] P. Mulser, H. Ruhl, and J. Steinmetz. Routes to irreversibility in collective laser–matter interaction. *Laser and Particle Beams*, 19(1):23–28, 2001.

[23] W. L. Kruer and K. Estabrook. J $\times$ B heating by very intense laser light. *Physics of Fluids*, 28(1):430–432, 1985.

[24] A. Macchi, M. Borghesi, and M. Passoni. Ion acceleration by superintense laser-plasma interaction. *Reviews of Modern Physics*, 85:751–793, 2013.

[25] T. Schlegel, N. Naumova, V. T. Tikhonchuk, C. Labaune, I. V. Sokolov, and G. Mourou. Relativistic laser piston model: Ponderomotive ion acceleration in dense plasmas using ultraintense laser pulses. *Physics of Plasmas*, 16:083103, 2009.

[26] J. F. L. Simmons and C. R. McInnes. Was marx right? or how efficient are laser driven interstellar spacecraft? *American Journal of Physics*, 61:205–207, 1993.

[27] T. Esirkepov, M. Borghesi, S. V. Bulanov, G. Mourou, and T. Tajima. Highly efficient relativistic-ion generation in the laser-piston regime. *Physical Review Letter*, 92:175003, 2004.

[28] L. O. Silva, M. Marti, J. R. Davies, R. A. Fonseca, C. Ren, F. S. Tsung, and W. B. Mori. Proton shock acceleration in laser-plasma interactions. *Physical Review Letter*, 92:015002, 2004.

[29] K. Nishihara, H. Amitani, M. Murakami, S. V. Bulanov, and T. Z. Esirkepov. High energy ions generated by laser driven coulomb explosion of cluster. *Nuclear Instruments and Methods in Physics Research Section A: Accelerators, Spectrometers, Detectors and Associated Equipment*, 464(1):98–102, 2001.

[30] Y. Sentoku, T. V. Liseikina, T. Zh. Esirkepov, F. Califano, N. M. Naumova, Y. Ueshima, V. A. Vshivkov, Y. Kato, K. Mima, K. Nishihara, F. Pegoraro, and S. V. Bulanov. High density collimated beams of relativistic ions produced by petawatt laser pulses in plasmas. *Physical Review E*, 62(5):6983, 2000.

[31] S. C. Wilks, A. B. Langdon, T. E. Cowan, M. Roth, M. Singh, S. Hatchett, M. H. Key, D. Pennington, A. MacKinnon, and R. A. Snavely. Energetic proton generation in ultra-intense laser–solid interactions. *Physics of Plasmas*, 8:542–549, 2001.

[32] M. Passoni, V. T. Tikhonchuk, M. Lontano, and V. Yu. Bychenkov. Charge separation effects in solid targets and ion acceleration with a two-temperature electron distribution. *Physical Review E*, 69:026411, 2004.

[33] P. Mora. Plasma expansion into a vacuum. *Physical Review Letter*, 90:185002, 2003.

[34] M. Passoni and M. Lontano. Theory of light-ion acceleration driven by a strong charge separation. *Physical Review Letter*, 101:115001, 2008.

[35] M. Passoni, L. Bertagna, and A. Zani. Target normal sheath acceleration: theory, comparison with experiments and future perspectives. *New Journal of Physics*, 12:045012, 2010.

[36] M. Passoni, C. Perego, A. Sgattoni, and D. Batani. Advances in target normal sheath acceleration theory. *Physics of Plasmas*, 20:060701, 2013.

[37] A. Formenti, A. Maffini, and M. Passoni. Non-equilibrium effects in a relativistic plasma sheath model. *New Journal of Physics*, 22:053020, 2020.

[38] V. T. Tikhonchuk, A. A. Andreev, S. G. Bochkarev, and V. Yu Bychenkov. Ion

acceleration in short-laser-pulse interaction with solid foils. *Plasma Physics and Controlled Fusion*, 47(12B):B869, 2005.

[39] D. Neely, P. Foster, A. Robinson, F. Lindau, O. Lundh, A. Persson, C.-G. Wahlström, and P. McKenna. Enhanced proton beams from ultrathin targets driven by high contrast laser pulses. *Applied Physics Letters*, 89(2):021502, 2006.

[40] M. Passoni, F. M. Arioli, L. Cialfi, D. Dellasega, L. Fedeli, A. Formenti, M. C. Giovannelli, A. Maffini, F. Mirani, and A. Pazzaglia. Advanced laser-driven ion sources and their applications in materials and nuclear science. *Plasma Physics and Controlled Fusion*, 62(1):014022, 2020.

[41] V. Horný, S. N. Chen, X. Davoine, V. Lelasseux, L. Gremillet, and J. Fuchs. High-flux neutron generation by laser-accelerated ions from single- and double-layer targets. *Scientific Reports*, 12:19767, 2022.

[42] I. Prencipe, A. Sgattoni, D. Dellasega, L. Fedeli, L. Cialfi, Il Woo Choi, I. Jong Kim, K. A. Janulewicz, K. F. Kakolee, and Hwang Woon Lee. Development of foam-based layered targets for laser-driven ion beam production. *Plasma Physics and Controlled Fusion*, 58(3):034019, 2016.

[43] E. Esarey, P. Sprangle, J. Krall, and A. Ting. Self-focusing and guiding of short laser pulses in ionizing gases and plasmas. *IEEE Journal of Quantum Electronics*, 33(11):1879–1914, 1997.

[44] H. Y. Wang, C. Lin, Z. M. Sheng, B. Liu, S. Zhao, Z. Y. Guo, Y. R. Lu, X. T. He, J. E. Chen, and X. Q. Yan. Laser shaping of a relativistic intense, short gaussian pulse by a plasma lens. *Physical Review Letter*, 107:265002, 2011.

[45] D. B. Zou, H. B. Zhuo, X. H. Yang, F. Q. Shao, Y. Y. Ma, T. P. Yu, H. C. Wu, Y. Yin, Z. Y. Ge, and X. H. Li. Enhanced target normal sheath acceleration based on the laser relativistic self-focusing. *Physics of Plasmas*, 21:063103, 2014.

[46] A. Sgattoni, P. Londrillo, A. Macchi, and M. Passoni. Laser ion acceleration using a solid target coupled with a low-density layer. *Physical Review E*, 85:036405, 2012.

[47] Y. J. Gu, Q. Kong, S. Kawata, T. Izumiyama, X. F. Li, Q. Yu, P. X. Wang, and Y. Y. Ma. Enhancement of proton acceleration field in laser double-layer target interaction. *Physics of Plasmas*, 20:070703, 2013.

[48] W. J. Ma, I Jong Kim, J. Q. Yu, Il Woo Choi, P. K. Singh, Hwang Woon Lee, Jae Hee Sung, Seong Ku Lee, C. Lin, Q. Liao, J. G. Zhu, H. Y. Lu, B. Liu, H. Y. Wang, R. F. Xu, X. T. He, J. E. Chen, M. Zepf, J. Schreiber, X. Q. Yan, and

Chang Hee Nam. Laser acceleration of highly energetic carbon ions using a double-layer target composed of slightly underdense plasma and ultrathin foil. *Physical Review Letter*, 122:014803, 2019.

[49] M. Passoni, A. Sgattoni, I. Prencipe, L. Fedeli, D. Dellasega, L. Cialfi, Il Woo Choi, I Jong Kim, K. A. Janulewicz, Hwang Woon Lee, Jae Hee Sung, Seong Ku Lee, and Chang Hee Nam. Toward high-energy laser-driven ion beams: Nanostructured double-layer targets. *Physical Review Accel. Beams*, 19:061301, 2016.

[50] Z. Mei, Z. Pan, Z. Liu, S. Xu, Y. Shou, P. Wang, Z. Cao, D. Kong, Y. Liang, Z. Peng, T. Song, X. Chen, T. Xu, Y. Gao, S. Chen, J. Zhao, Y. Zhao, X. Yan, and W. Ma. Energetic laser-driven proton beams from near-critical-density double-layer targets under moderate relativistic intensities. *Physics of Plasmas*, 30:033107, 2023.

[51] A. Pazzaglia, L. Fedeli, A. Formenti, A. Maffini, and M. Passoni. A theoretical model of laser-driven ion acceleration from near-critical double-layer targets. *Communications Physics*, 3:133, 2020.

[52] R. De Luca, F. Maviglia, G. Federici, G. Calabró, P. Fanelli, and F. Vivio. Preliminary investigation on w foams as protection strategy for advanced fw pfcs. *Fusion Engineering and Design*, 146:1690–1693, 2019.

[53] P. Meakin. *Fractals, Scaling and Growth Far from Equilibrium*. Cambridge University Press, USA, 2011.

[54] A. Maffini, D. Orecchia, A. Pazzaglia, M. Zavelani-Rossi, and M. Passoni. Pulsed laser deposition of carbon nanofoam. *Applied Surface Science*, 599:153859, 2022.

[55] D. A. Weitz, J. S. Huang, M. Y. Lin, and J. Sung. Limits of the fractal dimension for irreversible kinetic aggregation of gold colloids. *Physical Review Letter*, 54:1416–1419, 1985.

[56] T. A. Witten and L. M. Sander. Diffusion-limited aggregation, a kinetic critical phenomenon. *Physical Review Letter*, 47:1400–1403, 1981.

[57] L. Fedeli, A. Formenti, C. E. Bottani, and M. Passoni. Parametric investigation of laser interaction with uniform and nanostructured near-critical plasmas. *The European Physical Journal D*, 71(8):202, 2017.

[58] L. Fedeli, A. Formenti, L. Cialfi, A. Pazzaglia, and M. Passoni. Ultra-intense laser interaction with nanostructured near-critical plasmas. *Scientific Reports*, 8(1):3834, 2018.

[59] Y. L. Klimontovich. Introduction to kinetic theory of nonideal fully ionized plasmas. In Y. L. Klimontovich, editor, *Kinetic Theory of Nonideal Gases and Nonideal Plasmas*, volume 105 of *International Series in Natural Philosophy*, pages 107–110. Pergamon, 1982.

[60] Y. L. Klimontovich. Chapter 3 - equations with a self-consistent field — vlasov equations. In D. Ter Haar and Y.L. Klimontovich, editors, *The Statistical Theory of Non-Equilibrium Processes in a Plasma*, volume 9 of *International Series in Natural Philosophy*, pages 68–116. Pergamon, 1967.

[61] Y. L. Klimontovich. Chapter 7 - kinetic equations for the ideal fully ionized plasma. In Y. L. Klimontovich, editor, *Kinetic Theory of Nonideal Gases and Nonideal Plasmas*, volume 105 of *International Series in Natural Philosophy*, pages 139–167. Pergamon, 1982.

[62] H. H. Francis. Fluid dynamics in group t-3 los alamos national laboratory: (la-ur-03-3852). *Journal of Computational Physics*, 195(2):414–433, 2004.

[63] J. Dawson. One-Dimensional Plasma Model. *The Physics of Fluids*, 5(4):445–459, 1962.

[64] A. B. Langdon and C. K. Birdsall. Theory of plasma simulation using finite-size particles. *Physics of Fluids*, 13:2115–2122, 1970.

[65] G. Lapenta. Kinetic plasma simulation: particle in cell method. In *Schriften des Forschungszentrums Jülich Reihe Energie & Umwelt / Energy & Environment*, volume 298, pages 76–85, Jülich, 2015. 12th Carolus Magnus Summer School on Plasma and Fusion Energy Physics, Leuven (Belgium), 24 Aug 2015 - 4 Sep 2015, Forschungszentrum Jülich GmbH Zentralbibliothek, Verlag.

[66] J. M. Dawson. Particle simulation of plasmas. *Reviews of Modern Physics*, 55:403–447, 1983.

[67] J. Liu, M. Chen, J. Zheng, Z. Sheng, and C. Liu. Three dimensional effects on proton acceleration by intense laser solid target interaction. *Physics of Plasmas*, 20(6):063107, 2013.

[68] J. Schreiber, F. Bell, F. Grüner, U. Schramm, M. Geissler, M. Schnürer, S. Ter-Avetisyan, B. M. Hegelich, J. Cobble, E. Brambrink, J. Fuchs, P. Audebert, and D. Habs. Analytical model for ion acceleration by high-intensity laser pulses. *Physical Review Letter*, 97:045005, 2006.

[69] K. D. Xiao, C. T. Zhou, K. Jiang, Y. C. Yang, R. Li, H. Zhang, B. Qiao, T. W.

Huang, J. M. Cao, T. X. Cai, M. Y. Yu, S. C. Ruan, and X. T. He. Multidimensional effects on proton acceleration using high-power intense laser pulses. *Physics of Plasmas*, 25(2):023103, 2018.

[70] S. Sinigardi, J. Babaei, and G. Turchetti. Tnsa proton maximum energy laws for 2d and 3d pic simulations. *Nuclear Instruments and Methods in Physics Research Section A: Accelerators, Spectrometers, Detectors and Associated Equipment*, 909:438–440, 2018.

[71] J. Babaei, L. A. Gizzi, P. Londrillo, S. Mirzanejad, T. Rovelli, S. Sinigardi, and G. Turchetti. Rise time of proton cut-off energy in 2d and 3d pic simulations. *Physics of Plasmas*, 24(4):043106, 2017.

[72] A. M. Perelomov, V. S. Popov, and M. V. Terent'ev. Ionization of atoms in an alternating electric field. *Soviet Physics JETP*, 23(5):1393–1409, 1966.

[73] M. V. Ammosov, N. B. Delone, and V. P. Krainov. Tunnel ionization of complex atoms and of atomic ions in an alternating electromagnetic field. *Zhurnal Eksperimental'noi i Teoreticheskoi Fiziki*, 91(6):2008–2013, 1986.

[74] L. Fedeli, A. Formenti, L. Cialfi, A. Sgattoni, G. Cantono, and M. Passoni. Structured targets for advanced laser-driven sources. *Plasma Physics and Controlled Fusion*, 60(1):014013, 2018.

[75] L. M. Sander. Fractal growth processes. *Nature*, 322(6082):789–793, 1986.

[76] P. L. Leath. Cluster size and boundary distribution near percolation threshold. *Physical Review B*, 14:5046–5055, 1976.

[77] B. D. Hughes, E. W. Montroll, and M. F. Shlesinger. Fractal random walks. *Journal of Statistical Physics*, 28(1):111–126, 1982.

[78] E. Murray. A two-dimensional growth process. In *Fourth Berkeley symposium on mathematical statistics and probability*, pages 223–239, 1961.

[79] P. Meakin and F. Family. Structure and kinetics of reaction-limited aggregation. *Physical Review A*, 38(4):2110 – 2123, 1988.

[80] J. V. Marjorie. Computer simulation of floc formation in a colloidal suspension. *Journal of Colloid Science*, 18(7):684–695, 1963.

[81] P. Meakin. Formation of fractal clusters and networks by irreversible diffusion-limited aggregation. *Physical Review Letters*, 51(13):1119 – 1122, 1983.

[82] T.A. Witten and L.M. Sander. Diffusion-limited aggregation. *Physical Review B*, 27(9):5686 – 5697, 1983.

[83] P. Meakin. A historical introduction to computer models for fractal aggregates. *Journal of Sol-Gel Science and Technology*, 15(2):97–117, 1999.

[84] M. Galbiati, A. Formenti, M. Grech, and M. Passoni. Numerical investigation of non-linear inverse compton scattering in double-layer targets. *Frontiers in Physics*, 11, 2023.

[85] D. Margarone, I. J. Kim, J. Psikal, J. Kaufman, T. Mocek, I. W. Choi, L. Stolcova, J. Proska, A. Choukourov, I. Melnichuk, O. Klimo, J. Limpouch, J. H. Sung, S. K. Lee, G. Korn, and T. M. Jeong. Laser-driven high-energy proton beam with homogeneous spatial profile from a nanosphere target. *Physical Review Special Topics - Accelerators and Beams*, 18:071304, 2015.

[86] A. Maffini, F. Mirani, M. Galbiati, K. Ambrogioni, F. Gatti, M. S. Galli De Magistris, D. Vavassori, D. Orecchia, D. Dellasega, V. Russo, M. Zavelani-Rossi, and M. Passoni. Towards compact laser-driven accelerators: exploring the potential of advanced double-layer targets. *EPJ Techniques and Instrumentation*, 10(1):15, 2023.

[87] F. Mirani, A. Maffini, F. Casamichiela, A. Pazzaglia, A. Formenti, D. Dellasega, V. Russo, D. Vavassori, D. Bortot, M. Huault, G. Zeraouli, V. Ospina, S. Malko, J. I. Apiñaniz, J. A. Pérez-Hernández, D. De Luis, G. Gatti, L. Volpe, A. Pola, and M. Passoni. Integrated quantitative pixe analysis and edx spectroscopy using a laser-driven particle source. *Science Advances*, 7(3):eabc8660, 2021.

[88] J. Derouillat, A. Beck, F. Pérez, T. Vinci, M. Chiaramello, A. Grassi, M. Flé, G. Bouchard, I. Plotnikov, N. Aunai, J. Dargent, C. Riconda, and M. Grech. Smilei : A collaborative, open-source, multi-purpose particle-in-cell code for plasma simulation. *Computer Physics Communications*, 222:351–373, 2018.

[89] L. Fedeli, A. Huebl, F. Boillod-Cerneux, T. Clark, K. Gott, C. Hillairet, S. Jaure, A. Leblanc, R. Lehe, A. Myers, C. Piechurski, M. Sato, N. Zaim, W. Zhang, J. L. Vay, and H. Vincenti. Pushing the frontier in the design of laser-based electron accelerators with groundbreaking mesh-refined particle-in-cell simulations on exascale-class supercomputers. In *SC22: International Conference for High Performance Computing, Networking, Storage and Analysis*, pages 1–12, 2022.

[90] A. Stukowski. Visualization and analysis of atomistic simulation data with ovito–

the open visualization tool. *Modelling and Simulation in Materials Science and Engineering*, 18(1):015012, 2010.

[91] T. Z. Esirkepov. Exact charge conservation scheme for particle-in-cell simulation with an arbitrary form-factor. *Computer Physics Communications*, 135(2):144–153, 2001.

[92] A. Taflove, S. C. Hagness, and M. Piket-May. Chapter 9 - computational electromagnetics: The finite-difference time-domain method. In WAI-KAI CHEN, editor, *The Electrical Engineering Handbook*, pages 629–670. Academic Press, Burlington, 2005.

[93] Y. Kane. Numerical solution of initial boundary value problems involving maxwell's equations in isotropic media. *IEEE Transactions on Antennas and Propagation*, 14(3):302–307, 1966.

[94] A. Iserles. Generalized Leapfrog Methods. *IMA Journal of Numerical Analysis*, 6(4):381–392, 1986.

[95] R. Courant, K. Friedrichs, and H. Lewy. On the partial difference equations of mathematical physics. *IBM Journal of Research and Development*, 11(2):215–234, 1967.

[96] J. P. Boris. Cylrad particle pusher. In *Proc. Fourth Conference on Numerical Simulation of Plasmas*, 1970.

[97] R. Nuter, L. Gremillet, E. Lefebvre, A. Lévy, T. Ceccotti, and P. Martin. Field ionization model implemented in Particle In Cell code and applied to laser-accelerated carbon ions. *Physics of Plasmas*, 18(3):033107, 2011.

[98] I. Prencipe, D. Dellasega, A. Zani, D Rizzo, and M Passoni. Energy dispersive x-ray spectroscopy for nanostructured thin film density evaluation. *Science and Technology of Advanced Materials*, 16(2):025007, 2015.

[99] S. Mondal, M. Shirozhan, N. Ahmed, M. Bocoum, F. Boehle, A. Vernier, S. Haessler, R. Lopez-Martens, F. Sylla, C. Sire, F. Quéré, K. Nelissen, K. Varjú, D. Charalambidis, and S. Kahaly. Surface plasma attosource beamlines at eli-alps. *Journal of the Optical Society of America B: Optical Physics*, 35(5):A93–A102, 2018.

[100] G. M. Petrov, J. Davis, and Tz. Petrova. Ionization dynamics of high-intensity laser–target interactions. *Plasma Physics and Controlled Fusion*, 51(9):095005, 2009.

[101] A. J. Mackinnon, Y. Sentoku, P. K. Patel, D. W. Price, S. Hatchett, M. H. Key, C. Andersen, R. Snavely, and R. R. Freeman. Enhancement of proton acceleration by hot-electron recirculation in thin foils irradiated by ultraintense laser pulses. *Physical Review Letter*, 88:215006, 2002.

[102] S. S. Bulanov, A. Brantov, V. Y. Bychenkov, V. Chvykov, G. Kalinchenko, T. Matsuoka, P. Rousseau, S. Reed, V. Yanovsky, K. Krushelnick, D. W. Litzenberg, and A. Maksimchuk. Accelerating protons to therapeutic energies with ultraintense, ultraclean, and ultrashort laser pulses. *Medical Physics*, 35(5):1770–1776, 2008.

[103] V. Yu. Bychenkov, P. K. Singh, H. Ahmed, K. F. Kakolee, C. Scullion, T. W. Jeong, P. Hadjisolomou, A. Alejo, S. Kar, M. Borghesi, and S. Ter-Avetisyan. Ion acceleration in electrostatic field of charged cavity created by ultra-short laser pulses of 1020–1021 w/cm2. *Physics of Plasmas*, 24(1):010704, 2017.

A | Appendix A

The scope of this appendix is to show some interesting plots and data which can clarify some of the crucial considerations made during the text.

A.1. Useful plots from the 2D scan 20 TW laser simulation

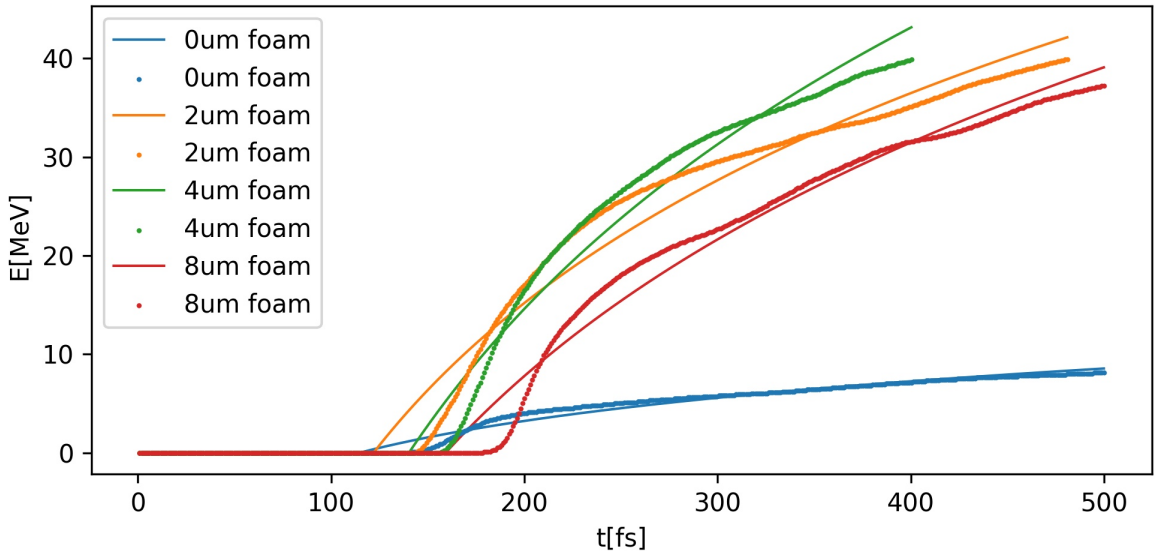

Figure A.1: Time-behaviour of the maximum proton energy in the 2D homogeneous simulations for the 20 TW laser case. The considered substrate is the 600 nm substrate, a similar behaviour is retrieved in the other cases. The plain substrate and different foam thicknesses are shown. The continuous line represents the logarithmic fitting performed using formula (2.15.)

A.2. Useful plots and data from the 2D sub-TW laser WarpX simulations

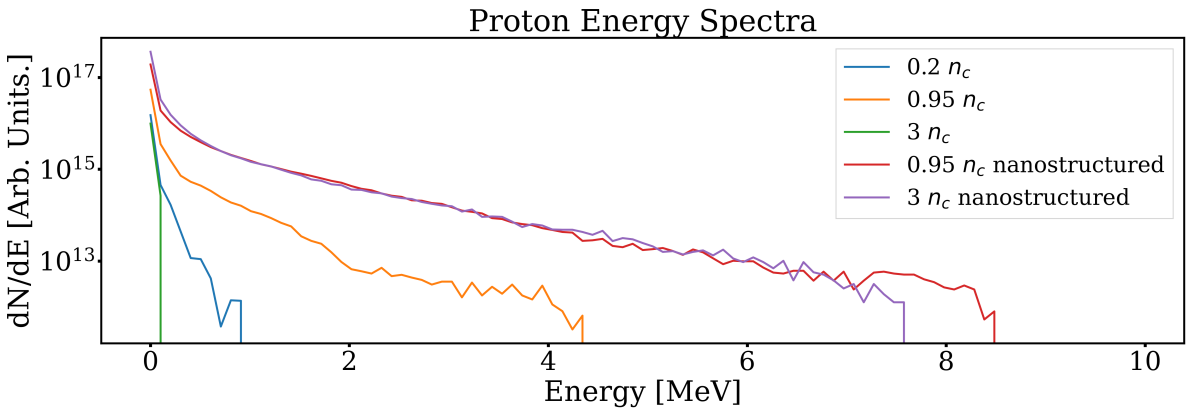

Figure A.2: Plots of the foam ion spectra retrieved 250 fs after the interaction of the laser with the substrate are shown in all cases simulated with 2D WarpX simulations of the 40 fs FWHM laser.

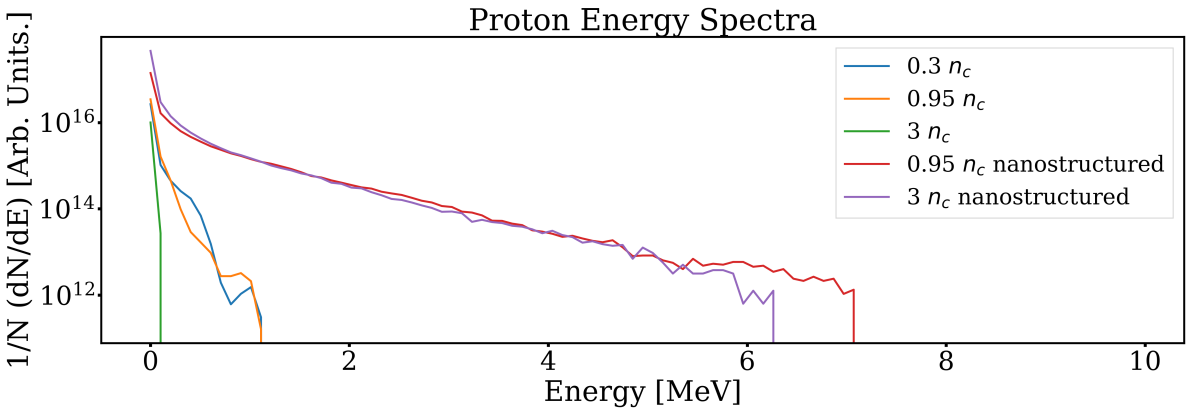

Figure A.3: Plots of the foam ion spectra retrieved 250 fs after the interaction of the laser with the substrate are shown in all cases simulated with 2D WarpX simulations of the 40 fs FWHM laser.

A.3. Useful plots from the 2D nanostructured sub-TW laser Smilei simulation

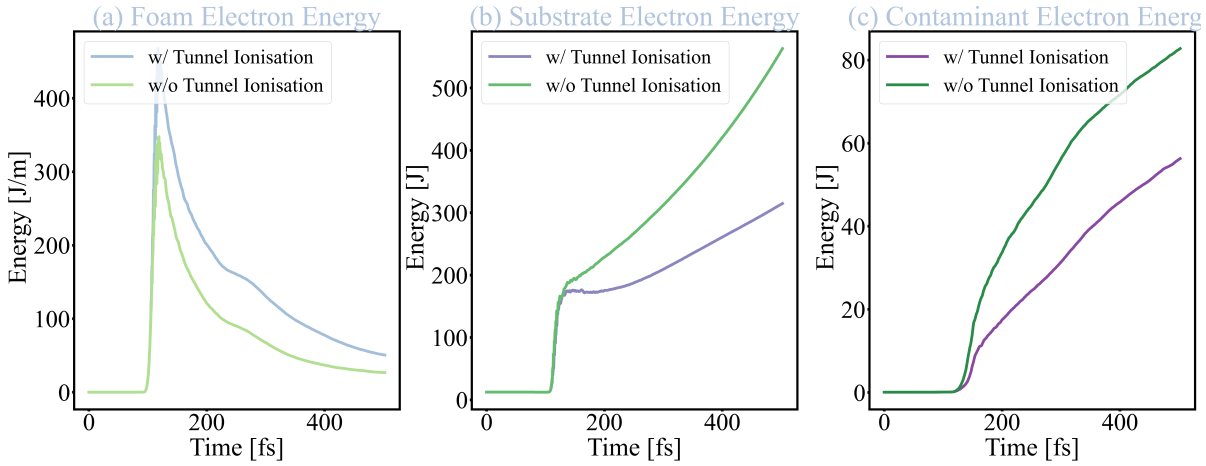

Figure A.4: In (a) the evolution of the foam electron energy in the nanostructured 2D simulations for 0.95 n_c performed in Smilei is shown, in (b) the evolution of the substrate electron energy and in (c) the contaminant electron energy. The plots in green represent the case performed without considering the tunnel ionisation process, the ones in purple represent the case accounting for it.

A.4. Useful plots and data from the 3D sub-TW laser Smilei simulation

Foam thickness	E_f^{max} **[keV]**	$\bar{E}_f$ **[keV]**	T_f **[keV]**	**Efficiency** η_f **[-]**
	FWMH = 40 fs			
0.95 n_c	3685.59	229.12	212.63	23.18%

Table A.1: Summary of the results for foam ion acceleration in the sub-TW laser obtained in the nanostructured 3D simulation for the optimal condition (0.95 n_c 3.0 µm) including tunnel ionisation. The columns show in order the foam ion maximum energy, the mean foam ion energy, the temperature associated with the foam ion spectrum and the laser energy conversion efficiency into kinetic energy of the foam ion.

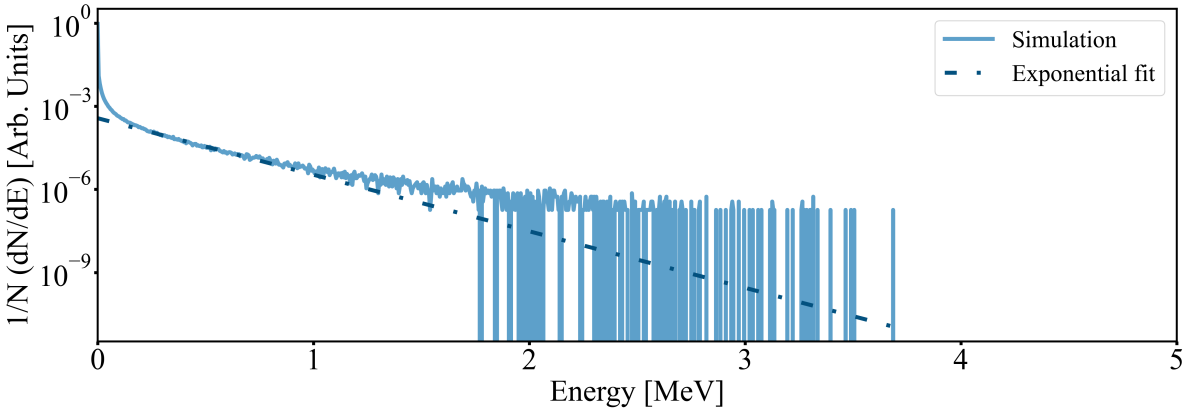

Figure A.5: Plot of the foam ion spectrum retrieved at the end of the 3D nanostructured simulation including tunnel ionisation in the optimal case for sub-TW laser performed with Smilei (0.95 n_c 3.0 µm).

List of Figures

List of Tables

Acknowledgements